Mechanochemical Synthesis of Low F-Doped Aluminium Hydroxide Fluorides

Dissertation

zur Erlangung des akademischen Grades

Doctor rerum naturalium

(Dr. rer. nat.)

im Fach Chemie

eingereicht an der

Mathematisch-Naturwissenschaftichen Fakultät

der Humboldt-Universität zu Berlin

von

M. Sc. Valentina Scalise

Präsidentin der Humboldt-Universität zu Berlin

Prof. Dr.-Ing. Dr. Sabine Kunst

Dekan der Mathematisch-Naturwissenschaftlichen Fakultät

Prof. Dr. Elmar Kulke

Gutachter/innen:

1. Prof. Dr. Erhard Kemnitz
2. PD Dr. Gudrun Scholz
3. Prof. Dr. Mamoru Senna

Tag der mündlichen Prüfung: 22.06.2018

Abstract

The mechanochemical approach opens a reliable and effective strategy for the formation of aluminium hydroxide fluorides with a very low F-content. Milling has the effect of introducing structural defects, causing amorphisation. The fluorination by milling creates a further and drastic increase of this degree of amorphisation.

Synthesis conditions (milling time, fluorination degree, water content) play a crucial role in the product composition.

Firstly, the significant role played by water in the mechanochemical synthesis of highly distorted aluminium hydroxide fluorides was evaluated. The importance of water in the synthesis was considered by a separated combination of O/OH sources ($Al(OH)_3$, Al_2O_3) and fluorine sources with or without structural water (β-$AlF_3 \cdot 3H_2O$, α-AlF_3).

Concerning the degree of fluorination, different aluminium hydroxide fluorides with varying Al/F molar ratios from 1:1.5 up to 1:0.05 were successfully synthesized by mechanochemical reactions. The characterization of the products by XRD, ^{27}Al and ^{19}F MAS NMR, thermal analysis, nitrogen adsorption and zeta potential techniques allows a detailed understanding of the structure and surface properties of the products. Using γ-$Al(OH)_3$ and β-$AlF_3 \cdot 3H_2O$ as OH- and F-sources, respectively, strongly disordered products were obtained with an Al: F molar ratio higher than 1:0.25. The degree of fluorination affects the amount of 4- and 5-fold coordinated Al sites, not present in the reactants. Obviously, these species affect the phase transition to alumina, by decreasing the transition temperature of the formation of α-Al_2O_3.

The influence of the milling time was considered by studying the power of a high energy ball milling process on the structure and at the surface of γ-Al_2O_3. The mechanochemical treatment strongly influences the adsorption of fluorine at the γ-Al_2O_3/ water interface. The time of the treatment has relevant importance on these processes. Since fluorine is not originally present in the bulk of γ-Al_2O_3, ^{19}F MAS NMR studies allow the discrimination of different F-species adsorbed at the surface or present as metal fluoride particles in γ-Al_2O_3 powders after adsorption experiments.

Keywords: mechanochemistry, fluorine, solid state MAS NMR, surface characterization.

Kursfassung

Die Mechanochemie ist eine effekive und überzeugende Methode zur Herstellung von Alumniumhydroxidfluoriden ($Al(OH)_{3-x}F_x$) mit einem sehr geringen Fluorgehalt. Durch den Prozess des Mahlens werden strukturelle Defekte in den Kristalliten erzeugt, die zu einer zunehmenden Amorphisierung des Kristallsystems führen. Die partielle Fluorierung von Alumniumhydroxid während des Mahlprozesses führt dabei zu einer noch stärkeren Amorphisierung und zur Bildung von Alumniumhydroxyfluoriden. Eine wichtige Rolle bei der resultierenden Produktzusammensetzung spielt die Variation der Synthesebedingungen, wie der Grad der Fluorierung, der Dauer des Mahlprozesses und des Wassergehalt der Edukte.

Folglich wurde zuerst der Einfluss von Wasser und dessen Bedeutung durch die verschiedenen Kombinationen von Oxid- und Hydroxid- ($Al(OH)_3$, Al_2O_3), sowie Fluorid-Quellen mit oder ohne Kristallwasser (β-$AlF_3{\cdot}3H_2O$, α-AlF_3) bei der mechanochemischen Synthese von hochgestörten Alumniumhydroxidfluoriden untersucht.

Um den optimalen Fluorierungsgrad zu ermitteln, wurden verschiedene Aluminiumhydroxidfluoride mit Al/F-Molverhältnissen von 1:1.5 bis 1:0.05 über die mechanochemische Syntheseroute hergestellt. Eine tiefergehende Charakterisierung der Struktur- und Oberflächeneigenschaften der entsprechenden Produkte erfolgte mittels XRD, ^{27}Al- und ^{19}F-Festkörper-NMR, thermischer Analyse, Stickstoffabsorptions- und Zeta Potentialmessungen. Mit γ-$Al(OH)_3$ und β-$AlF_3{\cdot}3H_2O$ als Hydroxid- und Fluorid-Quellen wurden dabei ab einem Verhältnis Al:F von 1:0.25 und hin zu höheren Fluoridanteilen besonders ungeordnete Strukturen erzeugt. Der Fluorierungsgrad betrifft dabei besonders die Ausbildung von 4- und 5-fach koordinierten Al-Zentren, die sonst nicht in den Edukten vorkommen. Diese Spezies beeinflussen die Bildung von Alumniumoxid und ermöglichen den Phasenübergang zu α-Al_2O_3 schon bei tieferen Temperaturen.

Der Einfluss der Mahldauer auf die Struktur und Oberfläche wurde am Beispiel von γ-Al_2O_3 im Detail untersucht. Die mechanochemische Synthese beeinflusst dabei die Absorption von Fluor an der Grenzschicht von γ-Al_2O_3 zu Wasser stark. Die Dauer des Mahlprozesses gewinnt daher einen großen Einfluss auf die entstehenden Produkte. Da Fluor nicht im Bulk von γ-Al_2O_3 vorkommt, kann mit der ^{19}F-Festkörper-NMR eine

Zuordnung der unterschiedlichen an der Oberfläche adsorbierten F-Spezies getroffen werden.

Stichwörter: Mechanochemie, Fluor, Festkörper-NMR, Oberflächencharakterisierung.

Acknowledgement

Firstly, I would like to thank prof. Kemnitz for having given me the chance of being part of his research group. It was a pleasure to work with him and I could not have imagined having a better advisor for my Ph.D. study.

I would like especially to express my gratitude to Dr. Scholz for her continuous support in the last four years, for her patience, her insightful comments and her constant encouragement.

My sincere thanks also go to my colleagues for the help and stimulating discussions, for all the bbq and the coffee breaks, the Ausflüge and the “Prost”. It was fun.
In particular, I would like to thank Lukas for our endless conversations about the golf swing, la licenza di pesca, dates, belly boat and exercises for becoming supple leopards; and Bea, the best part of my years in Adlershof. Te quiero muchissimissimo.

Last but not least, I thank my big amazing family and all my dear friends, Berliners and non, for all the love they give me.

Contents

Chapter 1. Introduction and Aim

Materials based on metal oxides are becoming increasingly important in the application of emerging technology. In many of those applications, including surface coatings and medical implants, metal oxides inevitably come into contact with water during their use. For this reason, a detailed understanding of metal oxide/water interactions, which define oxide formation as well as dissolution, is indispensable for the design of oxides with requested properties and for ensuring their stability over time. In this contest, the CRC 1109 (Collaborative Research Centre) founded by the DFG (Deutsch Forschungsgemeinschaft) has proposed a four-year project to investigate such a fundamental understanding which has not yet been reached. The purpose is to comprehensively describe the behaviour of oxide/water interfaces. To succeed in this goal, the involvement of several length scales must be taken into account, ranging from nanoparticles to crystalline and amorphous bulk.

Within the project, this Ph.D. work has a particular focus on the study of the interaction between water and aluminium (hydr-) oxides. With the specific aim to succeed in the synthesis of amorphous aluminium (hydr-) oxide fluorides by mechanochemistry and to understand the role played by water in this process. One of the greatest goals of Materials Science is the design of modified solids in order to synthesize functionalized material for specific applications. The mechanochemical synthesis is a well-known method in the ceramic industry to generate new surfaces and to introduce numerous defects. The number of defects due to the combination of mechanochemistry and fluorine supply is substantially high. The introduction of a small quantity of fluorine through mechanochemical approach leads to the formation of highly distorted aluminium hydroxide fluorides. The purpose of this fluoride doping is to control the introduction of structural distortions by chemical means. The influence of a varying fluorine supply on local Al-coordinations is also an important aspect of this work.

This Ph.D. thesis is divided into seven chapters. Each of them has the goal to give a comprehensive overview of the research line followed in this project. The chapters containing experimental data are organized by the modulation of a given variable (i.e. fluorination degree, water supply, milling time). A short description of each chapter follows.

Chapter 2 explains in detail potential applications of mechanochemistry and how it can allow access to amorphous (hydr-) oxide fluorides. A state of the art and preliminary

works defined in order to frame the presented work in line with the recent research achievements.

Chapter 3 considers the effect of the mechanical impact on the structures and at the surfaces of each of the aluminium hydroxides and oxides ($Al(OH)_3$, α-, γ-Al_2O_3). An analysis of the characterization of the selected hydroxides and oxides before and after the milling treatment is made.

Chapter 4 introduces the important role played by the amount of fluorine involved in the synthesis of the formation of the products. Especially the influence of the fluorination degree on the amount of 4- and 5- fold coordinated Al sites was on the main focus.

Chapter 5 explores the influence of water on the process. Its relevance in the synthesis of amorphous aluminium hydroxide fluorides was evaluated considering separate combinations of O/OH ($Al(OH)_3$, Al_2O_3) and fluorine sources with or without structural water (β-$AlF_3 \cdot 3H_2O$, α-AlF_3).

Chapter 6 presents an alternative method of introducing fluorine at the surface of unmilled and milled γ-Al_2O_3, which was chosen among all the available aluminium transition phases thanks to its adsorption capability.

Chapter 7 presents conclusions and future outlook.

Chapter 8 provides a short description of all the materials and methods used in this work.

Chapter 2. Fluorination by Mechanochemistry

Fluoride doping in oxide minerals is a well-known phenomenon in nature. The most well-documented effect of fluoride is the replacement of an hydroxyl ion in the apatite structure with this ion, giving rise to a reduction of crystal volume and a concomitant increase in structural stability [1, 2]. The purpose of fluorine doping is the introduction of structural distortion by chemical means. This implies the synthesis of fluorine doped almost amorphous aluminium oxides. The combined action of milling and fluorine doping should result in a substantial increase of the number of introduced defects. The as prepared aluminium hydroxide/oxide fluorides are expected to show an altered chemical behaviour, especially regarding their reactivity and solubility in water.

2.1 State of Art and Preliminary Work

The increasing interest on the synthesis of new fluoride based metal oxides is confirmed by the increasing of the number of published papers during the last years. This is thanks to their attractive perspectives in application fields as catalysts, optics, bio-labeling, composite materials, and biosensors. Many different approaches have been developed over the last decade and Fedorov et al.[3] published a detailed overview of all the available methods. Among these wide group of techniques, a non-aqueous sol-gel synthesis approaches have been just recently developed, thus extending the synthesis access toward nanoscopic metal fluorides and nanomaterials in general. It is shown that these nanoscopic metal fluorides obtained via this new synthesis approach exhibit. In particular, the non-aqueous fluorolytic sol-gel synthesis yields nanoscopic metal fluorides which exhibit distinctly different properties compared with their classical prepared homologs. Thanks to their extremely strong solid Lewis acidity, they allow new catalytic reactions with sometimes unexpectedly high conversion degrees and selectivity. More interestingly, metal hydroxide fluorides can be obtained via this synthesis route, otherwise not accessible via any other approach. The unique sol-gel fluorination synthesis of metal fluorides developed in our group [4, 5] opens to a variety of possibilities for the preparation of diverse catalysts. **Figure 2.1** resumes the main steps of this synthesis in which a metal alkoxide or any other suitable precursor is dissolved in an alcohol or any other suitable organic solvent.

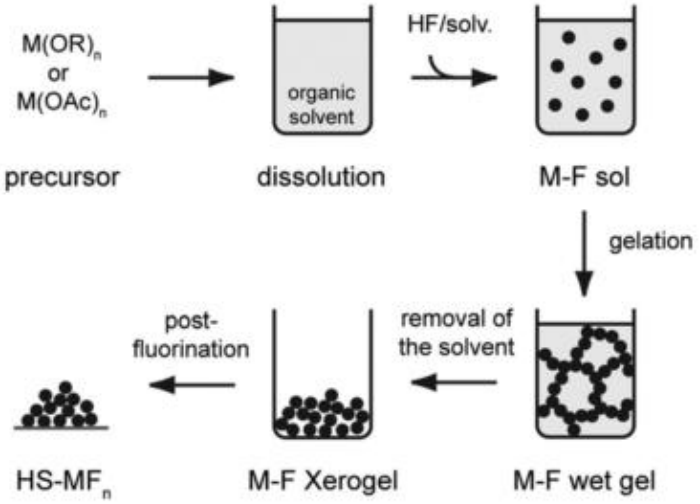

Figure 2.1: Illustration of the fluorolytic sol-gel synthesis starting from a metal alkoxide or carboxylate.

In this process, a solution of anhydrous hydrogen fluoride (from here the name of fluorolytic sol-gel process) is added in about stoichiometric amounts to the precursor solution, leading to the formation of a clear, translucent sol (temperature range 100–250 °C), which may become a gel, depending on the concentration, type of precursor and solvent (230–280 °C). The outcome of the fluorolytic reaction is not affected by varying the alkoxide from methoxide, ethoxide, isopropoxide or butoxide. Due to the possible presence of residues of the solvent after its removal (260-320 °C), a thermal post-treatment is performed in order to obtain an organic free, high surface (HS) metal fluorides xerogel as a final result. Most of the as-synthesized metal fluorides are totally X-ray amorphous or anyway highly distorted.

Beside this special sol-gel synthesis developed in our group in 2003 and just briefly explained above, mechanochemical techniques revealed also a great potential for the synthesis of highly distorted metal fluorides [6–8]. Among all the metal fluorides characterized in our group and the used synthesis techniques, the attention of this Ph.D. work is focused on the formation of aluminium hydroxide fluorides by mechanochemistry. In particular, the great potential of the mechanochemical approach was already shown by our group in several publications during the last decade [7-10].

2.2 Why Mechanochemistry?

Scientific challenges and environmental considerations have inspired the search for simple and energy-efficient syntheses. So far the necessary energy for activating a chemical reaction is usually provided by light (photochemistry), heat (thermochemistry) or electric potential (electrochemistry). Mechanically induced chemistry exploits instead of the mechanical force (action) produced from balls shaking rapidly inside a metal cylinder to drive chemical reactions. This kinetic energy replaces the most common energy sources in chemistry mentioned above. Stirrers and heaters are replaced by automated ball mills, and beakers and flasks by jars.

As above mentioned, the purpose of fluorine doping is the introduction of structural distortion by chemical means. Structural and topological changes are related to the defects introduced by mechanochemical means. The focus of this Ph.D. thesis, as will be explained later in more details, is the influence of water on the mechanochemical preparation of fluorine doped amorphous oxide samples. What is the state of art on this topic and what is the advantage of using high energy ball milling as synthesis technique?

2.2.1 From the Beginning to Nowadays

The so-called mechanochemistry has a long history, which covers the last two centuries[11]. The first documented application of a mechanical stimulus to induce chemical reactions in organic system (derivatives of quinhydrone) is probably the work of Ling and Baker in 1893 [12]. In 1919 the term "mechanochemistry" was introduced by Ostwald[13] when he examined and considered all the different ways of supplying energy able to promote chemical changes. Ostwald also commented the discoveries made by Carry Lea, considered as the father of mechanochemistry, in his book. The most influent published papers concerning mechanochemistry in the last forty years were well summarized in the book "Mechanochemistry in Nanoscience and Mineral Engineering" and also reported here (**Table 2.1**) for a complete understanding of the temporal development of this field.

Table 2.1: Overview of important published papers concerning applications of mechanochemical processes in the period of time between 1962 and 2006.

Title	Author(s)	Years
Mechanochemische Reaktionen [14]	Peters	1962
Review of the Phase Transformation and Synthesis of Inorganic Solids obtained by Mechanochemical Treatment [15]	Lin and Nadiv	1970
Mechanically Initiated Chemical Reactions in Solids [16]	Fox	1975
Mechanochemistry of Inorganic Solids [17]	Boldyrev	1986
Accelerating of Kinetics of Low-Temperature Inorganic Synthesis [18]	Roy	1994
Colloid-chemical Aspects of Mechanical Activation [19]	Juhasz	1998
Mechanochemistry of Solids: Past, Present, and Prospects [20]	Boldyrev and Tkacova	2000
M.Carey Lea, the first Mechanochemist [21]	Takacs	2004
Mechanochemistry: The Mechanochemical Activation of Covalent Bonds [22]	Beyer and Clausen-Schaumann	2005
Mechanochemistry and Mechanical Activation of Solids [23]	Boldyrev	2006

It was only in the last two decades though that the application of mechanochemical force to chemical systems has revealed successful results thus promoting an exciting period of the rediscovery of the field. Potential areas of application are numerous: pharmaceutical materials [24, 25], catalysis [26], synthesis of advanced materials [27, 9], green technology [28]. "The historical development of mechanochemistry" was written in 2013 by Lazlo Takacs [11], which follows the main developments until recent results and current trends. The transformation of inorganic substances, especially metal oxides and metal alloys, is actually the main goal of the mechanochemical research. In this regard, Šepelák et al. published in 2013 a comprehensive overview [29], with a special spotlight on the progress in heterogeneous and homogenous mechanochemical reactions in

oxides of various structure. An increasing number of reviews with a different focus is available online and a collection of the most significant ones with the simple title of "Mechanochemistry" (2013) allows an easy access to all of them [30].

The major inspiration behind the rediscovery of mechanochemistry is the so-called green chemistry, specifically the need for a cleaner, safer and more efficient transformations than the conventional routes can lead. How is this achievable? One of the most appealing aspects of mechanochemistry is that it does not require solvents. Eliminating or drastically reducing solvents would go a long way to moderating chemistry's environmental impacts because solvents make up most of the waste in the reactions, many of them are harmful to people and to the environment and a lot of them are produced from fossil fuels. Beside this, mechanochemistry gives access to materials and molecules otherwise inaccessible and reactivity that is difficult to achieve in solution. It offers fewer processing steps compared to the traditional processing routes; it is also suitable for the low cost, large-scale production of powders. Nowadays, milling is considered a reliable technique for the combination of different chemical elements, for the reduction of the particles size as well as for initiating solid state chemical reactions. Keeping in mind the long history of mechanochemistry and despite all the promising advantages, the underlying mechanisms are poorly understood and the comprehension of the kinetics of the mechanochemical reactions has still not reached a satisfactory level. This is maybe due to shortage of systemic studies and to the hard accessibility of the setup. Only recently real-time studies of the mechanochemical transformations [31] in a ball mill through the combination of two analytical techniques (time-resolved in situ X-ray diffraction (XRD) and Raman spectroscopy) lead to a more detailed analysis of the phenomena happening inside the milling jars.

2.2.2 High Energy Planetary Ball Milling

The "top-down" approach of mechanochemistry is based on providing the energy needed for physically breaking down coarse nanoparticles to finer ones. It relies on the principle of impaction and friction. **Figure 2.2** shows a potential positioning of the high energy mechanochemical within the other known processes. The mechanical grinding of dry reactants does not include any heating, except for the heating that results from the conversion of the mechanical energy of grinding into heat. The lack of control of the

reaction temperature is actually considered one of the biggest disadvantages of the high energy milling.

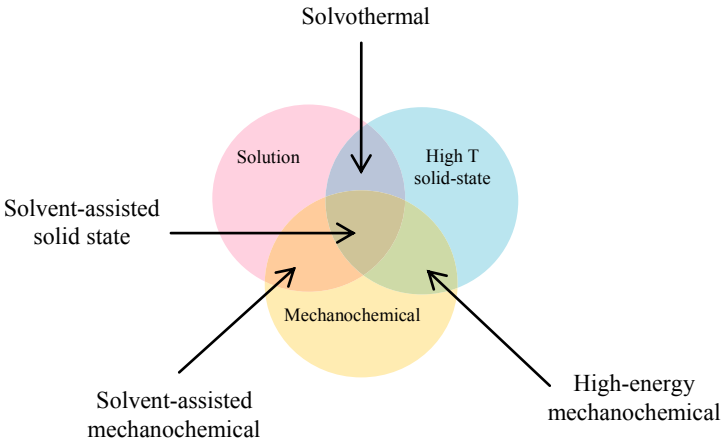

Figure 2.2: Relationship of high-energy mechanochemical synthesis to other known reaction processes. Adapted from ref. 32 with the permission from the copyright holder, Royal Society Chemistry.

One of the advantages of mechanochemical synthesis is that it requires very simple equipment that is widely available in chemistry laboratories. The two methods most frequently employed are simple manual grinding using a mortar and pestle or mechanical milling using an electrically powered ball mill. In spite of the developing popularity of many other technologies (stirred media mill[33], vertical roller mill, high pressure grinding roll), ball mill is widely used from minerals to chemicals. Considering for instance oxides, it induces a distinct kind of transformation such as disordering and amorphisation by introducing specific defects (in case of oxides, Schottky or Frenkel defects or crystallographic share planes).

The use of a planetary mill, included in the ball mill types, is also one of the options for replacing high-temperature reactions. It has the advantages of dry and wet operations, an easy set-up, a moderate cost and a simple cleaning procedure therefore very suitable for lab-scale process.

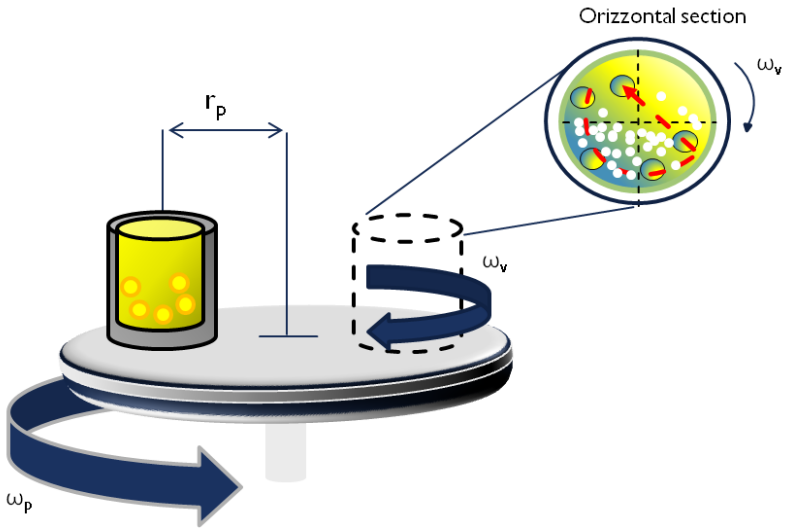

Figure 2.3: Scheme of the inner plate of a planetary ball miller. Signed movements are on a counter and in a normal direction; r_p: revolution radius. The zoom on the inside of the jar gives an idea about the motion of the balls. From the left to the right: cascading, cataracting and rolling [34].

Figure 2.3 provides a schematic representation of the inner of a planetary ball miller. The peculiarity of its setup is the simultaneous rotation of the plate and of the jars. In more details, the jars are attached to a metal plate which rotates around a common central axis (centrifugal rotation) while the jars (usually two) rotate simultaneously around their own axis (planetary rotation). The impact energy generated by the rotation of both defines an effective grinding performance. The energy transferred due to the impact and frictional forces produced by collision of the balls with the raw materials depends on many different parameters: rotational speed, velocity of the plate, number of balls (filling ratio of balls), filling ratio of the raw materials in the jars, ball to powder ratio, materials used for jars and balls, milling time (=reaction time). One of the most important parameter is the quantity of energy that is effectively transferred to the powder. All these parameters play an important role on the refinement of the particles of the starting materials.

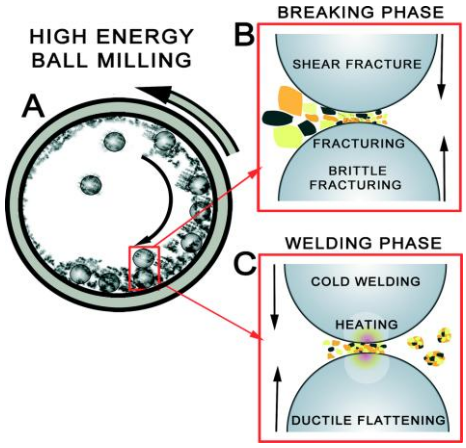

Figure 2.4: Schematic description of the high energy ball milling synthesis mechanism. (a) The content of the rotating (rpm) reaction chamber with hard balls and a mixture of the initial reactants at defined stoichiometric ratios which define the final product. (b) The breaking phase, where repeated fracturing of bulk reactants causes the formation of composite particles with desired compositions. (c) The welding phase, where small agglomeration of particles forms the final morphology of the powder. The scheme is referred to the synthesis of Cu-doped $BiVO_4$ nanoparticles and adapted from the Ref. 35 and with the permission from the copyright holder, Royal Society Chemistry.

The number of collisions, the velocity of the ball and therefore the energy of the impact are strongly influenced by the motion of the balls inside the jars. In turn, the pattern followed by the balls depends on the milling parameters. It changes from cascading to cataracting up to centrifugation or rolling in (as shown in the zoom in **Figure 2.3**) with increasing filling ratio and/or increasing revolution speed.

Many models were proposed in the last years[36, 37] for a better understanding of the kinetics of the mechanism that happens inside the jars. A major advance in this modeling became possible thanks to the development of the discrete element method (DEM). Very good reviews of the method can be found elsewhere [38-40]. In this scheme, the motions of each ball is traced and the interactions between balls are considered contact by contact. DEM has previously been implemented successfully to predict ball paths due to the ball and boundary interactions of high energy ball milling in horizontal, vibratory, and planetary mills. At the beginning of the simulation, balls are randomly positioned inside the milling vial and assigned small random velocities; the net momentum of the system is initially zero. For each time step, forces between balls are calculated for all contacting balls using the interaction force model. The new translational and rotational accelerations of the balls are calculated by Newton's

equation of motion. The new velocity and position of the balls are obtained by explicit integration of Newton's equation via the time-centered, finite-difference method.

Chapter 3. Mechanochemical Activation of Aluminium Hydroxides and Aluminium Oxides

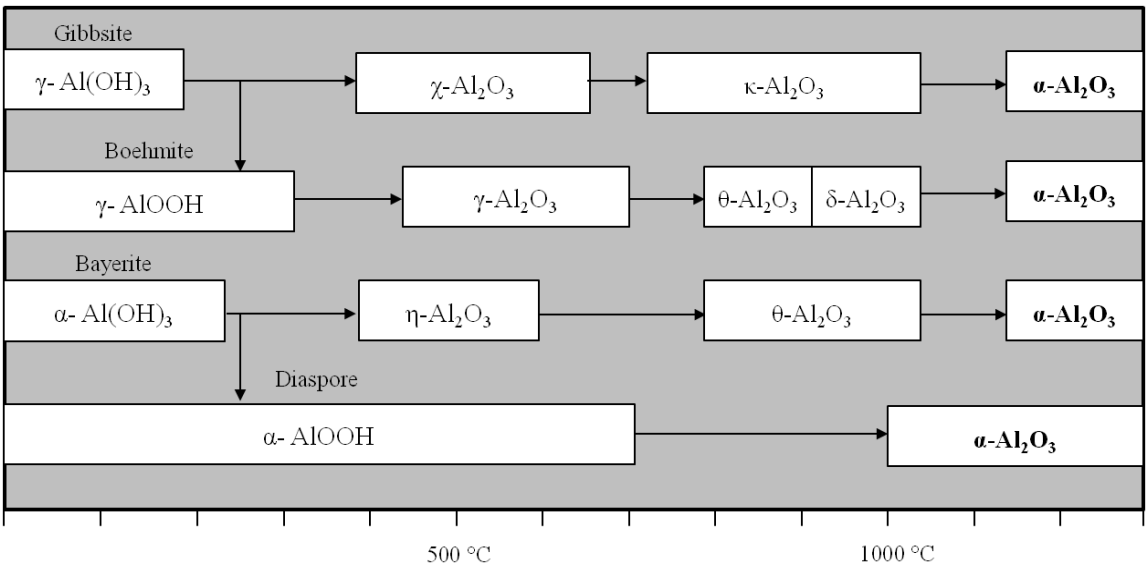

Figure 3.1: Scheme of the formation of transition aluminium oxide phases by increasing the temperature starting from aluminium hydroxides[41].

A preliminary study of the impact of the mechanochemical process on the structure and at the surface of the Al hydroxides and oxides is necessary to be able to discriminate between the amorphisation introduced by mechanochemistry and by fluorine.

As mentioned in the previous chapter, with nonconventional preparation techniques such as mechanosynthesis, in many cases non-equilibrium, metastable compounds are accessible. Understanding their formation processes might help improve their properties so that highly functionalized materials can be made available. Because of their fine particle size, high surface area, and catalytic activity of their surfaces, the transition aluminas find a lot of interest in material science. As a consequence of milling the number of introduced defects is high and as prepared aluminium hydroxides/ oxides are expected to show an altered chemical behaviour, especially concerning their reactivity and solubility in water. The planetary ball mill has been reported to induce mechanochemical phase transformations and reactions, the conditions of high stresses during milling are envisaged to play a major role in such phase transformations [42] reported on the phase transformation from γ to α Al_2O_3 by the use of this mill. Kostic et al. (2000) also reported on the phase transformation from γ to α by the use of a vibrating disc mill[43]. For instance, detailed studies of the chemical system (pseudoboehmites → corundum) revealed the great potential of mechanical milling[44,45]. In order to be able to distinguish the distortion introduced by milling, a detailed characterization of each reference sample is of fundamental importance for the better understanding of this

Thesis project. Aluminium oxide (alumina, Al_2O_3) exists in many metastable phases besides the thermodynamically stable α-Al_2O_3. Valuable alumina polymorphs are commonly produced by heating of aluminium (oxy) hydroxide as a precursor[46]. The path of transition Al_2O_3 during the heating processes is shown in **Figure 3.1**. On the next paragraphs, a description of the changes in the structure and at the surface of aluminium oxides introduced by milling effect is done.

3.1 Activation of γ-$Al(OH)_3$

Gibbsite (γ-$Al(OH)_3$), has a pillared structure where each pillar has a double layer of nearly close-packed oxygen ions with Al^{3+} ions occupying 2/3rd of the octahedral sites between the two layers. Remaining 1/3rd of octahedral voids are vacant. All aluminium ions lie on the midplanes between adjacent oxygen layers. Each oxygen is bound to a hydrogen atom. OH^- ions of adjacent layers are situated directly opposite to each other to have AB-BA-AB sequence. Because there are no aluminium ions between the adjacent hydroxyl layers, the basal plane is a weak cleavage plan [47]. The gibbsite structure is shown in **Figure 3.2**.

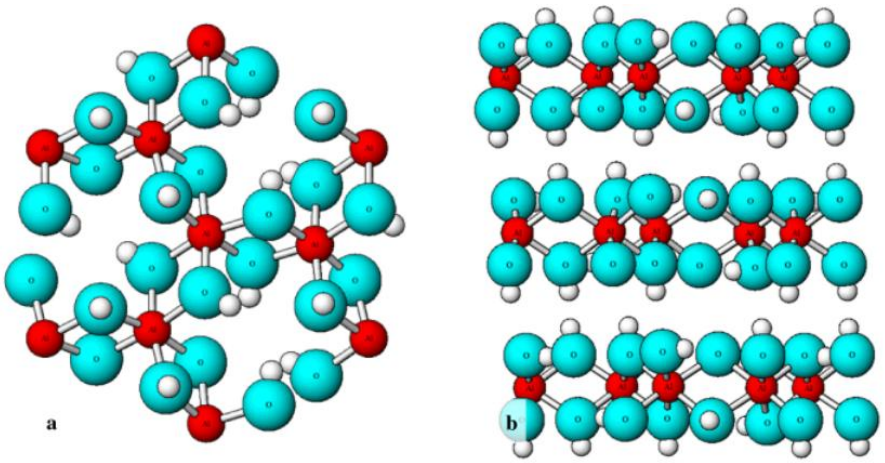

Figure 3.2: (a) View of a single layer of the gibbsite structure looking down upon the basal plane. (b) Side view of the gibbsite structure orthogonal to the basal plane. The light gray spheres represent the hydrogen atoms. Reproduced from Ref. 48 and with the permission from the copyright holder, John Wiley & Sons.

3.1.1 XRD Characterization

When many crystalline materials, including gibbsite, are submitted to milling, they are known to lose their long-range order and become X-ray amorphous[44]. As can be seen from the comparison between the X-ray diffractograms of the unmilled and milled samples (**Figure 3.3**), the impact of milling is strong enough to disrupt the typical layer structure of γ-$Al(OH)_3$.

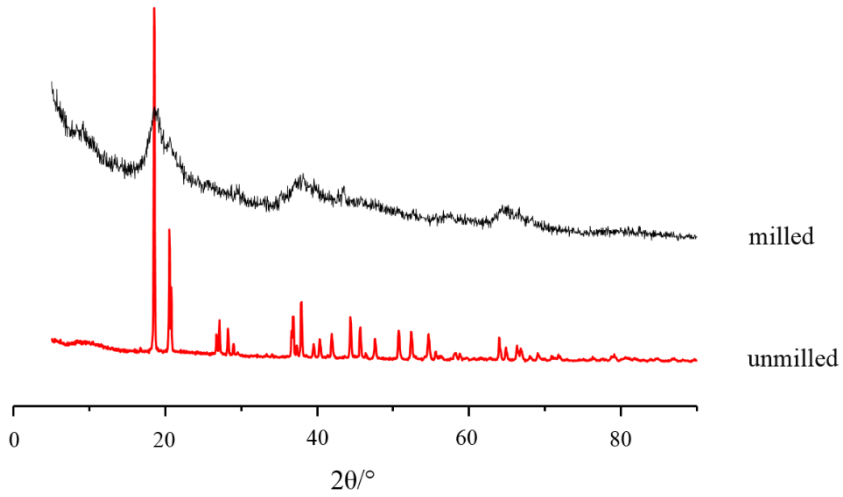

Figure 3.3: X-ray powder diffractograms of unmilled (red curve, PDF: 33-18) and milled (black curve) γ-$Al(OH)_3$.

After milling, the obtained powder is X-ray-amorphous. The pattern showed very broad maxima and the only peak still observable in the X-ray diffractogram is at 18.74 °. We observed also that the intensities of the gibbsite diffraction peaks weakened and broadened already after 1h of milling.

3.1.2 ^{27}Al MAS NMR Characterization

From the ^{27}Al MAS NMR spectra of the central transitions (**Figure 3.4**) it is apparent that gibbsite contains two nonequivalent Al atoms in octahedral environments, in agreement with the crystal structure determined by X-ray diffraction. The presence of these two distinguished ^{27}Al MAS NMR resonances characterized by rather similar chemical shifts but different quadrupolar coupling constants is explained only by the different character of the hydrogen bonds, in which the hydroxyl groups form the

corresponding octahedron around each Al site[49]. The structural disorder induced by the ball-milling process affects the Al coordinations.

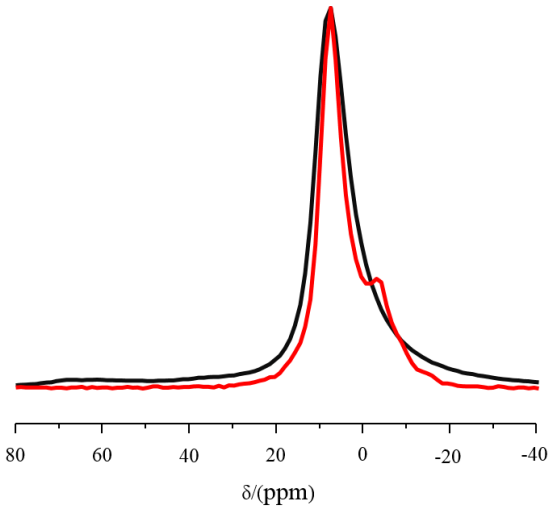

Figure 3.4: ^{27}Al MAS NMR spectra of unmilled (red curve) and milled γ-$Al(OH)_3$ (black curve). ν_{rot} = 20 kHz; na = 5000.

Indeed, the comparison of the normalized ^{27}Al MAS NMR spectra of the unmilled γ-$Al(OH)_3$ and 4h milled γ-$Al(OH)_3$ (**Figure 3.5**) shows that the milling process has introduced two additional resonances, one at ~65 ppm corresponding to an AlO_4 coordination, and one at ~35 ppm corresponding to an AlO_5 coordination (**Figure 3.4**, **Figure 3.5**). Due to the introduced disorder by milling, the two six-fold coordinated Al-sites are no longer distinguishable.

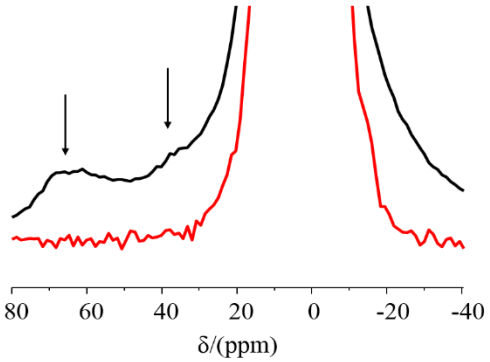

Figure 3.5: ^{27}Al MAS NMR spectra of unmilled (blue curve) and milled γ-$Al(OH)_3$ (black curve). Focus on the resonances at 65 ppm (5-fold coordinated Al sites) and 35 (4-fold coordinated Al sites) ppm introduced by milling. ν_{rot} = 20 KHz.

The comparison of the ^{1}H MAS NMR spectra of the unmilled and milled gibbsite (**Figure 3.6**) shows how the milling is able to destroy its layer structure, as it was shown already in the X-ray diffractogram (**Figure 3.3**).

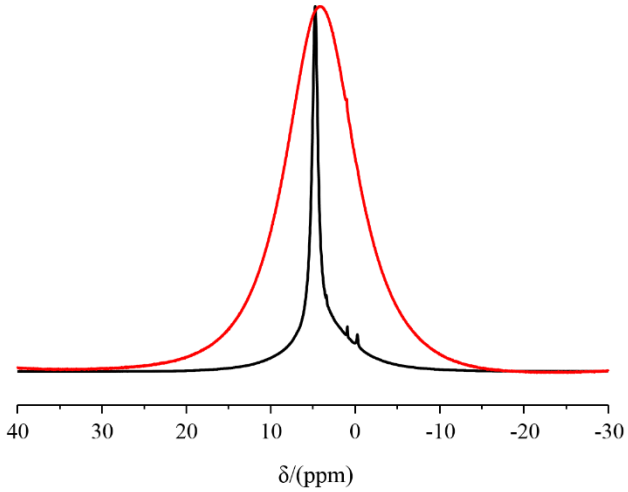

Figure 3.6: ^{1}H MAS NMR spectra of unmilled (red curve) and milled (black curve) γ-$Al(OH)_3$. ν_{rot} = 20 kHz; na = 256.

The ^{1}H MAS NMR spectrum of the unmilled sample shows a broader line. A distribution of different OH-groups can be observed. Due of the disruption of the layer structure by the milling impact and the introduction of subcoordinated Al-sites mobile water can be re-adsorbed and is visible with the narrow line at ~5 ppm in **Figure 3.7**.

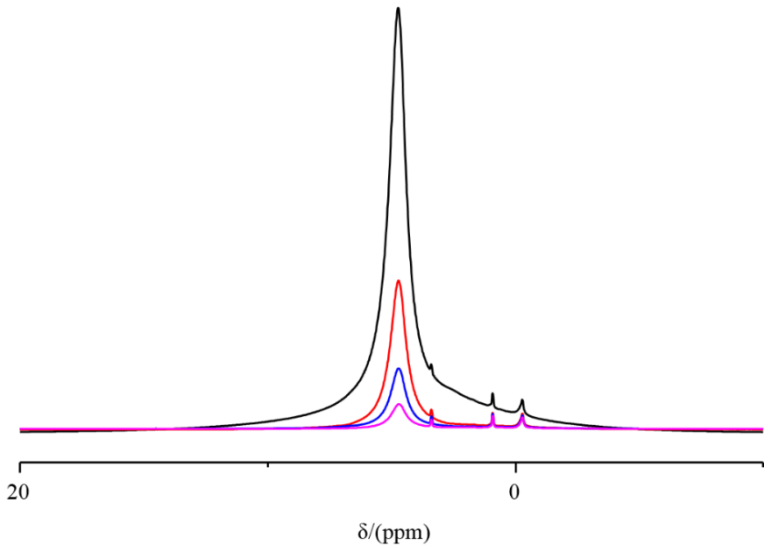

Figure 3.7: ^{1}H rotor-synchronized spin-echo MAS NMR spectra of milled γ-$Al(OH)_3$. Black line: L_0= 0; red line L_0= 10; blue line: L_0= 20; fucsia line: L_0= 30.

3.1.3 Zeta Potential Characterization

The traditional view, well defined by the multisite model (MUSIC), prevailed for quite a long time[50]. The purpose of this surface complexation model is to describe the adsorption behavior of many oxide surfaces. They can be helpful for understating adsorption behavior qualitatively. It was believed that the surface hydroxyl groups bound to two Al atoms (doubly coordinated aluminol sites, $Al_2(OH)$ on the basal plane were proton inactive and could not contribute to charging over the pH range 0-11.9. Gibbsite particles are typically hexagonal prismatic in shape. Because there are no aluminium ions between the adjacent hydroxyl layers, the basal plane is a weak cleavage plane. Mostly the basal planes (001) are occupied by $Al_2(OH)$, whereas AlOH and Al_2OH groups are equally distributed on the edge side[50,51]. Unlike the doubly coordinated surface hydroxyl groups, the charge of the singly coordinated hydroxyl group is not neutralized. As a result, the basal planes and the doubly coordinated OH species sites on the edge planes are not reactive. The point of zero charge of gibbsite has been found to be different for the edge plane (IEP around 11) and basal planes (IEP around 5) due to their dissimilar charging characteristics. The pH sensibility of surface charge of edge plane is greater than the one of surface charge of the basal plane. The observed point of charge is, then, between that of the edge plane and basal plane depending on the contribution from each surface. The solubility of gibbsite increases dramatically as pH is either decreased or increased. Only at low pH (below pH 4 or 5) the Al^{3+} ion prevail in a state where it is coordinated by six water molecules. At pH > 7, the $Al(OH)_4^-$ ion has the aluminium coordinated by four-fold hydroxide ions. As pH increases, the metal cation reacts with hydroxide anions in solution progressively to produce soluble hydrolysis products according to the solution equilibria. The basal plane too is (at least weakly) proton active at acidic pH and levels above pH 5. Thus, gibbsite does not belong to the group of minerals having only one type of mineral surface.

Comparing the curves (**Figure 3.8**) obtained for the unmilled sample and the 4h milled one, it can be easily seen that the milling process induces a change in the charging behavior of the sample. The IEP shifts from a value of 9.48 to one of 9.61. A shift in the IEP with milling suggests that alteration of the gibbsite surface has taken place during milling. Hiemstra et al.[50] accounted that as a result of the domination of single coordinated surface hydroxyl groups at the steps, vacancies and other defects in the

basal planes introduced by milling. The increase in zeta potential with milling may also have a similar origin, as there has been amorphisation by milling. The pH range of stability for the milled γ-$Al(OH)_3$ is 2 < pH < 8. The one for the unmilled sample is definitely smaller and involves low values of pH.

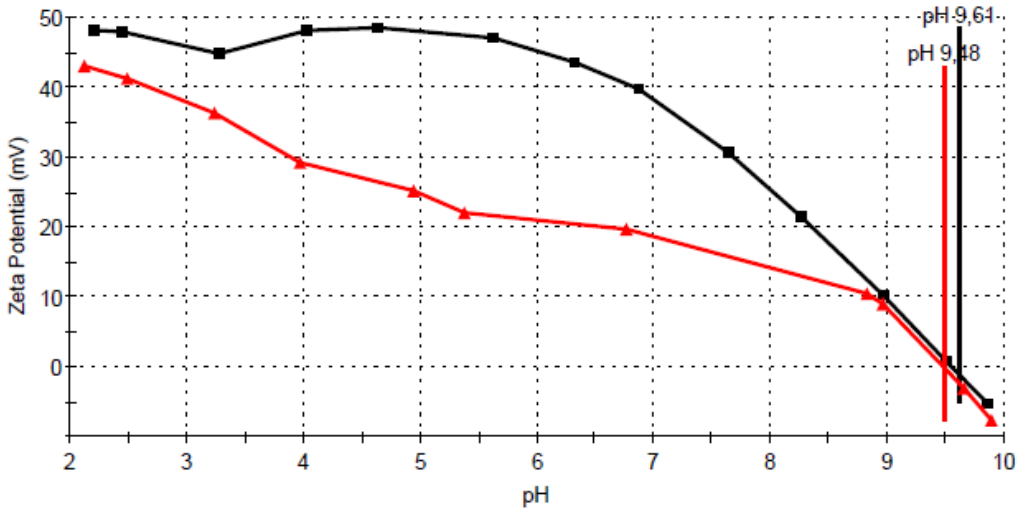

Figure 3.8: Zeta Potential vs pH curves of the unmilled (red curve) and milled (black curve) γ-$Al(OH)_3$.

3.1.4 TG/DTA Characterization

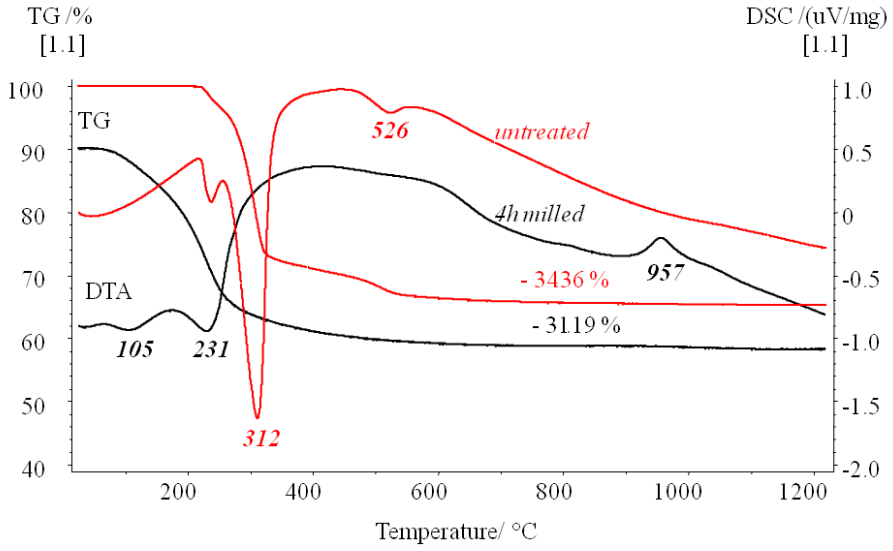

Figure 3.9: DTA and TG curves of unmilled (red curve) and milled (black curve) γ-$Al(OH)_3$.

The unmilled gibbsite shows a small endothermic peak at 238 °C (due to loss of water in the sample), a sharp endothermic peak at 312 °C and a weaker one at 526 °C (**Figure**

3.9). The total weight loss observed on the TGA curve in the T range 200- 820 °C was 34.36 %. This total loss of 34.36 % agreed well with the theoretical value of 34.6 % for the dehydration reaction. In the range of 200-280 °C only a small weight loss is observed (4 % approx.). This is probably due to adsorbed water which is not fully released. Up to the end temperature of the main peak (312 °C), the cumulative mass loss of the sample was 24 %, which approached the theoretical mass loss of γ-Al $(OH)_3$ to γ-AlOOH (23.08 %). So it is concluded that that the endothermic peak is induced by the conversion of γ-$Al(OH)_3$ to γ-AlOOH, which is accompanied by dehydroxylation reactions. While in the TG curve of the unmilled gibbsite no mass loss is appreciated for a temperature range from 100 °C to 200 °C, a mass loss of about 24 wt% is already visible in the same temperature range for the milled gibbsite. The endothermic peak at 526 °C indicates that boehmite transforms to amorphous γ-Al_2O_3. This endothermic peak disappeared after the milling of the sample, indicating that the milling conditions affected the transformation sequence of gibbsite. The total mass loss for the milled sample was lower, only 31.19 %. Obviously, a dehydroxylation already starts at milling which is only partially compensated by the adsorption of water on the surface. After milling for 4 h, an additional endothermic peak at 105 °C appeared. This is due to the release of the adsorbed water on the activated surface by milling. This result is in agreement with that observed in the ^{1}H MAS-NMR spectra (**Figure 3.6**). The course of the TG is in complete accord with the DTA curve. This indicates that endothermic peak results from weight loss by dehydration and that the milling enhances dehydration. Also, an exothermic peak at 957 °C was observed in the DTA curve of the milled sample, which corresponds to the early formation of the corundum. This confirms as well that the transformation sequence for gibbsite depends on the milling conditions.

3.2 Activation of γ-Al_2O_3

γ-Al_2O_3 is widely used as a catalyst support due to its high surface area to volume ratio, pore volume, and pore size distribution as well as its thermal stability and acid/base characteristics. Although many doubts are still related to the structure of γ-Al_2O_3, it is traditionally considered as a cubic system with face-centered cubic (fcc) oxygen packing. γ-Al_2O_3 has been described as defect spinel structure. An ideal spinel structure is shown in **Figure 3.10**. In γ-Al_2O_3, 8/3rd aluminium vacancies have been assumed

randomly distributed over the tetrahedral sites, so that the cationic sublattice is partially disordered as compared to the ideal spinel. The spinel structure adopted by γ-Al_2O_3 contains 16 octahedral and 8 tetrahedral cationic sites per unit cell in which 62.5 % of the available Al ions occupy octahedral sites and the remainder are tetrahedral [47] (**Figure 3.10**).

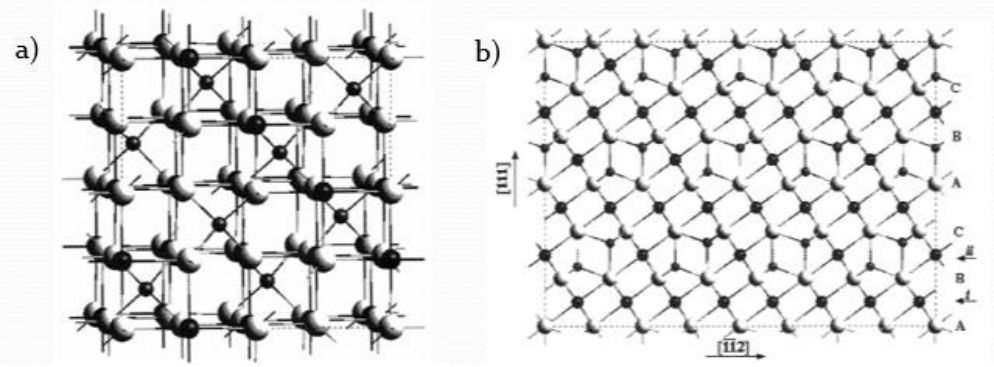

Figure 3.10: a) 3-D view of the spinel structure. White balls represent oxygen ions. Large dark balls represent 16d, octahedrally interstitial sites, and the smaller balls represent 8a, tetrahedrally coordinated sites. Presence of empty interstitial positions can also be observed. b) Ideal spinal structure projected along the [110] direction.

3.2.1 XRD Characterization

The X-ray diffractogram of the unmilled sample (**Figure 3.11**, red curve) shows the typical pattern of an almost amorphous sample[45]. After milling, already the presence of α-Al_2O_3 can be easily observed beside γ-Al_2O_3 [45, 52, 53].

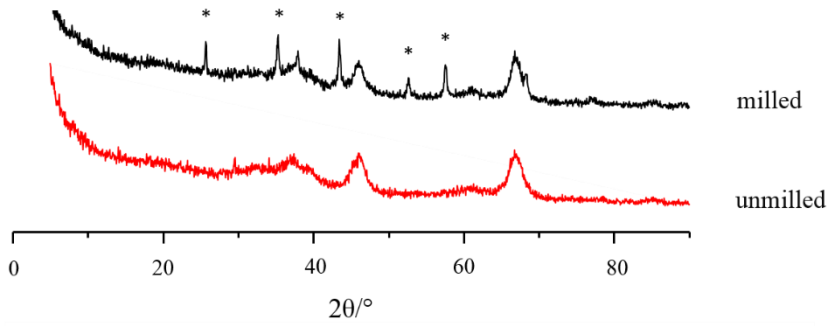

Figure 3.11: X-Ray powder diffractograms of unmilled (red curve, PDF: 10-425) and milled (black curve) γ-Al_2O_3; *: reflections of α-Al_2O_3.

Besides heat treatment, it is known that the γ to the α phase transformation of aluminium oxide can be initiated mechanically by ball milling at ambient temperature. The diffraction peaks observable in the X-ray diffractogram of the milled sample correspond to the typical peaks of the X-ray diffractogram of the α-Al_2O_3 (PDF: 10-173), beside still present γ-Al_2O_3.

3.2.2 ^{27}Al MAS NMR Characterization

^{27}Al MAS NMR is an effective tool for distinguishing local structures of the γ-Al_2O_3 phase from those the boehmite and the α-Al_2O_3. The Al coordination is exclusively octahedral in both the α-Al_2O_3 and boehmite phases, whereas it is roughly 70% octahedral and ~30% tetrahedral in the γ-Al_2O_3 phase. The expected resonances for the tetrahedral and octahedral Al-coordination are recorded at approximately 67 ppm and 10 ppm, respectively. Normalizing the spectra to the height of the signal representing AlO_6 (**Figure 3.12**), it is visible that the milling process decreased indeed the amount of AlO_4. Grinding causes a marked decrease in the intensity of the ^{27}Al resonance at about 67 ppm in the γ-Al_2O_3 spectrum. The appearance of a small amount of a resonance at about 36 ppm can be attributed to additional five-fold coordinated Al-sites which stabilize the defect spinel structures of transition aluminas [54, 55].

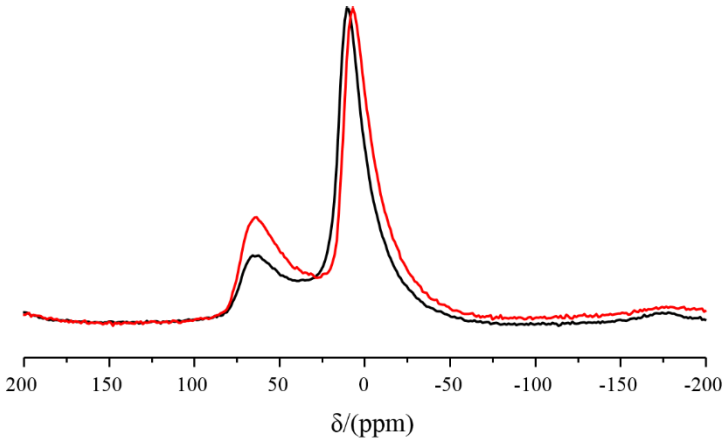

Figure 3.12: ^{27}Al MAS NMR spectra of unmilled (red curve) and milled (black curve) γ-Al_2O_3. ν_{rot} = 20 kHz.

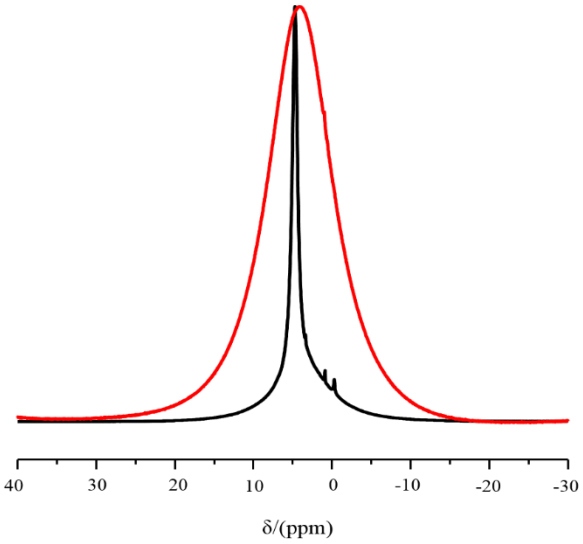

Figure 3.13: ^{1}H MAS NMR spectra of unmilled (red curve) and milled (black curve) γ-Al_2O_3. ν_{rot} = 20 kHz.

In **Figure 3.13**, the ^{1}H MAS NMR spectra of unmilled γ-Al_2O_3 (red curve) are shown. The position of the main peak is at 5.05 ppm. This peak is assigned to protons of physisorbed water molecules, showing a higher mobility in the case of unmilled γ-Al_2O_3. After milling the main peak is visibly broader because of the disorder introduced by milling.

3.2.3 Zeta Potential Characterization

Comparing the curves of the zeta potential measurements (**Figure 3.14**), any remarkable changing can be observed. The plateau visible at the ZP value of ~ +30 mV in the pH range 3.5 ÷ 7.5 is, after milling, reached a higher value of ZP (~ +34 mV) but the stability of this value is in a smaller pH range. The IEP of the milled sample is shifted toward a lower value of pH.

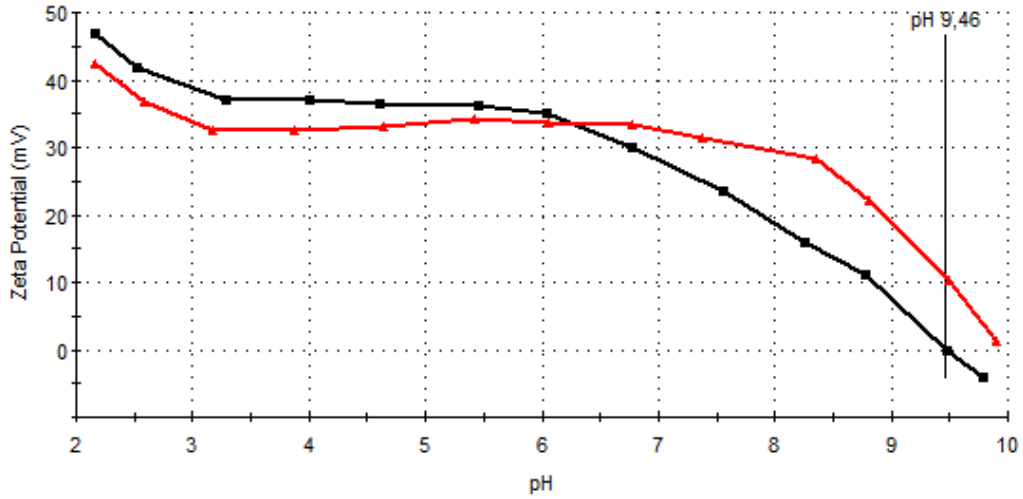

Figure 3.14: Zeta potential vs pH curves of unmilled (red curve) and milled (black curve) γ-Al_2O_3.

3.2.4 TG/DTA Characterization

In the thermoanalytical curves (**Figure 3.15**) the unmilled γ-Al_2O_3 shows a main endothermic peak, superimposed with a small exothermic peak below 600 °C with associated mass loss of ca. 9%. The mass loss up to this temperature must be due to the removal of adsorbed mobile water, which is in agreement with the removal of mobile water of milled γ-$Al(OH)_3$ observed at about 100 °C (**Figure 3.9**). Above 600 °C, the mass-loss curve becomes much flatter. Only the final ~1% appears to be due to the loss of residual hydroxyl groups from the γ-Al_2O_3. The exothermic peak at 1211 °C is due to the transformation to corundum. Little difference is observed in the shape of the mass loss curves for unmilled and milled samples, since in both materials the removal of water is gradual, and continues over an extended temperature range. The total water loss from both samples is similar, indicating that changes induced in the sample by milling do not involve, in that case, dehydration. However, as indicated in **Figure 3.13**, the adsorbed water of milled γ-Al_2O_3 is less mobile, resulting in a broadening and a shift of the endothermic peak to 150 °C. Since the α-Al_2O_3 produced by milling should not contain structural water, the water loss from these transformed regions must remain in the system as adsorbed water. As already observed previously (**Figure 3.11**, **Figure 3.12**), the phase transformation to corundum is shifted to lower temperature using milled γ-Al_2O_3.

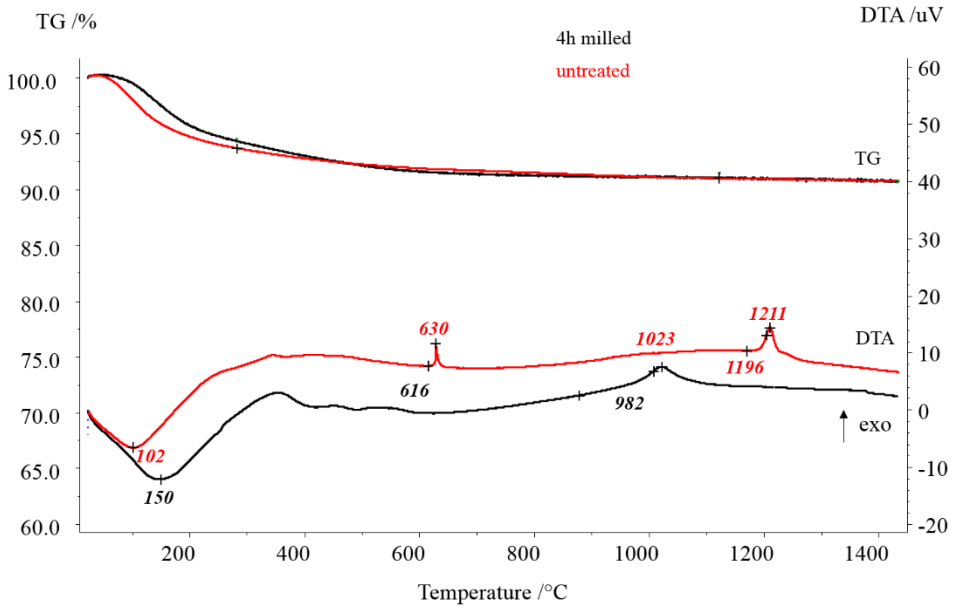

Figure 3.15: DTA and TG curves of unmilled (red curve) and milled (black curve) γ-Al_2O_3.

3.3 Activation of α-Al_2O_3

Corundum is the most stable and common crystalline form of alumina. The bulk structure of corundum has oxygen atoms arranged in approximately hexagonal close-packed layers. Between any two layers of oxygen (O) atoms, 2/3rd of the octahedral sites are filled with aluminium (Al) atoms in an ordered array. The Al atoms do not lie on the mid-plane between the oxygen layers. The Al atoms displace slightly toward the unoccupied octahedral site in the cation layer either above or below. The result is that an ordered half of the Al ions lay just above and half of the Al ions lay just below the mid-plane between the oxygen layers[56]. The structure of the α-Al_2O_3 is shown in **Figure 3.16**.

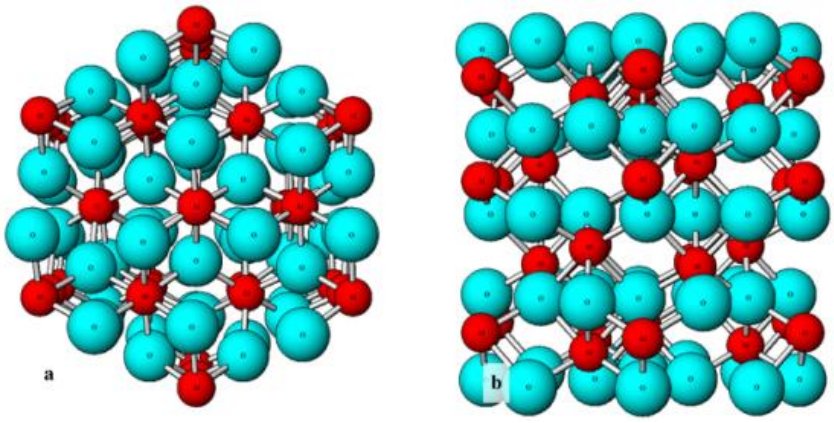

Figure 3.16: The α-alumina corundum crystal structure viewed along, (a) the <0001> direction (c plane) and (b) the < $10\bar{1}0$> direction. Blue spheres represent oxygen atoms and red spheres represent aluminium atoms. Reproduced from Ref. 48 and with the permission from the copyright holder, John Wiley & Sons.

3.3.1 XRD Characterization

The diffractograms show reflections of a crystalline phase (**Figure 3.17**, red curve) and a nanocrystalline probably partially amorphous phase (**Figure 3.17**, black curve) where the long-range order is to some extend almost lost. Obviously, the mechanical treatment results in a broadening of the diffraction peaks and in a decrease of their amplitudes. The decrease in the peak heights and the corresponding increase in the width of the peaks indicate a decrease in crystallite size, as said already. During the milling process, the alumina remains in the α-Al_2O_3 form, but the lattice expands. This may be due to the introduction of vacancies and other defects[56].

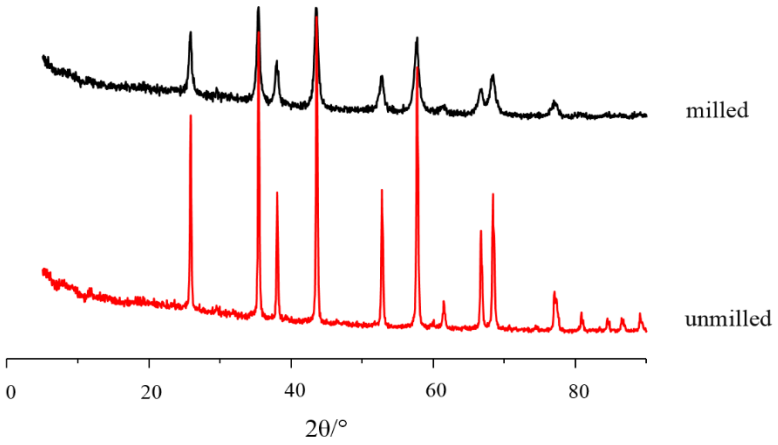

Figure 3.17: X-Ray powder diffractograms of the unmilled (red curve, PDF: 10-173) and milled (black curve) α-Al_2O_3.

3.3.2 ^{27}Al MAS NMR Characterization

As no extra central line appears which could be characteristic of 4- or 5-fold coordinated Al^{3+} ions, it can be noticed that the aluminium ions remain in a 6-fold oxygen coordination also after milling (**Figure 3.18**). As for the XRD patterns (**Figure 3.17**), only a line broadening effect can be observed.

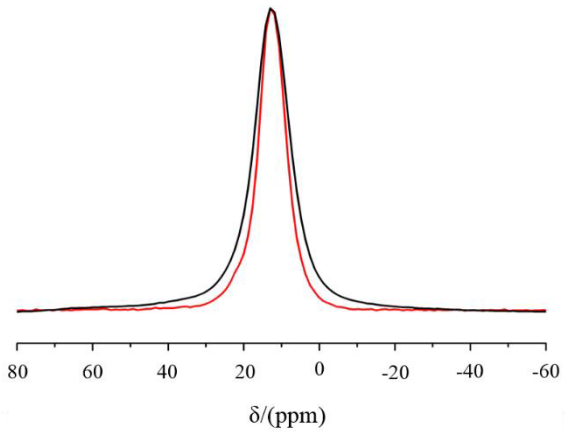

Figure 3.18: ^{27}Al MAS NMR spectra of unmilled (red curve) and milled (black curve) α-Al_2O_3.

The ^{1}H MAS NMR spectrum for the unmilled sample (**Figure 3.19**, red curve) shows peaks at 4.9 ppm, 3.5 ppm, 1.0 ppm and 1.7 ppm. These resonances can be attributed to isolated OH-groups (1.0 ppm), bridged OH-groups (1.7 ppm and 3.5 ppm) and adsorbed

water (4.9 ppm) at the surface of corundum. As observable from the spin-echo measurements, the peak at 4.86 ppm disappears increasing the dipolar evolution time. The introduced disorder at least at the surface of corundum only allows recording a ^{1}H spectrum enveloping the above-mentioned signals (**Figure 3.19**).

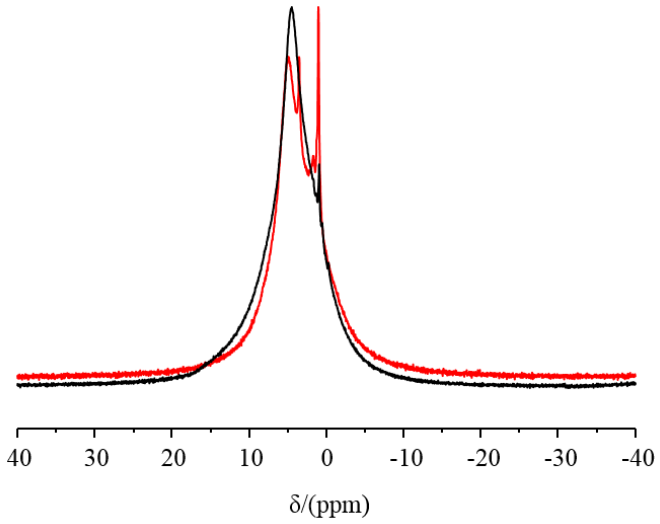

Figure 3.19: ^{1}H MAS NMR spectra of unmilled (red curve) and milled (black curve) α-Al_2O_3.

3.3.3 Zeta Potential Characterization

From the zeta potential data, shown in **Figure 3.20**, in both cases (unmilled sample, red curve and milled sample, black curve) lower pH values promise better dispersing efficiencies with respect to higher surface charges yielding more intensive repulsive forces. The results show that the suspension at acidic pH range generates good dispersion, which could be due to the high positive surface charge in an acid environment. As alumina is a basic oxide, it consumes H^+ ions and increases pH, resulting in positive surface charge at the surface in pure water[57]. The IEP of the untreated α-Al_2O_3 is found to be at pH 8.6, which is in close agreement with the reported value[58]. The curve displays the largest zeta potential decrease, compared with the other samples. This consequently affects the agglomeration state.

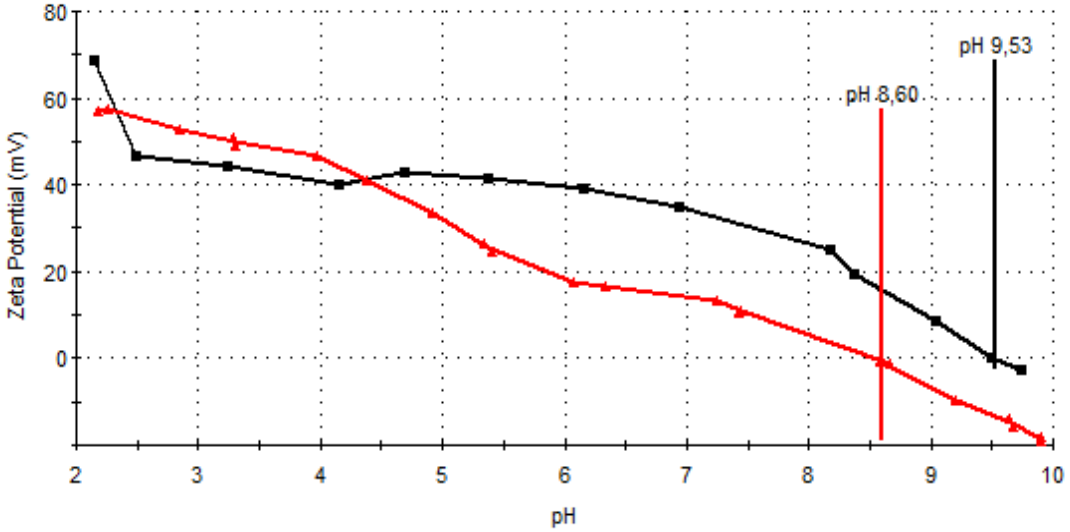

Figure 3.20: Zeta potential vs pH curves of the unmilled (red curve) and milled (black curve) α-Al_2O_3.

Measurements have shown that grinding induces modification of surface properties and the introduction of the defects leads to a shift of the IEP from a pH= 8.60 to a higher pH= 9.53.

3.3.4 FT-IR Characterization

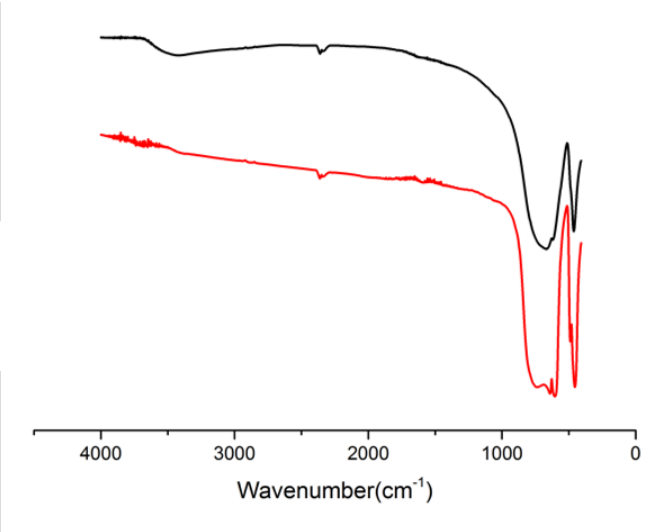

Figure 3.21: FT-IR spectra of unmilled (red curve) and milled (black curve) α-Al_2O_3.

The red curve in the **Figure 3.21** shows the FT-IR spectrum of the unmilled α-Al_2O_3. IR vibration bands at 456 cm^{-1}, 489 cm^{-1}, 605 cm^{-1} and 640 cm^{-1} are observable. As confirmed by the ^{27} Al MAS NMR spectrum (**Figure 3.18**), the bands in the 650 to 400

cm^{-1} range are typical for stretching vibrations in AlO_6-octahedral groups. After milling, all bands become broader. Supporting the result of ^1H MAS NMR the water content of the milled sample is higher, leading to a visible and broad vibration band at about 3500 cm^{-1} (**Figure 3.21**).

3.3.5 TG/DTA Characterization

Expectedly, no phase transition can be observed in the DTA curves (**Figure 3.22**) of the unmilled and milled samples. The only visible peak is an endothermic one in the DTA curve of the unmilled sample. This peak at 94 °C is induced by removal of absorbed water. The same peak is extremely broadened in the DTA curve of the milled sample but it is broader. As expected, no phase transitions are observed in both DTA curves. Considering the TG curve of the unmilled sample, mass loss is almost completed at 120 °C. Its value considerably decreases (5.92% loss), associated with the water eliminate on. Taking in account the TG curve of the milled sample, the mass loss is around 2.02%.

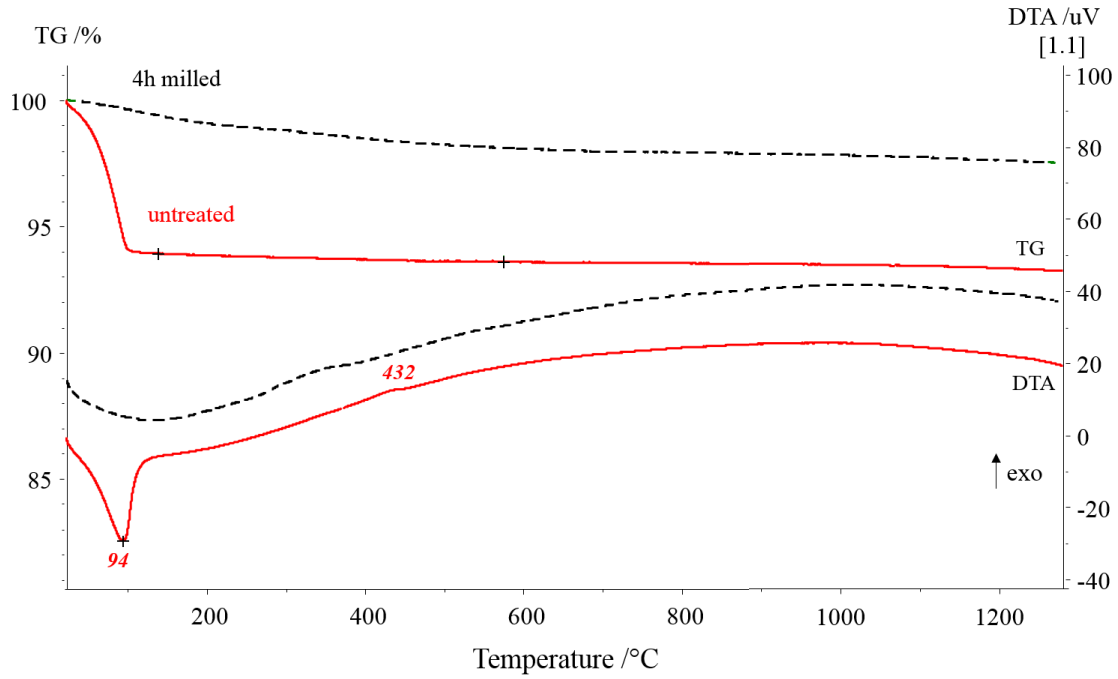

Figure 3.22: DTA and TG curves of unmilled (red curve) and milled (black curve) α-Al_2O_3.

3.4 Comparison of Zeta Potential Measurements

The coordination behaviour of Al^{3+} toward hydroxide ions explains the dependence of aluminium hydroxide solubility on the pH-value. Hydroxyl groups coordinated in various ways with aluminium cations constitute the reactive functional groups of alumina surfaces. They show different behaviour compared to the OH groups inside the bulk. For instance, in the bulk structure of corundum (α-Al_2O_3), the Al ions are hexacoordinated and the coordination number of oxygen is 4. At the surface, oxygens with a lower coordination can also be found, ranging from singly to triply coordinated surface oxygens. At the (110) face, for instance, equal numbers of singly [AlOH], doubly [Al_2OH], and triply [Al_3O] aluminium coordinated oxygen surface sites are present. In other polymorphic aluminium oxides, like γ-Al_2O_3, the situation is even more complicated because the Al ion is present not only in octahedral (Al^{VI}) but also in tetrahedral oxygen coordination (Al^{IV}), as confirmed by the ^{27} Al MAS NMR spectrum in **Figure 3.12**. The refined MUSIC model predicts a low proton affinity for the reactive groups $Al^{IV}OH^{1/4-}$ (log K = 5), $Al^{IV}Al^{VI}O^{3/4-}$ (log K = 7), and $Al^{VI}{}_3O^{1/2-}$ (log K = 6) using Pauling bond valences. The presence of these groups can be a reason for a lower PZC for some aluminium oxides[50].

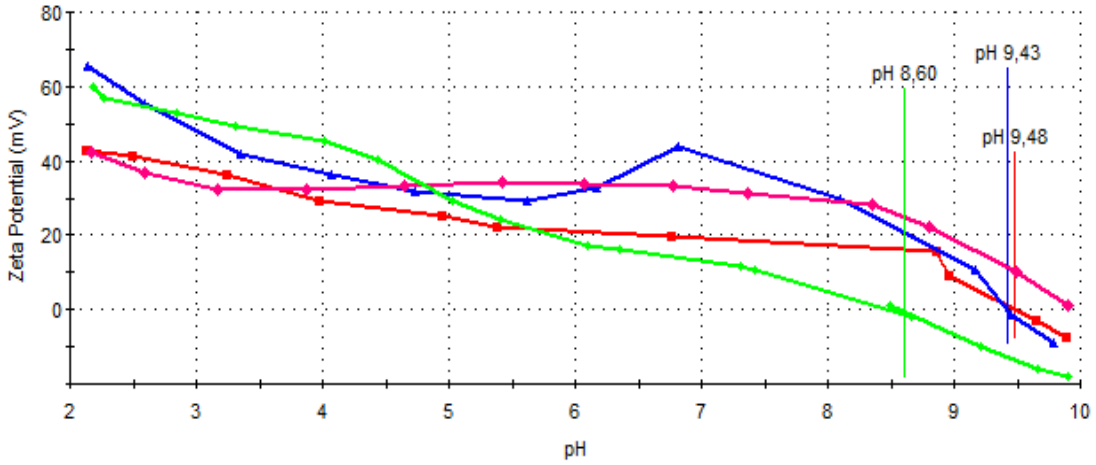

Figure 3.23: Comparison of the zeta potential vs pH curves of the unmilled samples. Red curve: γ-Al_2O_3; green curve: α-Al_2O_3; blue curve: γ-AlOOH; pink curve: γ-$Al(OH)_3$.

The ball milling is able to modify the surface properties of each sample. As it is shown in the **Figure 3.23**, the trend of the Zeta potential curves for all the milled samples is very similar. From a pH 3 to the pH 7 a plateau is observed for each sample. Such

plateaus were less distinct in the pH profile of the unmilled sample (**Figure 3.23**), especially for the α-Al_2O_3. The zeta potential values in this range of pH is for each sample higher than +30 mV and that is an indication that the suspensions are physically stable [59].

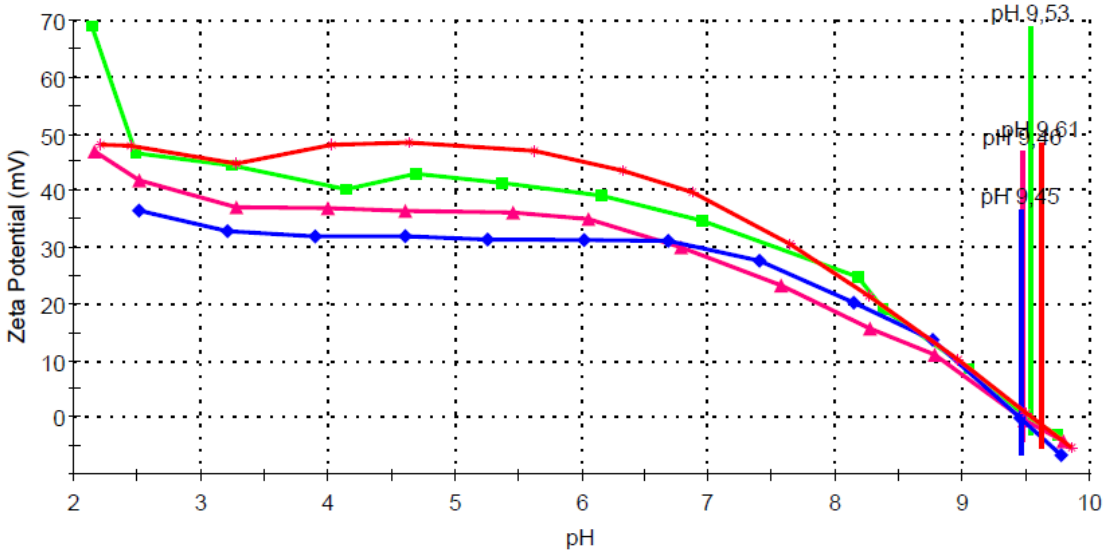

Figure 3.24: Comparison of the zeta potential vs pH curves of the milled samples. Red curve: γ-$Al(OH)_3$; green curve: α-Al_2O_3; blue curve: γ-AlOOH; pink curve: γ-Al_2O_3.

For an easier comparison of the IEP values, they were reported in the tables below. **Table 3.1** includes the IEP values for the unmilled samples and the **Table 3.2** the IEP values for the milled samples. After milling, all the samples display a shift of the IEP toward more basic range except the γ-Al_2O_3.

Table 3.1: IEP values of the unmilled reference samples.

Sample (unmilled)	**IEP (pH)**
γ-$Al(OH)_3$	9.48
γ-Al_2O_3	<10
α-Al_2O_3	8.60

Table 3.2: IEP values of the milled reference samples.

Sample (milled)	IEP (pH)
γ-Al(OH)$_3$	9.61
γ-Al$_2$O$_3$	9.46
α-Al$_2$O$_3$	9.53

One may conclude that the impact of the mechanochemical synthesis on the γ-AlOOH leads the sample to reach the properties of the phase transition of γ-Al_2O_3 (**Figure 3.25**), not just in terms of bulk properties but even of the surface chemistry.

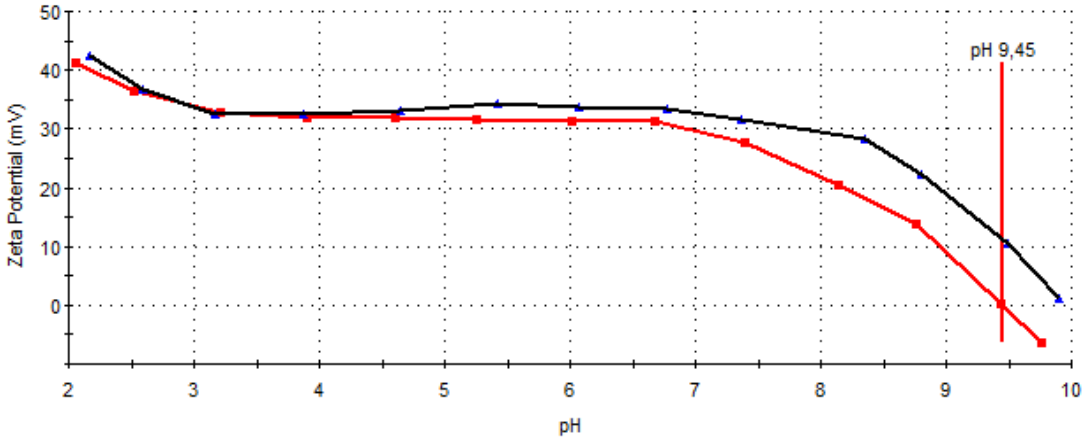

Figure 3.25: Comparison of the zeta potential vs pH curves of the milled γ-AlOOH and the unmilled γ-Al_2O_3.

Same consideration can be made for the properties of the γ-Al_2O_3 (**Figure 3.26**) reached after milling. The X-ray diffractograms have already shown how the γ to α phase transformation can also be initiated mechanically by ball milling at ambient temperature.

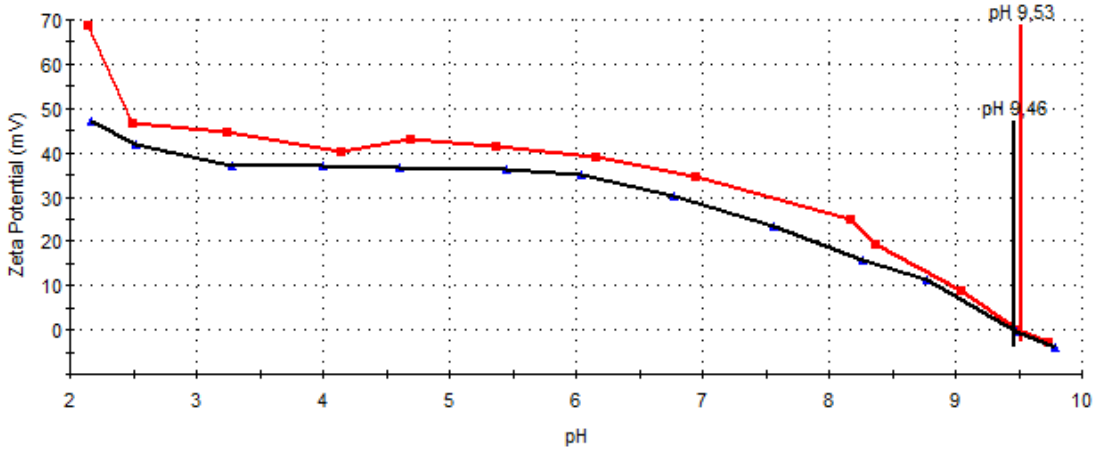

Figure 3.26: Comparison of the zeta potential vs pH curves of the milled α-Al_2O_3 (red curve) and of the milled γ-Al_2O_3 (black curve).

Chapter 4. Mechanochemical Synthesis of Low F-Doped Aluminium Hydroxide Fluorides

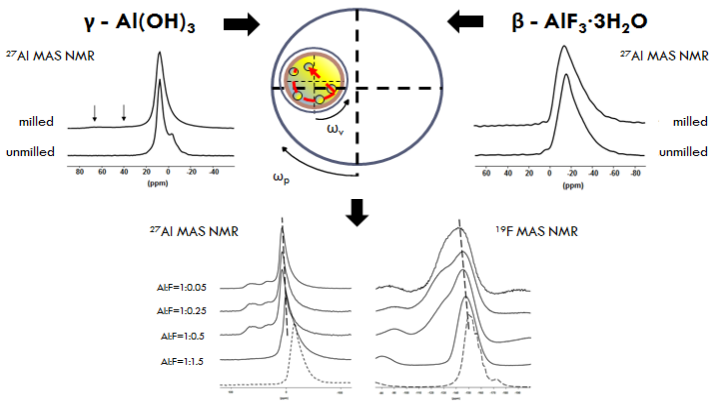

V. Scalise, G. Scholz, E. Kemnitz, *J. Solid State Chem.*, 243 (2016), 154-161.

On the main focus:

- Low F-doped Al-hydroxide fluorides can be successfully prepared by mechanosynthesis.
- Both F-doping and mechanochemical synthesis introduce a high number of defects in the structure.
- The fluorination degree affects the amount of 4- and 5-fold coordinated Al sites as well as the transition temperature to corundum.

Different aluminium hydroxide fluorides with varying Al/F molar ratios from 1:1.5 up to 1:0.05 were successfully synthesized by mechanochemical reactions. The characterization of the products by XRD, ^{27}Al and ^{19}F MAS NMR, thermal analysis, nitrogen adsorption and zeta potential techniques allows a detailed understanding of the structure and surface properties of the products. Using γ-$Al(OH)_3$ and β-$AlF_3 \cdot 3H_2O$ as OH- and F-sources, respectively, strongly disordered products were obtained with an Al: F molar ratio higher than 1:0.25. The fluorination degree has affected the amount of 4- and 5-fold coordinated Al sites, not present in the reactants. This amount of sub-coordinated species results dependent on the temperature of a calcination process. An evolution of the sub-coordinated Al-species has been detected also as a consequence of annealing processes. Obviously, these species affect the phase transition to alumina, by decreasing the transition temperature of the formation of α-Al_2O_3. Synthesis conditions (milling time, fluorination degree) play a crucial role in the product composition.

4.1 Introduction

The successful mechanochemical synthesis of nanocrystalline aluminium hydroxide fluoride samples $AlF_x(OH)_{3-x}\cdot 3H_2O$ with pyrochlore structure was also previously shown by our group[9]. In fact, for x= 1.5 the reaction was almost complete according to equ. (1).

$$Al(OH)_3 + \beta - AlF_3 \cdot 3H_2O \rightarrow 2AlF_x(OH)_{3-x} \cdot nH_2O + 2H_2O \quad (1)$$

Well resolved reflections of the aluminium hydroxide fluoride with pyrochlore structure were observed. Changes in the amplitudes and line widths of the reflections with increasing milling impact allowed an estimation of the crystallite sizes applying the Scherrer-equation[60]. Surprisingly was, in this case, the circumstance that a higher impact results for this mechanosynthesis in a better crystallinity (larger crystals). This morphological peculiarity explains the higher temperature for the observed phase transition to corundum as compared to the less mechanically treated sample[10]. A classical solid state chemical reaction at high temperature does not lead to the same result.

Starting from the same reference system, in the present chapter we reduced the fluorine supply from Al: F= 1: 1.5 down to 1: 0.05 in order to prepare highly distorted aluminium oxide/hydroxide fluorides. The introduction of even low dopant amounts modifies the chemical composition and causes a disruption of the crystalline atomic structure of the reactants. Following that, as prepared aluminium hydroxide fluorides are expected to show altered local structures as well as an altered chemical behaviour, especially concerning their reactivity and solubility in water. In the present study mechanochemical reactions of these two reactants, γ-$Al(OH)_3$ and β-$AlF_3\cdot 3H_2O$, were performed with different Al: F ratios down to 1:0.05 without further subsequent chemical treatment. The influence of the mechanical impact and the F-doping was evaluated by X-ray powder diffraction, ^{19}F and ^{27}Al MAS NMR and FT-IR spectroscopies. The thermal behaviour of the samples was studied by DTA-TG, the characterization of the specific surface areas was performed using the BET method and the analysis of their dissolution behaviour and stability in aqueous solution was made by zeta potential measurements. In order to be able to distinguish the distortion introduced

by milling and the one introduced by fluorine doping, a detailed characterization of each reference sample was peculiar, as described in the previous chapter.

4.2 XRD Characterization

Milling of γ-$Al(OH)_3$, as shown in the previous chapter, essentially causes the disruption of the pillar-like structure of the matrix of γ-$Al(OH)_3$, producing the characteristic broad features of an almost X-ray amorphous material (**Figure 4.1**, f). On the other hand, β-$AlF_3 \cdot 3H_2O$ remains, after milling, nearly unchanged as indicated by XRD (**Figure 4.1**, a, b), showing only a small broadening of the individual reflections accompanied by a slight decrease of their amplitudes. Although β-$AlF_3 \cdot 3H_2O$ itself contains theoretically all the elements (Al, F, O, H) necessary for a mechanically initiated transformation into $AlF_x(OH)_{3-x} \cdot nH_2O$ without any impurities, this does not occur at milling. **Table 4.1** gives an overview of the products identified by XRD measurements obtained from the mechano-synthesis applying different Al: F molar ratios.

Table 4.1: Overview of products of the mechanochemical reaction between γ-Al(OH)3 and β-$AlF_3 \cdot 3H_2O$ based on XRD measurements. * Pyrochlore structure.

MOLAR RATIO	REFLECTIONS
AL: F= 1: 1.5	$AlF_x(OH)_{3-x} \cdot 3H_2O$, $Al(OH)_3$ *
AL: F= 1: 1	$AlF_x(OH)_{3-x} \cdot 3H_2O$, $Al(OH)_3$ *
AL: F= 1: 0.5	$AlF_x(OH)_{3-x} \cdot 3H_2O$, $Al(OH)_3$ *
AL: F= 1: 0.25	X-ray amorphous, $Al(OH)_3$
AL: F= 1: 0.1	X-ray amorphous
AL: F= 1: 0.05	X-ray amorphous

For lower Al: F ratios, well-resolved reflections of aluminium hydroxide fluoride with pyrochlore structure (PDF-number: 41-0381) can be observed immediately, as already demonstrated[9]. These reflections are observable with a really good resolution for a molar ratio Al: F= 1: 1.5, (**Figure 4.1**, c). Increasing the Al: F ratio (that corresponding with decreasing F-content) results in broad reflections that indicate a higher degree of

disorder in the products. However, in all mechanochemical reactions of the two reactants the reflections of β-$AlF_3 \cdot 3H_2O$ disappear completely (**Figure 4.1**, **Table 4.1**).

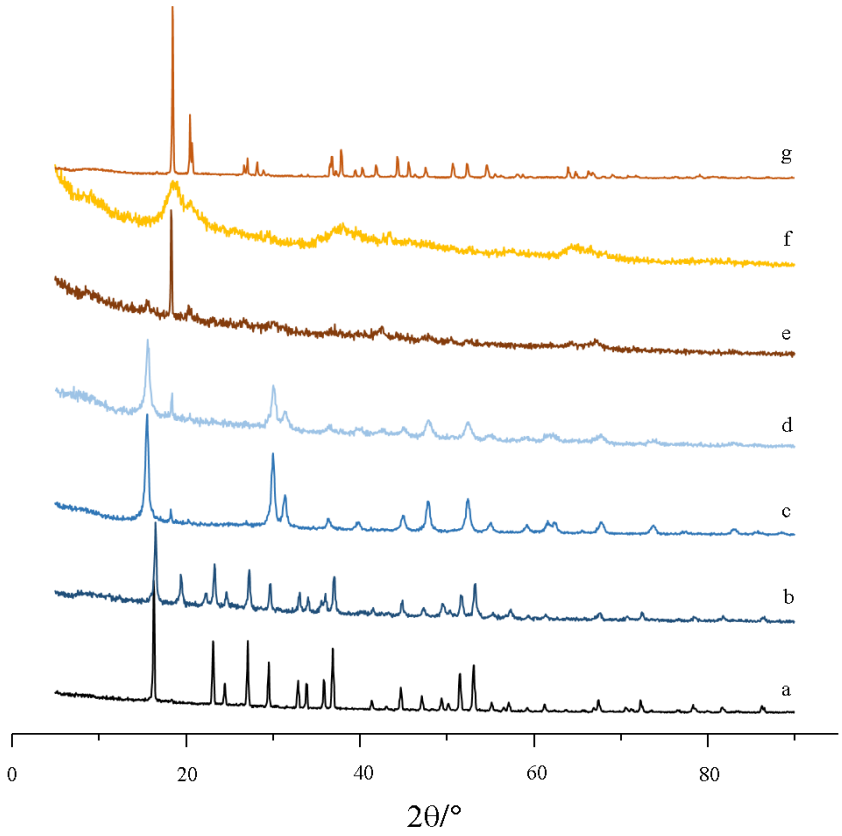

Figure 4.1: X-ray powder diffractograms of samples prepared by reaction of γ-$Al(OH)_3$ (g, PDF: 33-18) and β-$AlF_3 \cdot 3H_2O$ (a, PDF:1-203) in a molar ratio of: c) Al: F= 1: 1.5; d) Al: F = 1: 1; e) Al: F = 1: 0.25. For comparison: f) X-ray diffractogram of the milled γ-$Al(OH)_3$ and b) of the milled β-$AlF_3 \cdot 3H_2O$.

4.3 ^{27}Al and ^{19}F MAS NMR Characterization

Figure 4.1 shows the ^{27}Al MAS NMR spectra of the unmilled and the milled γ-$Al(OH)_3$. In all crystal forms of aluminium hydroxides (γ-$Al(OH)_3$, α-$Al(OH)_3$), the Al ions occupy octahedral sites. The ^{27}Al MAS NMR spectrum of unmilled γ-$Al(OH)_3$ indeed contains the signals of the two non-equivalent Al atoms in octahedral environments, as it can already be deduced by the presence of two distinguished resonances (**Figure 4.2**, 1.a) [61]. The structural disorder induced by ball-milling immediately affects the Al coordination. The crystalline order of the γ-$Al(OH)_3$ is destroyed by milling, resulting in the formation of-an amorphous alumina system. As a consequence of milling, the two central lines (**Figure 4.2**, 1.b) are broadened and two additional resonances, that show the presence of Al in 4-fold (~64 ppm) and 5-fold (~36 ppm) coordination appear

(**Figure 4.1**, 1 indicated by arrows) [62]. **Figure 4.2,** 1 shows the ^{27}Al MAS NMR of the unmilled and milled β- $AlF_3 \cdot 3H_2O$. **Figure 4.2**, 2 and 3 clearly indicate that the milling does not have the same strong impact on the structure of the β- $AlF_3 \cdot 3H_2O$ as on the γ-$Al(OH)_3$ structure. In its ^{27}Al MAS NMR, the maximum of the main signal is at about -15 ppm, which is a typical value for aluminium fluorides with bridging fluorine atoms. The asymmetric decay to the upfield of the central line, which indicates the local disorder at the aluminium sites, is observable already before and also after milling. In the ^{19}F MAS NMR spectra the main peak is detected at -155 ppm (**Figure 4.3**). The rigid chain structure allows observing six different species in agreement with literature [63]. But the observed ^{19}F chemical shift values can only be explained taking into account the strong H-bridging network[64]. The position and the intensity of the central peak do not change significantly after milling. The small peak at around -173 ppm disappears after milling.

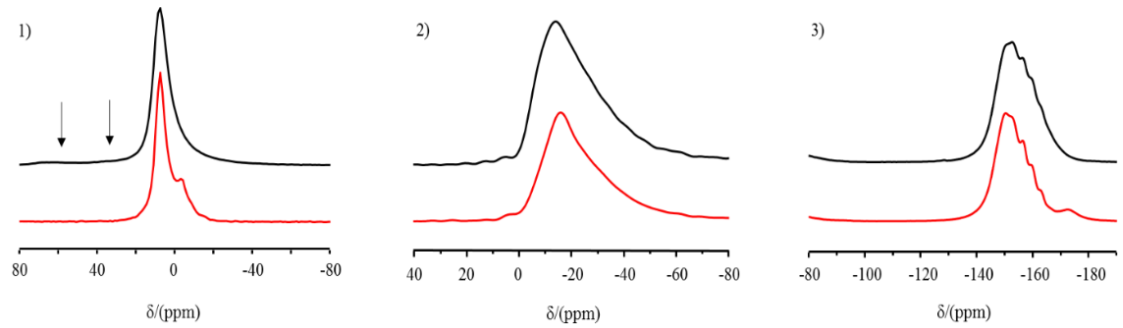

Figure 4.2: ^{27}Al MAS NMR spectra (central lines, ν_{rot}= 20 kHz) of 1) γ-$Al(OH)_3$, 2) β- $AlF_3 \cdot 3H_2O$, 3) ^{19}F MAS NMR spectra of β- $AlF_3 \cdot 3H_2O$; red line: unmilled samples, black line: milled samples. ↓ underline the rise of the signals at 64 ppm and 36 ppm.

Figure 4.3 presents both the ^{27}Al and ^{19}F MAS NMR spectra of the products obtained by milling with a different Al: F molar ratio. For comparison, the spectra of the unmilled β-$AlF_3 \cdot 3H_2O$ are given on bottom. Since it was already shown that the impact of milling on the β-$AlF_3 \cdot 3H_2O$ was not so significant, the spectra of the milled β-$AlF_3 \cdot 3H_2O$ are not added for an easier legibility of the figure. The combined action of the F-doping and the milling causes a significant increase of the intensities of the signals corresponding to the sub-coordinated Al-species (64 ppm corresponding to the 4-fold coordinated Al atoms and 35 ppm to 5-fold coordinated Al atoms). The intensity of the 35 ppm and the 64 ppm resonances does not increase proportionally to the introduced amount of fluorine. The product which exhibits the highest amount of 4- and 5- fold coordinated Al atoms was synthesized with a molar ratio Al: F=1:0.25.

The ^{27}Al MAS NMR spectrum of the sample obtained with a molar ratio Al: F= 1: 1.5 (**Figure 4.3**, b) ensures the presence of only 6-fold coordinated Al-species: a shoulder at 6.3 ppm, indicating residues of AlO_6 species or also AlF_1O_5-species, the main peak at 0 ppm and another shoulder (that defines an asymmetric decay to the upfield) at -12 ppm typical for AlF_6 species[65]. Al is surrounded by a mixed fluoride/oxide environment in this pyrochlore structure. Decreasing the amount of fluorine, the main signal of 6-fold coordinated Al-sites shifts to lower field (from 0 ppm to 7 ppm, (**Figure 4.3**, b-e). The ^{19}F MAS NMR spectra of the products exhibit a high field shift of the maxima with higher fluorine content. The broadening of the main peak is proportional to the decrease of the fluorination degree and an additional shoulder, strongly low-field shifted, occurs. In any case, all the signals lay within a region of δ_{cs} = -115 ppm and δ_{cs} = -152 ppm.

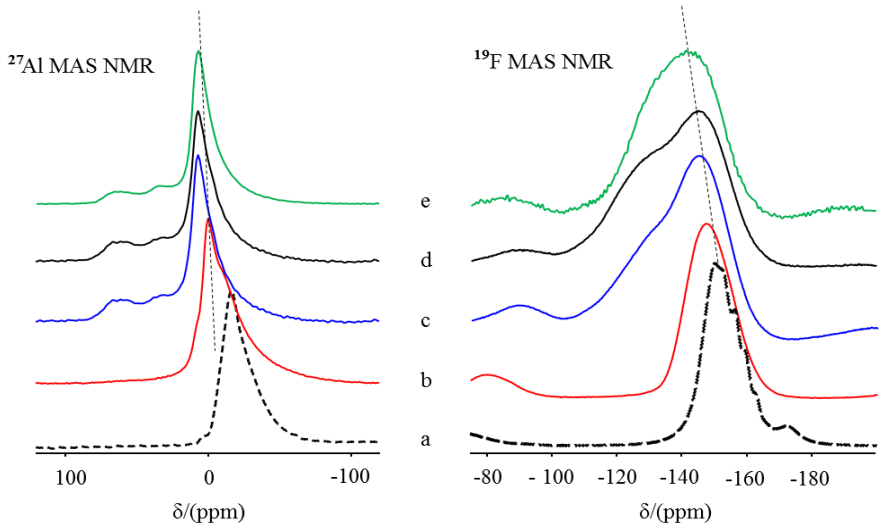

Figure 4.3: ^{27}Al and ^{19}F MAS NMR spectra (central lines, ν_{rot} = 20 kHz) of the products after mechanochemical reaction in a molar ratio Al: F of b) 1: 1.5; c) 1: 0.5; d) 1: 0.25; e) 1: 0.05. The spectra of β-$AlF_3 \cdot 3H_2O$ (a) are added for comparison.

Especially the high-field region corresponds to a typical region for bridging F-sites in octahedral AlF_xO_{6-x}[64]. The low-field shifted shoulder issues parallel to the appearance of Al in 4- and 5-fold coordination.

A simulation of the ^{27}Al MAS NMR spectra can lead to an estimation of the percentage amount of different Al coordinated species. Since the Czjczek model allows a quantitative decomposition of the spectra for highly distorted systems[66], the simulation of the ^{27}Al spectra was performed using this distribution function for each species. Due

to the high numbers of defects introduced by the combined action of F-doping and ball milling (also experienced by the rising up of the 35 ppm and 64 ppm resonances), a quantitative description of the different Al-sites is difficult. For a better separation of the resonances, a higher magnetic field NMR (14 T, 600 MHz) measurement of the product with the highest amount of 4- and 5- fold coordinated Al atoms was performed in addition (Figure 4, blue line: spectrum, black dotted line: simulated spectrum). As can be seen, the higher magnetic field allows detecting well distinguishable resonances, which can be comparatively easy simulated applying distribution functions.

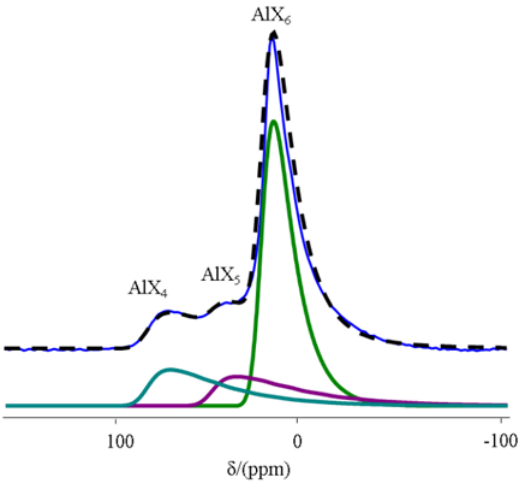

Figure 4.4: ^{27}Al MAS NMR spectra of the product obtained with a molar ratio Al: F=1:0.25 (blue curve); simulated spectrum (black dotted curve) by using DMFIT software. (B_0 = 14 T; ν_{rot} = 27.5 kHz).

In **Table 4.2** the main parameters used for the simulation of the ^{27}Al MAS NMR (B_0 = 14 T) spectrum (**Figure 4.4**) of the product synthesized with a molar ratio of 1:0.25 are summarized. Due to the limited access to the 14 T NMR spectrometer, all the other spectra were performed applying a magnetic field of 9.4 T.

Table 4.2: Parameters obtained by the simulation of the ^{27}Al NMR spectrum (B_0 = 14 T; ν_{rot} = 27.5 kHz) of the product synthesized with a molar ratio of 1:0.25. ν_Q = value of the quadrupolar product of the Czjczek distribution; FWHM CS = Full Width at Half Maximum of the isotropic chemical shift distribution; Position = isotropic chemical shift.

Species	ν_Q (kHz)	FWHM CS (ppm)	Position δ_i (ppm)
Al^{VI}	788	8.0	10.7
Al^{V}	1429	8.2	41.5
Al^{IV}	1250	10.6	74.5

The isotropic chemical shift δ_i and the quadrupolar product $\nu_{Q\eta}$ were derived for each species by considering the deconvolutions of the spectra. Parameters of the simulations are given in **Table 4.3**. The deviation of the parameters obtained with a 14 T magnetic field is negligible for four- and five-fold coordinated Al-sites and clearly noticeable for the 6-fold coordinated Al-sites is clearly. This can be explained considering the presence (confirmed by X-ray measurements) of residues of γ-$Al(OH)_3$ in the matrix (cf. **Figure 4.1**.e). A superposition of the signals of six-fold coordinated Al-sites makes the simulation of the spectrum for these contributions more complicated.

Table 4.3: ^{27}Al MAS NMR parameters obtained by the simulation of each spectrum (B_0 = 9.4 T) for milled products with a molar ratio Al: F higher than 1.

Sample		1:0.5	1:0.25	1:0.1	1:0.05
Al^{VI}	δ_i (ppm)	12.6	12.4	13.1	12.1
	$\nu_{Q\eta}$ (kHz)	730	659	680	730
Al^{V}	δ_i (ppm)	39.8	41.5	41.8	42.2
	$\nu_{Q\eta}$ (kHz)	938	1429	1000	938
Al^{IV}	δi (ppm)	74.5	76.2	74.2	73.3
	$\nu_{Q\eta}$ (kHz)	999	1250	940	999

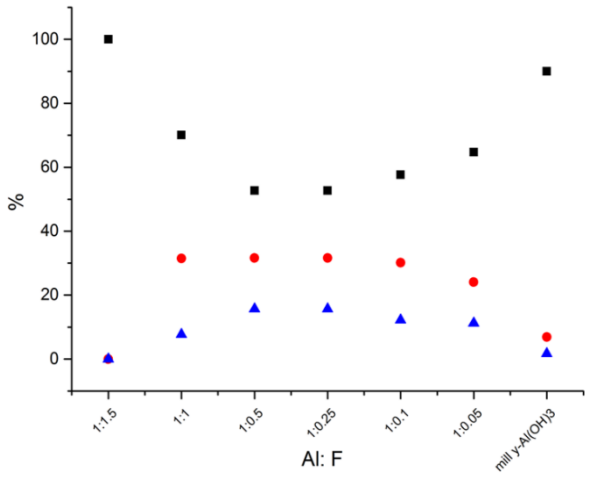

Figure 4.4: Amount of 4- (▲), 5- (●), 6- (■) fold coordinated Al-species vs the molar ratio Al: F. The average (%) amount was obtained by decomposition of the spectra of each sample.

The results of the simulations are outlined in **Figure 4.4** where the relative intensity of the signals of the 6-, 5-, 4- fold coordinated Al sites is plotted versus the molar ratio Al: F. The relative intensity of each signal group of the 4h milled γ-$Al(OH)_3$ spectrum is added for comparison. The graph can be divided into two different regions: one characterized by an almost linear reduction of the 6-fold and an evolution of the 5- and 4- fold coordinated Al sites; the other shows the opposite trend. The separation point of these two regions is represented by the Al: F=1: 0.25 sample. The highest relative amount of sub-coordinated Al-species was detected for this sample, as readily observable.

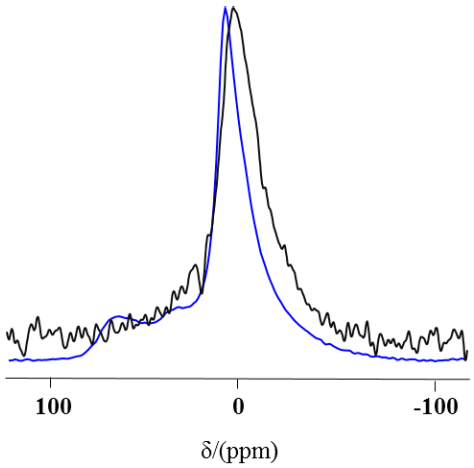

Figure 4.5: $^{19}F \rightarrow {}^{27}Al$ CP MAS NMR of the product obtained with a molar ratio Al: F= 1: 0.25 (gray curve). The blue curve is the ^{27}Al MAS-NMR spectrum of the same sample, added for comparison.

The application of $^{19}F \rightarrow {}^{27}Al$ CP MAS NMR (**Figure 4.5**) technique can selectively enhance the Al signals of the aluminium atoms in the neighbourhood of F atoms.

The comparison of the CP MAS NMR of the product obtained with a molar ratio of Al: F = 1: 0.25 with the ^{27}Al MAS-NMR spectrum of the same sample reveals that at least in the surrounding of the two species at about 30 ppm and 2 ppm there must be fluorine. In fact, the appropriate peaks could be further depicted. The products obtained with a molar ratio of Al: F=1: 0.5, Al: F=1: 0.25, Al: F=1: 0.05 were calcined at 120 °C for 72 h and the ^{27}Al MAS NMR spectra were measured. The tendency observed for the untreated products is confirmed after calcination; in fact the sample with the molar ratio Al: F= 1: 0.25 has shown the highest relative amount of sub-coordinated Al species.

4.4 Thermal Treatment

The products obtained with the lowest amounts of fluorine were treated thermally in order to evaluate the thermal evolution of the 4-fold and the 5-fold coordinated Al sites. For the calcination process, samples were treated in a ceramic crucible and were kept on the furnace for 12h at different temperatures (between 125 °C and 1400 °C). After each calcination treatment, the ^{27}Al NMR spectra of each sample were recorded and normalized to the main signal, corresponding to the 6-fold coordinate Al sites (**Figure 4.6**). ^{19}F MAS NMR spectra were also measured per each temperature of calcination (**Figure 4.7**).

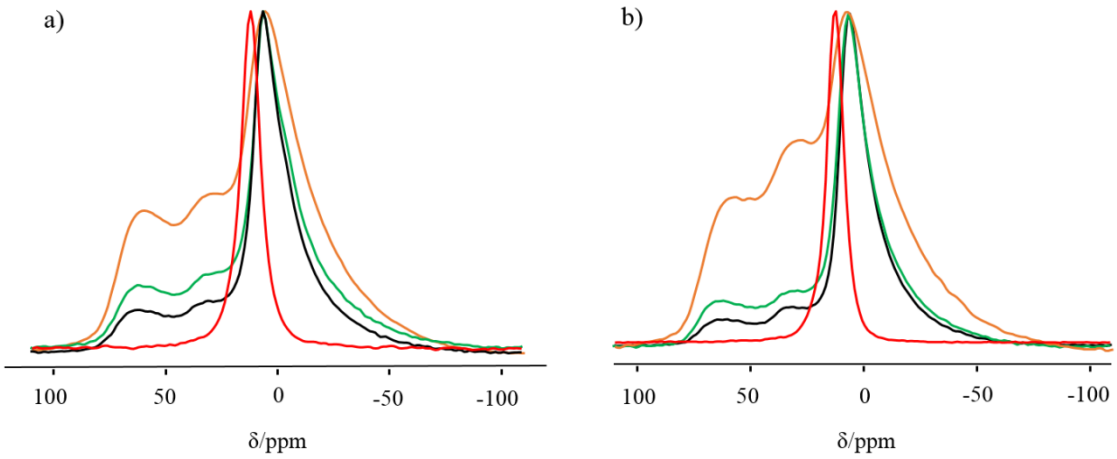

Figure 4.6: Central signals of ^{27}Al MAS NMR spectra of the milled products after thermal treatment at different temperatures. a) Molar ratio Al: F = 1. 0.25; b) Al: F = 1: 0.05. Black line: r.t.; green line: 125 °C; orange line: 500 °C; red line: 1400 °C.

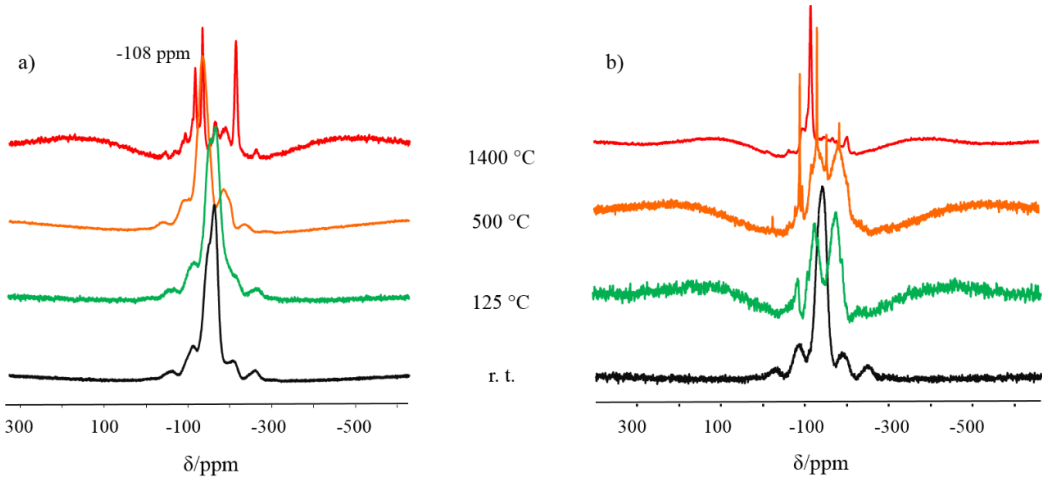

Figure 4.7: Central signals of ^{19}F MAS NMR spectra of the milled products after thermal treatment at different temperatures. a) Molar ratio Al: F = 1. 0.25; b) Al: F = 1: 0.05.

As already shown in the previous paragraph, the aluminium hydroxide fluorides feature, besides the main signal at around 3 ppm, two weaker signals, one around 30-40 ppm (assigned to 4-fold coordinated Al sites) and the other one around 60-70 ppm (assigned to 6-fold coordinated Al sites). Amorphous aluminium hydroxides exhibit these signals too. By increasing the temperature the main signal shifts to the lower field (from 3 to 10-12 ppm) and the ratios of the 6-fold to 4-fold and 5- fold coordinated Al sites change. As mentioned above, this ratio is strongly influenced by the amount of fluorine. The degree of structural disorder is evidenced by the conversion of a big part of 6-fold coordinated species in the sub-coordinated units. Independently on the fluorine content, at a temperature of 1400 °C, only the main signal shifted to the lower field can be depicted. The corresponding ^{19}F NMR spectra (**Figure 4.7**) can suggest some understandings about structural details. For the samples dried at room temperature one main signal at around -140 and -150 ppm is shown. The broadness of the signal is due to the amorphous nature of the sample and maybe to the probable superposition of different species[64]. Therefore it is not easy to assign certainly the species. By increasing the temperature a shift of this main signal to the higher field is observable. For a temperature of 1400 °C only small residues of fluorine corresponding to really small peaks are present.

4.5 TG/DTA Characterization

As expected, the thermal behaviour of samples with different F-degree changes. Fluorides have especially a great influence on the transition temperature to the most thermodynamically stable form of alumina α-Al_2O_3 (corundum). From the DTA curve of the milled γ-$Al(OH)_3$ (**Figure 4.8**, red curve), it can be noticed anyway that the transition temperature (usually at about 1200 °C) is definitely decreased (broad exothermic peak at 957 °C) after milling.

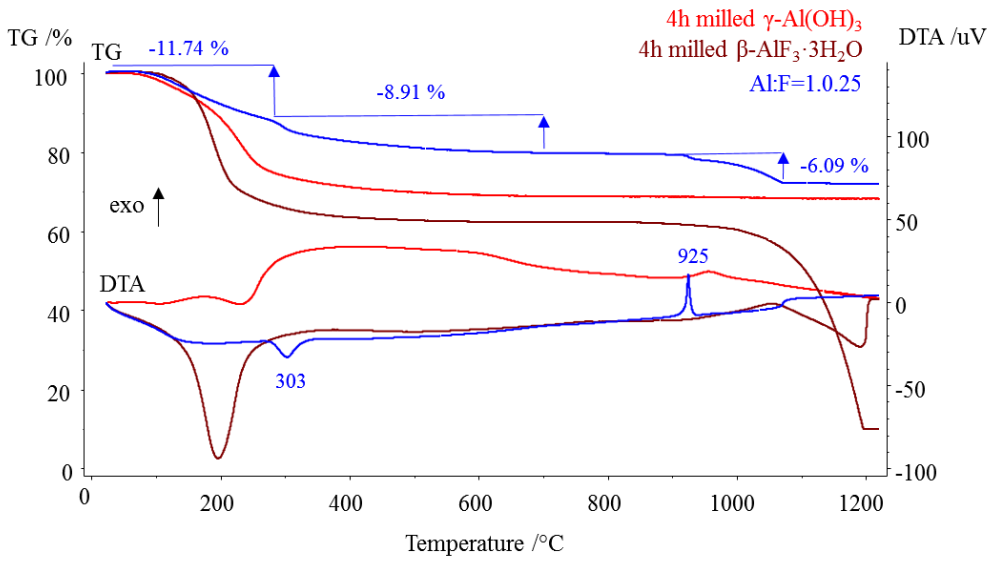

Figure 4.8: DTA and TG curves of the mechanochemical product of the reaction between γ-$Al(OH)_3$ and β-$AlF_3 \cdot 3H_2O$ in a molar ratio Al:F of 1:0.25 milled γ-$Al(OH)_3$, milled β-$AlF_3 \cdot 3H_2O$.

In the low-temperature region (T < 300 °C) the mass loss of 24 % of the milled γ-$Al(OH)_3$, which starts already below 100 °C, corresponds to the loss of water. In the same range of temperature (T < 250 °C) the untreated γ-$Al(OH)_3$ only exhibits a 4% mass loss (TG/DTA curves of unmilled γ-$Al(OH)_3$ (**Figure 3.9**). It means that the release of adsorbed water from the activated disordered surface of milled γ-$Al(OH)_3$ is substantially easier compared to the unmilled sample. In contrast to unmilled γ-$Al(OH)_3$, the TG /DTA curves of milled γ-$Al(OH)_3$ do not show well resolved peaks corresponding to the known steps of the dehydration process (first step: desorption of adsorbed water, second step: condensation of hydroxyl groups) (cf. **Figure 3.9** and [9, 67, 54]). This is finally expected considering the amorphisation of the sample as a consequence of milling. As expected for the thermal behavior of samples implemented in **Figure 4.8**, the highest loss of water (29 % for T < 300 °C) belongs to the milled β-$AlF_3 \cdot 3H_2O$ (**Figure 4.8**, claret curves). All the DTA/TG curves of the products with varying molar ratios are available (**Figure 4.9**).

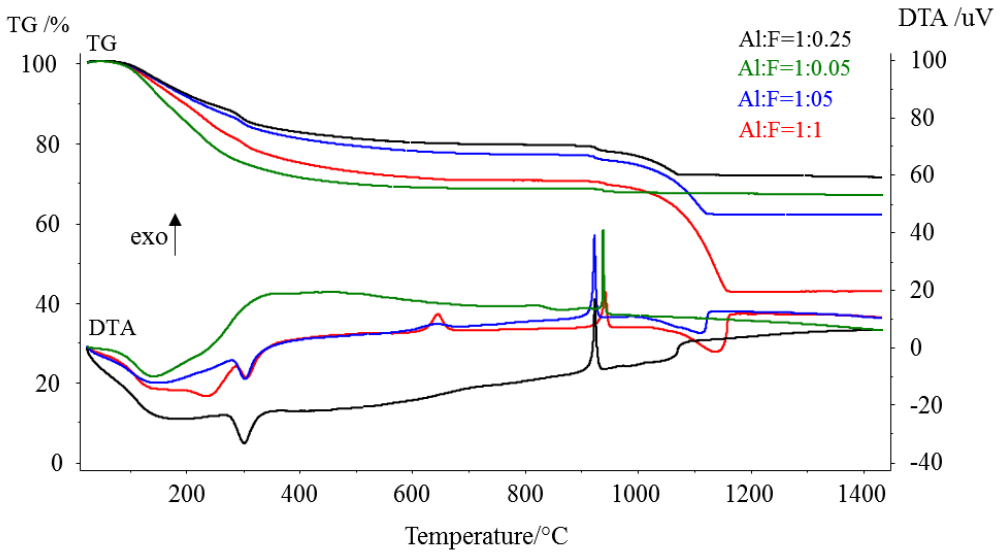

Figure 4.9: TG/DTA curves of the products milled in a molar ratio Al: F of 1:1 (red curves), 1:0.5 (blue curves), 1:0.25 (black curves), 1:0.05 (green curves).

The TG/DTA curve of the product milled in a molar ratio of 1: 0.25 is shown here (**Figure 4.8**, blue curves). For this sample, a surprising narrow exothermal effect observed at 925 °C indicates the phase transition to α-Al_2O_3. Both the X-ray powder diffractogram and the ^{27}Al MAS NMR spectrum taken after DTA/TG measurements (heated up to a temperature of 1200 °C) confirm the formation of nanocrystalline α-Al_2O_3. The ^{27}Al MAS NMR spectrum indicates the existence of AlO_6 octahedra with a chemical shift typical for corundum and the X-ray powder diffractogram shows all typical very narrow reflections of corundum. A substantial mass loss in the high-temperature region (T > 1000 °C) can be detected only in the TG curve of the β-$AlF_3 \cdot 3H_2O$, which is due to the sublimation of AlF_3.

4.6 BET Specific Surface Area Measurement

Since one of the potential applications of these new substances is in heterogeneous catalysis, the measurement of the specific surface area is an indispensable experiment. The specific surface areas of each sample, including the unmilled and milled reactants, are summarized in **Table 4.4**.

Table 4.4: Relative surface areas calculated with the BET method for the reactants and for each product with different molar ratios.

Sample	BET surface area (m^2/g)
β-$AlF_3 \cdot 3H_2O$	5.3
milled β-$AlF_3 \cdot 3H_2O$	2.7
Al : F = 1 : 0.5	31.7
Al : F = 1 : 0.25	94.9
Al : F = 1 : 0.1	43.0
Al : F = 1 : 0.05	51.3
milled γ-$Al(OH)_3$	214.0
γ-$Al(OH)_3$	1.8

Table 4.4 shows that high energy ball milling has a strong impact on the specific surface area of γ-$Al(OH)_3$ compared to the unmilled sample. In fact, after milling we were able to obtain high surface area γ-$Al(OH)_3$. The induced amorphisation of γ-$Al(OH)_3$ (cf. **Figure 4.1**) leads to a distinct increase of the BET surface area, attributed to the changes in the nature of the pore structure. The reduction of the particle size and a partial removal of water defines an increase of the specific surface area. The combination of the high energy ball milling process and the F-doping results in lower specific surface areas compared to the milled γ-$Al(OH)_3$ alone. Even with this characterization method, the product milled with a molar ratio Al: F= 1:0.25 gives the highest specific surface area among the products obtained by milling. The shape of the isotherm suggests the presence of slit-like, easily accessible mesopores, with an estimated average pore diameter of about 12 nm[68].

4.7 Zeta Potential Characterization

The milling process induces a change in the charging behavior of the samples in aqueous solution. The recorded trends of the measured zeta-potential in dependence on the pH-value for the two reactants, before and after milling, are shown in the **Figure**

4.10. The unmilled γ-$Al(OH)_3$ shows a zeta potential (ZP) higher than +30 mV in the pH range 2-4 (**Figure 4.10, a**). By convention, dispersions of oxides (hydroxides) having zeta potentials larger than |30|mV are considered as sufficiently stabilized [69].

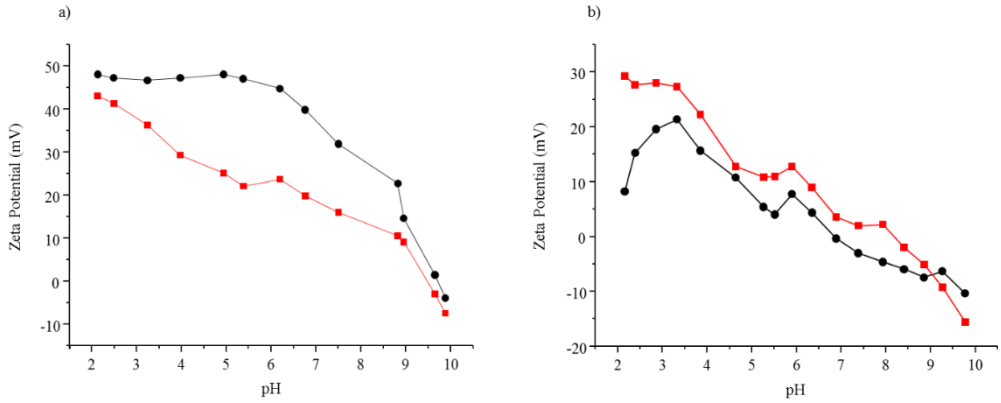

Figure 4.10: Zeta potential vs pH of a) γ-$Al(OH)_3$ and (b) β-$AlF_3 \cdot 3H_2O$. ■ = unmilled samples; ● = milled samples.

These ZP-values of γ-$Al(OH)_3$ are distinctly enlarged after milling, and values above 30 mV can be observed up to a pH-values of about 7, i.e. milling broadens the stability range of the suspensions. A similar trend can be observed for suspensions of unmilled and milled β-$AlF_3 \cdot 3H_2O$, although the ZP values themselves are in both cases distinctly lower than for suspensions of aluminium hydroxides (**Figure 4.10, b**). In both cases a shift of the pH-value of the isoelectric point (pH_{IEP}) with milling suggests that alteration of the reactants surface has taken place during milling. The pH_{IEP} of γ-$Al(OH)_3$ is shifted from 9.48 for the unmilled sample to 9.61 for the milled sample. For β-$AlF_3 \cdot 3H_2O$ this shift is observed from 7.0 (unmilled sample) to 8.5 (milled sample).

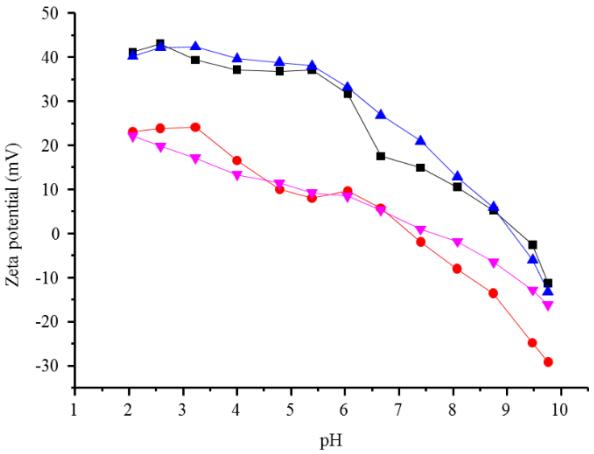

Figure 4.11: Zeta potential vs pH of the milled products obtained with different molar ratios Al: F. ■: 1:0.25; ●: Al: F= 1: 0.5; ▲: Al: F= 1: 1; ▼: Al: F= 1: 1.5.

The F-doping also affects the behavior of the products in aqueous suspension. Whereas samples with low fluorine content have a pH_{IEP} nearby the values of γ-$Al(OH)_3$, an increase of the F amount shifts the pH_{IEP} into a more acidic range (**Figure 4.11**). The latter values are comparable to those of the reference sample with higher fluorine content (**Figure 4.10, b**). With **Figure 4.11** it is obvious that a gap to lower zeta potential values can be especially observed for the milled products which exhibit crystalline pyrochlore structure (by XRD and NMR evidence), and therefore a nominally higher fluorine content.

4.8 ^{1}H-^{2}H CP MAS NMR

In order to get more information about the interaction of the milled samples with water, ^{1}H-^{2}H Cross Polarization MAS (CPMAS) NMR measurements were performed. As already previously shown, the different fluorination degree guaranteed the formation of different products. The molar ratio Al: F= 1: 0.25 was considered as the most effective one for this research. For this reason, the CPMAS NMR experiment was done just for this sample along with a ^{2}H MAS NMR experiment. Five different ^{2}H species can be identified by the combination of these two experiments, as illustrated in **Figure 4.13**.

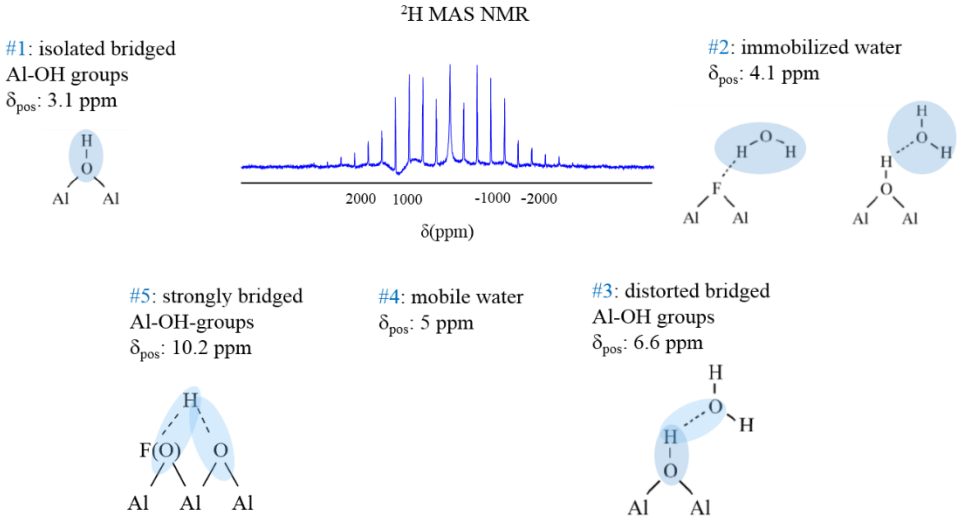

Figure 4.12: ^{2}H MAS NMR and potential assignment of 5 different species.

A signal at a chemical shift of ~ 5 ppm indicates the presence of mobile water at the surface of the sample (species #4, visible only with the direct ^{2}H MAS NMR experiment and disappearing in the CP experiment (**Figure 4.13**). The simulation of the CP

spectrum allowed to discriminate further species: for instance, immobilized water is also present and represented by the signal at a chemical shift of ~4 ppm. Strongly bridged, distorted bridged and isolated bridged Al-OH groups were also characterized. So an exchange of hydrogen and deuterium effectively occurred. How the ^{1}H-^{2}H exchange was realized is item by item explained in the Materials & Methods chapter.

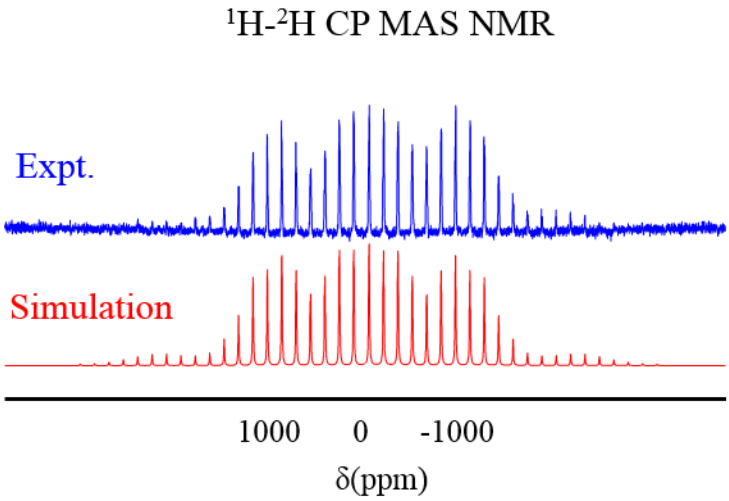

Figure 4.13: ^{1}H-^{2}H Cross Polarization MAS (CP-MAS) NMR. At the top the experimental curve (blue line). At the bottom the simulated one (red line).

4.9 Conclusions

The mechanochemical synthesis of low-fluorine doped aluminium hydroxide fluorides described here is the same applied previously[9], (equ. (1)). As already known, this led to the well crystalline hydroxide fluorides $AlF_x(OH)_{n-x}\cdot nH_2O$, with Al in local 6-fold oxygen/fluorine coordination, when an Al: F ratio of 1: 1.5 was chosen. With decreasing F-supply (Al: F =1:0.5), reflections of the crystalline pyrochlore structure can be still observed, as well as some main reflections of γ-$Al(OH)_3$. That makes the matrix composition very complex to analyze. But already for the two crystalline components two general different local Al-coordinations ($Al(O/F)_6$) and AlO_6 have to be considered (cf. **Table 4.2**). With further decreasing F-content, distinct changes are observable by X-ray measurements. For the product milled with a molar ratio of Al: F = 1: 0.25, the matrix is almost X-ray amorphous but residues of γ-$Al(OH)_3$ (narrow reflection at about 18°) hint at a complex composition. An again lower amount of F introduced by milling leads to totally X-ray amorphous products (Al: F= 1:0.1, Al: F=

1:0.05). Anyway as shown in Figure 2 and Figure 3, a strong local disorder is introduced and not only 6-fold coordinated Al sites can be observed. The maximum amount of 4- and 5- fold coordinated Al sites was achieved for the product milled with a molar ratio Al: F of 1:0.25 (**Figure 4.4**). In any case, the asymmetric upfield decay is mainly caused by distribution effects. A higher F content leads to the formation of the crystalline pyrochlore structure, also noticeable in the decreasing amount of 4- and 5-fold coordinated sites. Thanks to the comparison of the chemical shifts detected and calculated for MAS NMR spectra of fluorine and aluminium depending on the F-content, the F species can be related to Al species of different coordination[9,64]. Decreasing the amount of fluorine, the broadening of the main ^{19}F signals is observed in agreement with the rise of the 4-fold and 5-fold Al coordinated sites (as it can be observed by the ^{27}Al MAS NMR spectra, **Figure 4.3**). As all the maxima of the ^{27}Al MAS NMR signals of the compounds are within the range from 12 to -20 ppm, the main coordination of aluminium is octahedral in a mixed O/F surrounding. The corresponding ^{19}F signals can be found in the region between -135 ppm and -160 ppm (**Figure 4.3**), typical for bridging F-sites in octahedral AlF_xO_{6-x} units with an average composition of $AlF_{1-2}O_{5-4}$[64]. The shift of the maximum of the ^{19}F signal from -150 ppm to around -140 ppm and the strongly down-field shifted additional shoulder indicate that not only $AlFO_5$ units are involved. The CP MAS NMR evidenced the correlation of F with the 5-fold coordinated Al environment as well. Further structural changes have been observed in the FT-IR spectra (**Figure 4.14**). Changes in the intensities of Al-O-, Al-F- and OH-bonds occur, indicating structural changes due to the mechanical impact and the fluorination process. However, a clear assignment is almost impossible due to the highly disordered character of these samples, implementing many different species as shown by MAS NMR experiments. The higher the F content is, the more crystalline is the structure and consequently, the narrower the vibrational bands are. In contrary, the widest vibrational bands were observed for the sample with the Al: F ratio of 1: 0.05.

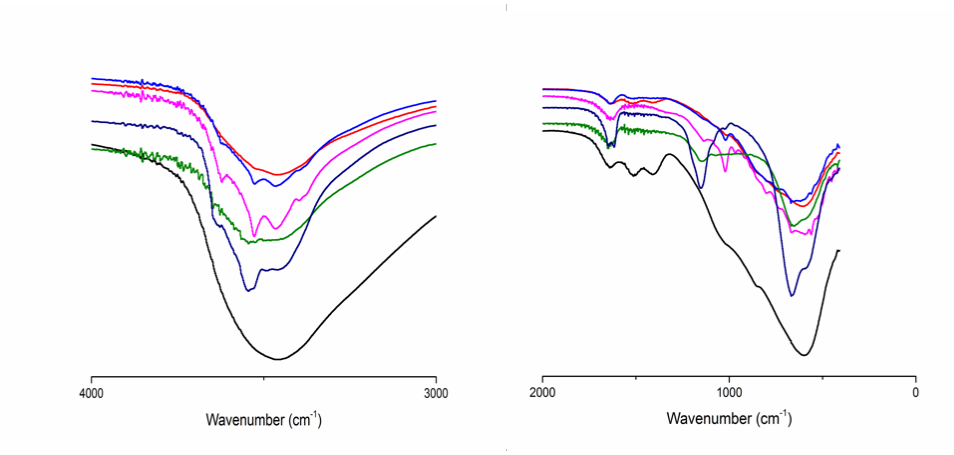

Figure 4.14: FT-IR spectra of the products milled with different molar ratios: Al: F of: 1: 1.5 (dark blue curve), 1: 1 (red curve), 1: 0.5 (blue curve); 1: 0.25 (pink curve), 1: 0.1 (green curve), 1: 0.05 (black curve).

Very low fluorine supply at milling results in highly distorted aluminium hydroxide fluorides containing different structural units. The combination of both processes has a very remarkable effect also on the phase transition behavior to corundum (α-Al_2O_3). High energy ball milling combined with fluoride doping leads indeed to a complete corundum formation after thermal treatment at distinctly lower temperatures, as was shown in the DTA/ TG measurements (Figure 4.9). In the sample milled with the lowest amount of F (Al: F=1: 0.05) we have tested in this work, a really sharp exothermic peak at 939 °C due to the formation of corundum is visible (**Figure 4.9**). A complete transformation to well-crystallized corundum can be observed for all low-fluorine doped aluminium hydroxide fluorides in the temperature range between 925 °C and 939 °C. In the case of milled γ-$Al(OH)_3$, the exothermic peak corresponding to the formation of corundum is definitely broader, indicating a wider temperature range of the phase transition. The lower the F content is, the lower the mass loss in the high-temperature region is. Only for the sample with the highest fluorine content (Al: F= 1: 1) the phase transition to AlF_3 can be observed at about 660 °C (**Figure 4.9**). Milling itself is able to enhance the dehydration due to the strong mechanical impact and due to the activation of the surfaces. It can induce a variety of transformations such as amorphisation, grain boundary disordering but also changes in particle size and surface area. As already evidenced by the BET measurements, the amorphisation of the samples by milling induces higher surface areas. Zeta potential measurements of suspensions of the unmilled and milled samples in water sensitively indicate the number of positive or

negative charges at their surfaces. This number is distinctly higher for samples with very low or no fluorine content. The high number of hydroxyl groups and their accessibility in these samples makes a protonation or deprotonation of the surface in dependence on the pH comparatively easy. As a consequence, remarkably higher values of the zeta potential and isoelectric points in the strong basic region will be found (**Figure 4.10**). All observations described and discussed above will contribute to the enormous potential of these new low-fluorine doped aluminium hydroxide fluorides as catalysts in heterogeneous catalysis. For related compounds prepared mainly by fluorolytic sol-gel techniques, this wide field of applications was already opened [70- 73].

In conclusion, the mechanochemical approach, starting from γ-$Al(OH)_3$ and β-$AlF_3 \cdot 3H_2O$ as reactants, opens a reliable and effective strategy for the formation of aluminium hydroxide fluorides with a very low F-content. Milling has the usual effect of introducing structural defects, causing amorphisation. The impact of milling has been evaluated first on the structure and the surface of the precursors used in this presented mechanochemical synthesis: a crystal size reduction in the case of β-$AlF_3 \cdot 3H_2O$ (represented by a broadening of the reflections in the X-ray powder diffractogram) and an amorphisation of the crystalline γ-$Al(OH)_3$ (confirmed also by the disappearance of the narrow reflections in the X-ray powder diffractogram). The mechanical impact strongly affects the phase transition of γ-$Al(OH)_3$ to corundum. As a consequence of the combined action of milling and fluoride doping the number of introduced defects is remarkably higher compared to a separate milling of the reactants. The introduction of fluorine in different Al: F molar ratios (higher than 1:1) leads to the formation of strongly disordered products. The higher the fluorine degree is, the more crystalline is the structure of the products. In contrast to the crystalline aluminium hydroxide fluoride and to γ-$Al(OH)_3$, the amorphous products exhibit a higher amount of unsaturated Al sites (detected by ^{27}Al MAS NMR). Especially the signal corresponding to 5-fold coordinated Al species gets a noticeable intensity. After removing the physisorbed water by heating at 120 °C, the amount of unsaturated Al sites increases. High energy ball milling combined with fluoride doping leads in all cases to a complete formation of α-Al_2O_3 after subsequent thermal treatment at around 940 °C. The impact of the mechanochemical process affects also the surface properties of the products. Changes of the specific surface areas and the isoelectric points can be observed.

Chapter 5. On the Influence of Water on the Preparation of Low F-Doped Aluminium Hydroxide Fluorides by Milling

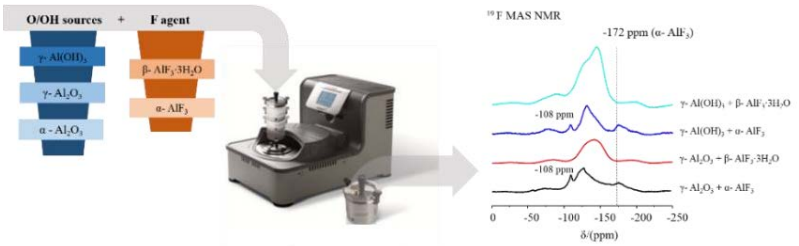

V. Scalise, G. Scholz, E. Kemnitz, *J. Mater. Sci.*, (2018), accepted.

On the main focus:

- How does the structure of the product change, changing the amount of water involved in the synthesis?
- Does water play a crucial role?
- Different products for different reactants.

The significant role played by water in the mechanochemical synthesis of highly distorted aluminium hydroxide fluorides is on the main focus of this chapter and of the whole Ph.D. work. The importance of water in the synthesis was evaluated considering separately combinations of O/OH sources ($Al(OH)_3$, Al_2O_3) and fluorine sources with or without structural water (β-$AlF_3 \cdot 3H_2O$, α-AlF_3). Each system was studied by typical bulk and surface characterization techniques (XRD, MAS NMR, DTA/TG, NH_3-TPD) and compared to each other in order to gain a more comprehensive insight of the importance of including water in the synthesis of amorphous aluminium hydroxide fluorides.

5.1 Introduction

It was previously shown by our group [74] and already mentioned in the previous chapter, that the mechanochemical approach opens a reliable and effective strategy for the formation of amorphous aluminium hydroxide fluorides with a very low F-content. The synthesis was carried out using γ-$Al(OH)_3$ (gibbsite) as starting material and the chosen fluorinating agent was β-$AlF_3 \cdot 3H_2O$. In that case, water was supplied by both reactants (OH groups and water molecules of crystallization).

The main goal of the research shown in this chapter is to evaluate the impact of water included in the structure of different reactants on the product formation. Does water influence the formation of amorphous Al hydroxide fluorides, and if so, how? Is there a

detectable influence on fluoride doping? To give an answer to these questions, two different kinds of aluminium fluorides (hydrated and non-hydrated samples: β-$AlF_3 \cdot 3H_2O$ and α-AlF_3) were used as fluorinating agents. With regard to the effect on both structural and surface properties, also different kinds of aluminium (hydr-) oxide precursors were considered, namely: $Al(OH)_3$ and Al_2O_3. The synthesis was always done just considering two different reactants (**Scheme 5.1**): a fluorinating agent and an Al-(hydr) oxide to ensure the presence of only Al, F, O and H as elements in the reactants and therewith to avoid the introduction of additional impurities.

Changes of the precursors and the product formation, in order to answer the above questions, were followed by X-ray powder diffraction, ^{27}Al and ^{19}F MAS NMR, TPD and DTA/TG techniques.

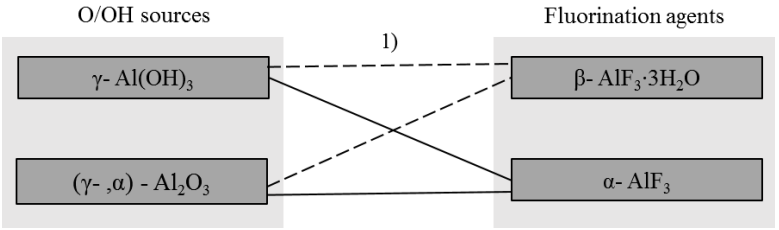

Scheme 5.1: Scheme of the investigated reactions between commercially available Al-(hydr) oxides and Al-fluorides performed in the present study. Dotted line: reactions between Al (hydr-) oxides and a fluorine source including water in the structure. Full line: reactions between Al (hydr-) oxides and water-free fluorination agent. 1) Previous reaction, explained in detail in the 4th Chapter and published [74].

5.2 XRD Characterization

Many crystalline materials, including γ-$Al(OH)_3$ (gibbsite), are known to lose their long-range order and become X-ray amorphous at milling. For instance, the impact of milling is strong enough to disrupt the typical layer structure of γ-$Al(OH)_3$ during amorphisation [3, 4, 13, 21]. The X-ray powder diffractogram of γ-$Al(OH)_3$ after 4h milling is added to **Figure 5.1** for comparison. A strong broadening of all reflections can be observed. Once we introduce fluorine by milling, the X-ray patterns of the products show no new reflections (**Figure 5.1**), which can be related to the fluorine introduction, independent of using β-$AlF_3 \cdot 3H_2O$ or α-AlF_3 as fluorinating agents. Only two distinctly visible narrow reflections (18.5° and 20.50°) characterize the diffractogram of the reaction between γ-$Al(OH)_3$ and β-$AlF_3 \cdot 3H_2O$, which belong to the γ-$Al(OH)_3$ structure.

Whereas no typical reflections of the γ-$Al(OH)_3$ structure are anymore detectable in the diffractogram of the reaction between γ-$Al(OH)_3$ and α-AlF_3. Here, the product is almost X-ray amorphous and no further considerations can be made.

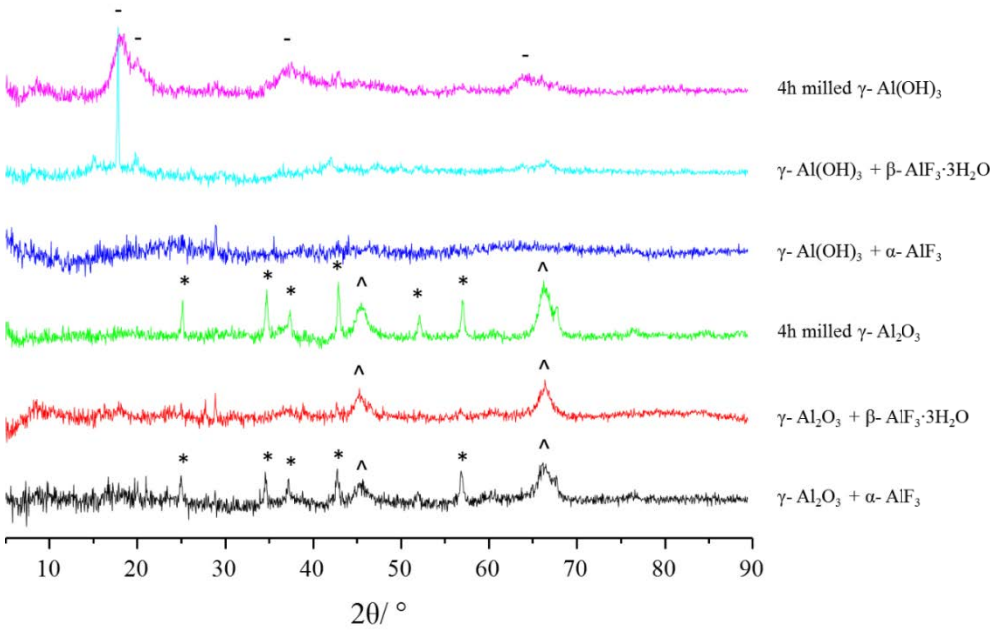

Figure 5.1: X-ray powder diffractograms of samples prepared by reaction of an OH/O source and an F source as indicated on the right side of the graph. *: X-ray reflections of α-Al_2O_3 (PDF number: 10-173); ^: X-ray reflections of γ-Al_2O_3 (PDF number: 10-425). -: X-ray reflections of γ-$Al(OH)_3$ (PDF number: 33-18). Al: F= 1: 0.25.

In agreement with our previous study, the formation of $AlF_x(OH)_{3-x}\cdot nH_2O$ samples in pyrochlore structure can be ruled out with this low fluorine supply.

In case that γ-Al_2O_3 is considered as starting material, milling time has an important influence on the structure of the obtained products. For a milling time shorter than 1h, just a broadening of the X-ray reflections of γ-Al_2O_3 is observable [75]. After a 4h milling treatment, reflections of the X-ray diffractogram evidence that the transition to the α-phase begins to occur (diffractogram added to **Figure 5.1** for comparison). The introduction of fluorine by milling with γ-Al_2O_3 changes the dynamics of the phase transition from γ-Al_2O_3 to α-Al_2O_3. If less water is involved in the mechanochemical reaction (in our case this means to consider α-AlF_3 as fluorinating agent), the phase transition to α-Al_2O_3 can be observed. In contrast, an almost X-ray amorphous product is obtained by milling γ-Al_2O_3 with β-$AlF_3\cdot3H_2O$. In case that α -Al_2O_3 is the examined

O/OH source, due to its well-packed structure, just a decrease of the intensity and a broadening of the reflections is outlined (**Figure 5.2**).

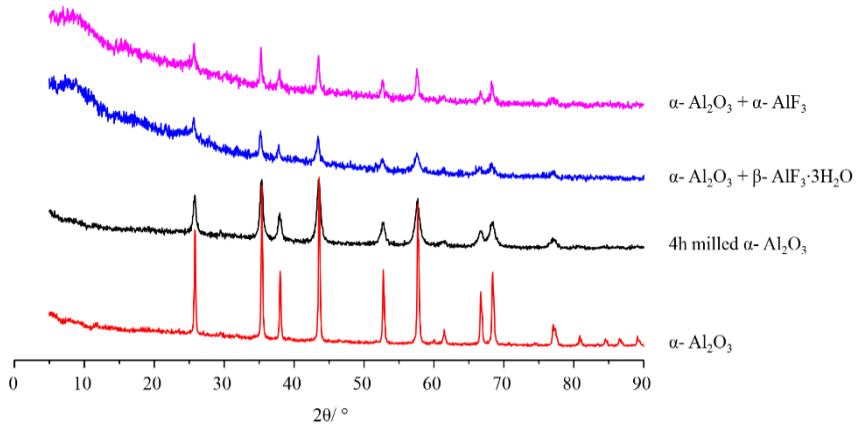

Figure 5.2: X-ray powder diffractograms of samples prepared by reaction of α-Al_2O_3 and an F source as indicated on the right side of the graph.

5.3 ^{27}Al and ^{19}F MAS NMR Characterization

Figure 5.3 shows a comparison of the ^{27}Al MAS NMR spectra (central lines) and ^{19}F MAS NMR spectra of the prepared samples in this paper. From the bottom to the top, the amount of water involved in the mechanochemical reaction trough the reactants increases. The considered molar ratio Al: F was taken as 1: 0.25 for all reactions. Depending on the composition of the starting materials, different fluorine and aluminium environments are observed.

The ^{27}Al MAS NMR spectra do not exhibit drastic changes due to the fluorine doping (spectra of milled γ-Al_2O_3 and milled γ-$Al(OH)_3$ added to **Figure 5.3** for comparison). The strongest effect on the structure of the aluminium (hydr-) oxides seems to be actually due to the mechanochemical treatment.

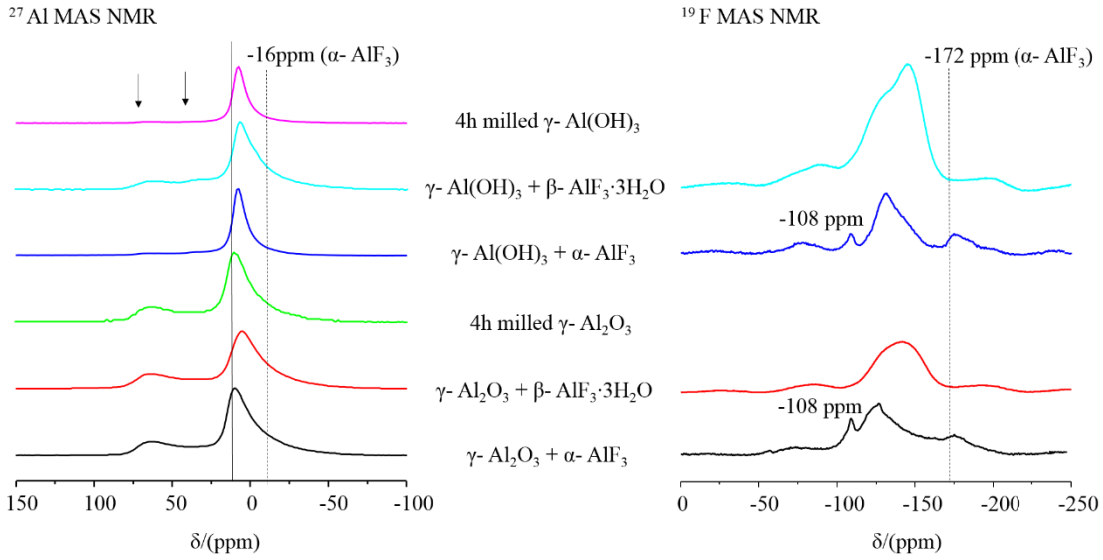

Figure 5.3: ^{27}Al MAS NMR and ^{19}F MAS NMR spectra (central line, ν_{rot}= 20 kHz) of each mechanochemical product obtained by the reaction of the two reactants indicated in the middle. The black full line indicates the position of the signal assigned to AlX_6. Black arrows remark the position of the raising up signals corresponding to the sub-coordinated Al species.

Indeed, the two weak signals, appearing in the characteristic range for sub-coordinated Al species, rise up already after milling γ-$Al(OH)_3$ [44, 45, 74].

These signals are observed in amorphous aluminium hydroxides as well [66]. Once fluorine is introduced by the milling, the positions of these signals (at 30-40 ppm and at 60-70 ppm) do not experience any significant changes. But they are most distinctly visible after the reaction of $Al(OH)_3$ with β-$AlF_3·3H_2O$ (**Figure 5.3**). Considering the product achieved by the reaction of an aluminium (hydr-) oxide with α-AlF_3, residues of α-AlF_3 still can be assigned in the ^{27}Al MAS NMR spectra. In fact, the ^{27}Al MAS NMR spectra cover a signal at about -16 ppm corresponding to α-AlF_3 which is in that case responsible for the broader asymmetric decay to higher field [76]. A line is introduced in **Figure 5.3** at the position of -16 ppm as a guide for the eyes. The same products are characterized by ^{19}F MAS NMR in which now different F-species can be discriminated. Products obtained after milling reactions with α-AlF_3 still show in their ^{19}F MAS NMR spectra the contribution of the fluorine signal belonging to α-AlF_3 with the typical isotropic chemical shift at -172 ppm (as also marked in **Figure 5.3**). Instead, residues of α-AlF_3 cannot be observed in the X-ray powder diffractograms of the products (**Figure 5.1**), which can be a consequence of the too low fluorine supply. In two ^{19}F spectra, a new signal at -108 ppm rises up. The same signal was observed after annealing an

amorphous Al hydroxide fluoride (starting materials: γ-$Al(OH)_3$ and β-$AlF_3 \cdot 3H_2O$) at 1400 °C, a temperature at which the transition to corundum is surely completed (**Figure 5.4**).

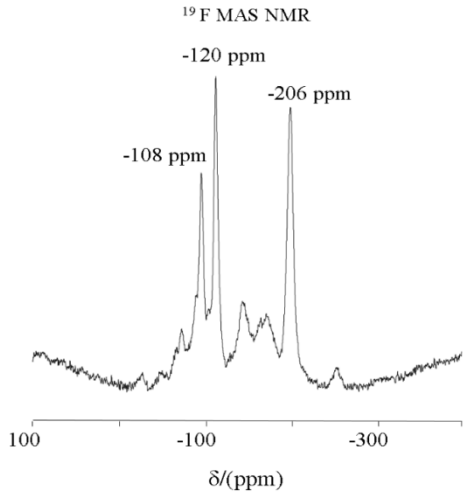

Figure 5.4: ^{19}F MAS NMR spectrum of F-doped α-Al_2O_3, obtained after a DTA/TG measurement up to 1200 °C. The DTA curve shows the complete transition to α- phase. (Starting material: amorphous $AlF_x(OH)_{3-x}$, prepared by milling γ-$Al(OH)_3$ with β-$AlF_3 \cdot 3H_2O$). Al: F =1: 0.25.

This chemical shift was recently assigned to 3-fold Al-coordinated F^- ions on the surface of corundum by DFT calculation [77].

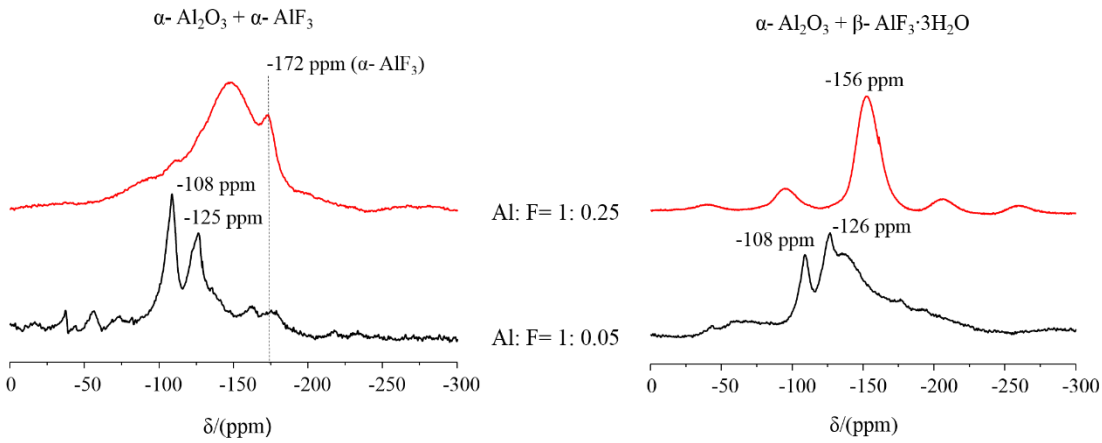

Figure 5.5: ^{19}F MAS NMR spectra (ν_{rot}= 20 kHz) of the products obtained by the reaction of the α-Al_2O_3 with the two fluorine sources indicated on top. The amount of fluorine considered in the reaction increases from the spectrum at the bottom to the one at the top.

To prove this new situation of fluorine coordination, corundum was milled in addition to the two fluorinating agents used in this study. For an Al: F molar ratio of 1: 0.05 and independent from the fluorinating agent (whether it is α-AlF_3 or β-$AlF_3 \cdot 3H_2O$), the same

signal was observed also in the case that one of the reactants is α-Al_2O_3, as shown in **Figure 5.5**. The comparison of different molar ratios highlights how the amount of F present in the reactants plays a crucial role in the formation of the products. If the really low amount of fluorine (Al: F= 1: 0.05) is considered in the reaction, the ^{19}F MAS NMR spectra are characterized by narrower signals which can be expected. The signal at δ_{19F}= -108 ppm (already discussed above) arises independently on the fluorine source. But from Fig.3 the importance of the choice of the fluorination agent can be easily noticed. Using α-AlF_3, fluorine signals belonging to this reactant are still present as residues besides the typical signals for F-doped corundum. The latter are enveloped with the higher fluorine supply (**Figure 5.5**) with a signal at about -145 ppm, standing for bridged F-sites in local AlF_xO_{6-x}-units.

In the case that β-$AlF_3 \cdot 3H_2O$ is used as a fluorinating agent, the ^{19}F MAS NMR spectra are characterized by really broad signals within a region of δ_{19F} = -120 ppm and δ_{19F} = -152 ppm (**Figure 5.3**, **Figure 5.5**). Especially the higher-field region (**Figure 5.3**) corresponds to a typical region for bridging F-sites in octahedral AlF_xO_{6-x} units [64]. For a molar ratio of Al: F= 1: 0.05 two specific narrower peaks, beside the one at -108 ppm, are evident which are covered when a higher F-content is supplied (**Figure 5.3**).

5.4 TG/DTA Characterization

The different amount of water considered in the reaction plays a crucial role especially in the thermal behavior of the products. **Figure 5.6** shows the results of the thermal analyses of some of the studied samples. The behavior of the product obtained by the reaction of γ-$Al(OH)_3$ and β-$AlF_3 \cdot 3H_2O$ was already detailed analyzed previously [74]. Thermogravimetric curves with the indicated percentage of mass loss are shown in the supporting information (**Figure 5.7**). In case that one of the reactants in the mechanochemical synthesis is γ-$Al(OH)_3$, endothermic peaks below 300 °C can be expected [44, 78, 79]. This is due to the fact that not all the water is released. Considering the curves corresponding to the reaction between γ-$Al(OH)_3$ and α-AlF_3, the total mass loss of 31.4 % for a temperature lower than 300 °C actually agrees well with the theoretical value of 34.6 % for the dehydration and dehydroxylation reaction of γ-$Al(OH)_3$ [44]. Although a similar mass loss was expected in the same range when β-$AlF_3 \cdot 3H_2O$ is used as fluorination agent, the endothermic peak is definitely narrower and smaller.

This is maybe due to the fact that most of the water releases for this reaction already during the milling process. Really narrow exothermic peaks in the range between 936 °C and 967 °C stay for the phase transition to α-Al_2O_3. As already known from the literature [9, 74, 80], the addition of fluoride reduces the phase transition temperature to corundum. When γ-Al_2O_3 is involved in the mechanochemical reaction then the trend of the DTA/TG curves is really similar to the one recorded for the separately milled γ-Al_2O_3 [45]. The most significant change is the lower temperature of the phase transition to corundum (from ~ 1100 °C to ~ 984 °C). And it is well known that the formation of the α–Al_2O_3 phase takes place without a significant mass change, as also happened in our case (**Figure 5.7**). The presence of α-AlF_3, this phase transition temperature decreases to 936 °C. In the case that α-Al_2O_3 is one reactant no exothermic peaks are present in this temperature range. The broader exothermic peak present in the curve obtained from the reaction between α-Al_2O_3 and α-AlF_3 (at 677 °C) can be due to the beginning formation of crystalline α-AlF_3 from nano-α-AlF_3. The latter can be expected to be formed at milling.

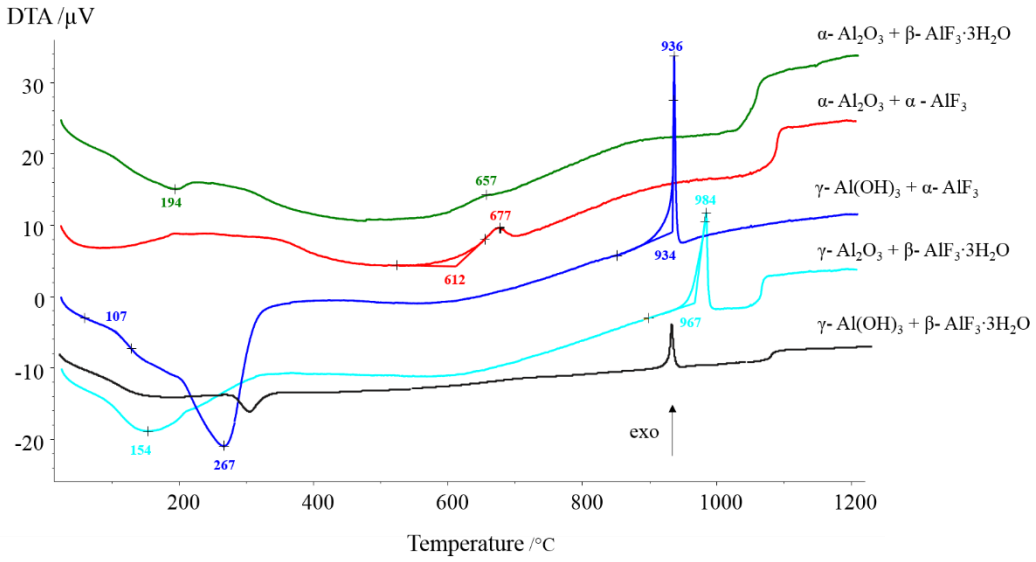

Figure 5.6: DTA curves of some of the studied products obtained by milling. Reactants are indicated on the right side of each curve. The direction of exothermic reaction is indicated in the left side of the graph.

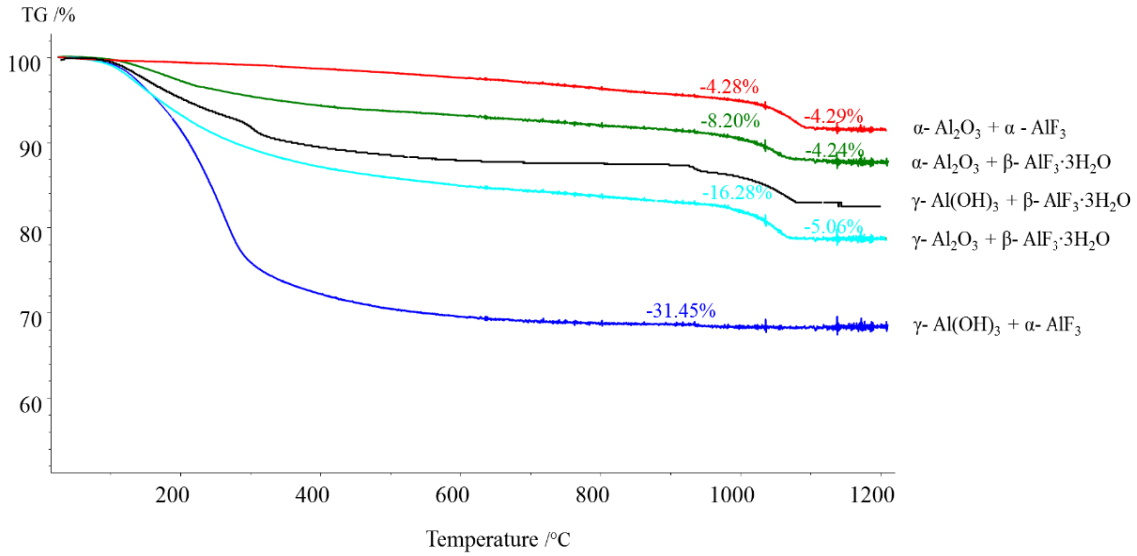

Figure 5.7: TG curves of some of the products. The mass loss (in %) is indicated for each curve.

5.5 NH_3-TPD Characterization

Figure 5.8 gives an overview about the presence and strength of acid sites of the different products obtained by milling. The data represent the integral acidity of both Brønsted and Lewis acid sites. All curves, except using the water-free reactants, show a main peak at about 270 °C. In case that β-$AlF_3 \cdot 3H_2O$ is the fluorination agent, a second less intense and broad shoulder can be depicted.

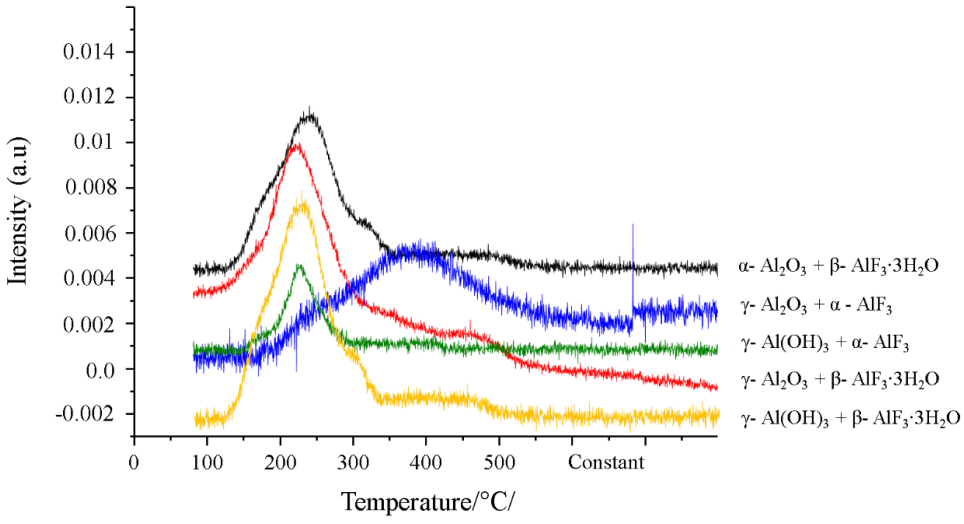

Figure 5. 8: NH_3-TPD desorption profiles of different products. Reactants are indicated on the right side of each curve. The relative amount of desorbed NH_3 is on the y-axis.

5.6 Classical Solid State Chemical Reaction vs Mechanochemistry

Does the fluorination occur just by applying the classical solid state chemical reaction? Can we get the same product? In order to show the power of mechanochemistry, one of the previous syntheses was carried out also at a temperature of 500 °C for 2h. The synthesis involved α-Al_2O_3 and β-$AlF_3 \cdot 3H_2O$ as reactants. A comparison of the X-ray diffractograms (**Figure 5.9**, after milling, red line, and after thermal treatment, black line) and of the ^{27}Al MAS NMR spectra (**Figure 5.10**) are here shown. The X-ray diffractograms show a decrease of the intensities of the peaks in both the proceeding ways. The intensities were subjected to a different degree of decrease depending on the used method for the synthesis. The ^{27}Al MAS NMR spectra explicate better the difference between the two procedures. In case milling is used (**Figure 5.10**, red line), just an asymmetric decay to the higher field can be observed due to the presence of residues of β-$AlF_3 \cdot 3H_2O$. But if the classical solid state reaction pattern is used, then ^{27}Al NMR spectrum is definitely different. The access of air in the Q-crucible defines the beginning of a partial hydrolysis process with the formation α-AlF_3 (-17 ppm). The resonance at around 60 ppm corresponding to the presence of 4-fold coordinated Al sites indicates the partial formation γ-Al_2O_3.

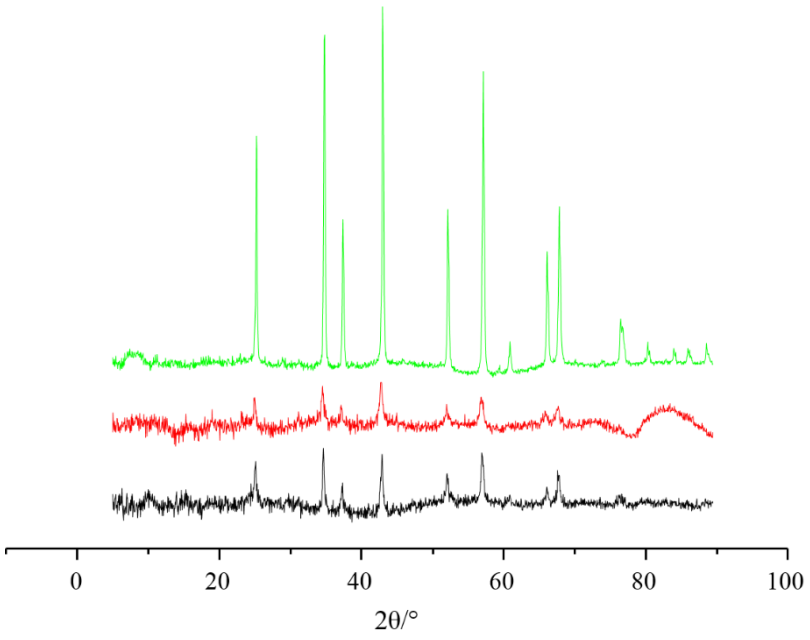

Figure 5.9: X-ray diffractograms of the classical solid state reaction (black line) and mechanochemical reaction (red line). The diffractogram of untreated α-Al_2O_3 (top, green line) is added for comparison.

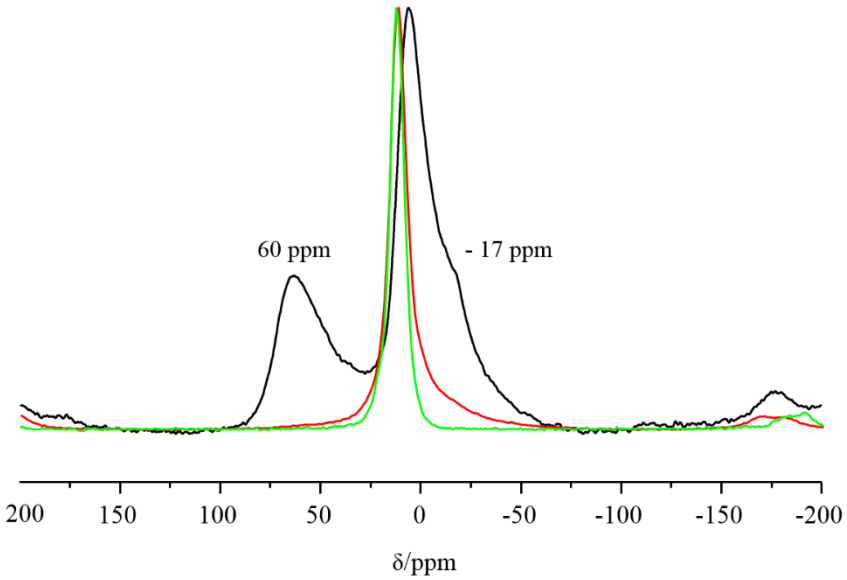

Figure 5.10: ^{27}Al MAS NMR spectra of the classical solid state reaction (black line) and mechanochemical reaction (red line). The spectrum ^{27}Al MAS NMR of untreated α-Al_2O_3 (green line) is added for comparison.

5.7 NH_4F as Fluorination Agent

Some mechanochemical tests on the structure of γ-Al_2O_3 fluorinated by NH_4F were also done in this Ph.D. project. No significant changes were observed in the structure of the products compared to one of the reactant. The impact of the fluorination by α-AlF_3 and β-$AlF_3 \cdot 3H_2O$ is more evident and effective. Using these reactants, the presence of side products can be observed. **Figure 5.11** shows the X-ray diffractograms of the products of the mechanochemical synthesis of γ-Al_2O_3 and NH_4F. Reflections of Ammonium hexafluoroaluminate are present independently on the fluorination degree. Evidence of the presence of side products is also recorded in the ^{19}F MAS NMR spectra. Detailed characterizations and considerations and about this synthesis process can be found in the bachelor thesis of Victoria Wenshan Bünger [81].

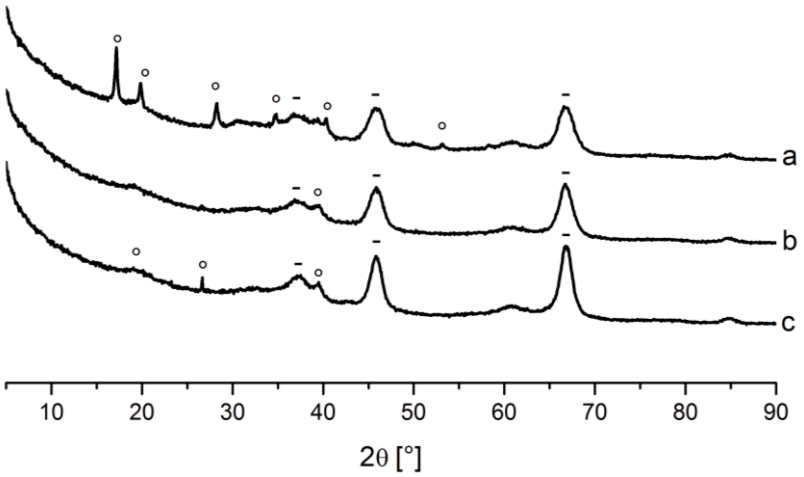

Figure 5.11: XRD of the products obtained by mechanochemical synthesis of γ-Al_2O_3 and NH_4F in a molar ratio Al: F of 1:0.5 (a), 1:0.25 (b), 1:0.1 (c). – Reflections of γ-Al_2O_3 (PDF 10–425); ° Reflections of $(NH_4)_3$ [AlF_6] (PDF 22–1036).

5.8 Conclusions

As already demonstrated in the literature[74], highly distorted aluminium hydroxide fluorides can be simply synthesized by a mechanochemical approach. This solvent-free synthesis does not only allow to introduce a high number of defects in the structures of the starting materials but also changes their structures dependent on the starting material and the water supply. The fluoride doping contributes to an increased degree of amorphisation. Simply by milling the long-range order of the Al hydroxides is lost because of the mechanical action and they become almost X-ray amorphous. In case of corundum (α-Al_2O_3), the intensity of the X-ray reflections decreases and peaks get broader (**Figure 5.2**). Except for the α-Al_2O_3 case and the visible partial formation of α-Al_2O_3 starting from γ-Al_2O_3 (**Figure 5.1**), the high degree of amorphisation makes the interpretation of X-ray diffractograms of the obtained products impossible or at least difficult.

The most relevant information about the structure of the products can be gained with the help of solid state NMR spectroscopy. Although the ^{27}Al MAS NMR spectra do not exhibit significant changes after fluorine doping by milling, the ^{19}F MAS NMR spectra interestingly and selectively confirm the presence of different fluorine species in the samples. The presence of a fluorination agent which includes structural water (β-$AlF_3 \cdot 3H_2O$) results in really broad signals between -120 and -170 ppm in the ^{19}F MAS

NMR spectra of the products, covering a superposition of different F-species and reflect the highly disordered nature of the samples. The maxima of those spectra are at around -152 ppm and can be assigned, as already stated, to bridging F-sites in octahedral AlF_xO_{6-x} species [9]. That fits considering that the ^{27}Al MAS NMR spectra are predominantly characterized by a signal assigned to 6-fold coordinated Al sites. When α-AlF_3 is the fluorination agent of Al (hydr-) oxides, ^{19}F MAS NMR spectra show narrower and more distinguishable peaks. Residues of the α-AlF_3, although not visible in the X-ray powder patterns, are evident thanks to the signal at -172 ppm. The shift of the main peak to lower field in case α-AlF_3 and γ-Al_2O_3 are used as reactants is due to the beginning formation of α-Al_2O_3. That causes also a shift of the ^{27}Al signal of the AlO_6-units to lower field in its ^{27}Al MAS NMR spectrum (**Figure 5.3**). The group of ^{19}F signals is in a region that can still be generally assigned to bridging fluorine sites. A separate discussion deserves the signal at -108 ppm. As already mentioned in the previous paragraph, this chemical shift was recently assigned to 3-fold aluminium coordinated F^- ions in corundum (**Figure 5.4**). In our samples (**Figure 5.2**) it gives a sensitive indication of the local corundum formation. In case of the combination of γ-Al_2O_3 and α-AlF_3, this is confirmed even by the X-ray powder diffractogram. In case of γ-$Al(OH)_3$ and α-AlF_3, these local units are still not crystalline. The importance of the fluorine degree included in the mechanochemical process can be easily noticed in Fig.3. A very low amount of fluorine (Al: F= 1: 0.05) allows observing well-separated fluoride sites representing defects introduced by milling. Besides the [FAl_3] coordination, typical for α-Al_2O_3: F, a ^{19}F signal at -125 ppm stays for F-coordinated coordinatively unsaturated aluminium sites probably on the surface, not visible in ^{27}Al MAS NMR. With increasing amount of fluorine, the homogeneity of the distribution of the fluoride ions in the structure or at the surface of the Al (hydr-) oxides increases. Unfortunately, by using the MAS NMR spectroscopy technique, we are not able to distinguish between bulk and surface of the oxides and hydroxides.

Further considerations about the thermal behavior of the products can allow a more comprehensive view of the role played by water. In fact, in contrast to expectation, the highest mass loss (**Figure 5.7**) is given by the product obtained by the reaction between γ-$Al(OH)_3$ and α-AlF_3. The most significant effect on the thermal behavior of the products is due to the disruptive force of the milling process. In accordance with that, a large amount of water already evolved directly at milling using β-$AlF_3 \cdot 3H_2O$ as a

fluorinating agent. In addition, fluorine doping causes in all reactions investigated here a decrease of the phase transition temperature to corundum.

In our previous study (4th Chapter) we showed that a mechanochemical synthesis using $Al(OH)_3$ and β-$AlF_3 \cdot 3H_2O$ as reactants opens a reliable and effective strategy for the synthesis of aluminium hydroxide fluorides with very low fluorine content. With the present study, we varied systematically the water content of the reactants and tried to elucidate the role of water in the mechanochemical synthesis of low fluorine doped aluminium (hydr-) oxides. First, it has to be considered that the water was introduced in the synthesis just as the structural water of the reactants. No other solvents were included in the synthesis. In this specific case, evidently, water improves the fluorination of the Al (hydr-) oxides. This means, a more homogenous distribution of the fluorine species in the structure and at the surface of the aluminium (hydr-) oxides is obtained by mechanochemistry. Considering first as starting material an Al hydroxide (γ-$Al(OH)_3$), the choice of the fluorination agent influences the degree of amorphisation of the final product. In fact, if water is structurally included in the fluorine source (as in the case of β-$AlF_3 \cdot 3H_2O$), residues of γ-$Al(OH)_3$ are still observable and a variation in the ratio between 4-fold coordinated Al and 6-fold coordinated Al sites is evident. In case that no water is present in the structure of the chosen fluorination agent, residues of α-AlF_3 can be detected in the product along with a local indication of corundum formation. In case of γ-Al_2O_3 as one reactant, the use of aluminium fluoride hydrate suppresses the corundum formation at milling. The opposite is true (formation of corundum) using a water-free aluminium fluoride as a fluorinating agent. The presence of water obviously favors the implementation of fluorine and guarantees an almost homogeneous distribution of F-sites in the products.

Chapter 6. Identification of F-Species after Adsorption at the Surface Of Milled and Unmilled γ-Alumina

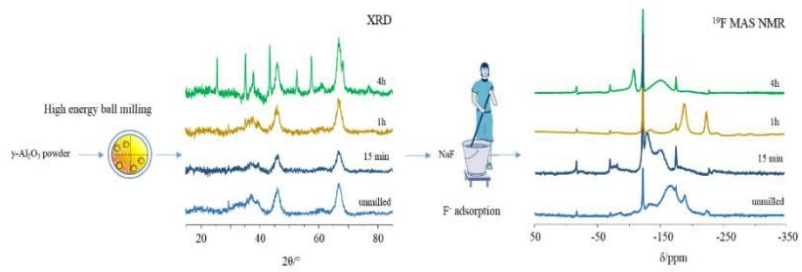

V. Scalise, G. Scholz, R. Bertram, E. Kemnitz, *Surfaces and Interfaces,* 10, 2018, 117-122.

On the main focus:

- Degree of amorphisation of γ-Al_2O_3 strongly dependent on the milling time
- Adsorption of fluorine also strongly dependent on the milling time
- Interpretation of the adsorbed species at the surface of unmilled and milled γ-Al_2O_3

6.1 Fluorine in Water

Fluorine ranks on the 13th position in terrestrial abundance and is the most electronegative of all the chemical elements. It can be found in the form of fluoride ions in natural waters[82] due to its high reactivity. Together with nitrate, fluoride is classified as a contaminant of the water for human consumption. According to the World Health Organization (WHO), the optimal concentration of fluoride in water is recommended to be within the range 0.5-1.5 mg/L (depending on the climate conditions)[83]. Fluoride concentration up to a level of 1 mg/L in groundwater is beneficial to humans but excessive exposure might cause dental as well as skeletal fluorosis. As shown in **Figure 6.1**, its concentration was found to be higher than this limit in various countries of the Rift Valley as in India, China, Kenya, Tanzania, Argentina, and Australia[84].

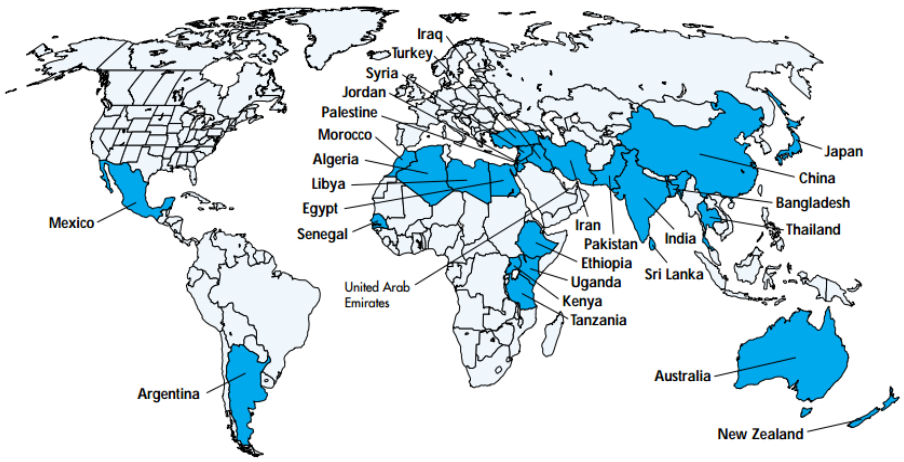

Figure 6.1: A world map for better visualizing the countries in which groundwater is affected by a high degree of fluorine.

Several methods (precipitation[85] and coagulation[86], adsorption, ion exchange[87, 88], electro-dialysis[89], reverse osmosis) have been developed with the aim of reducing the fluoride below the permissible value (<1.5 mg/L). Among these various treatment technologies, adsorption offers a greater accessibility and is often recommended as a low-cost method. Many reviews have reported a list of the most efficient adsorbents tested in the literature under different conditions (pH, temperature, initial fluoride concentration, stability of the adsorbent)[90, 84]. Among the adsorbents, activated alumina (manufactured from Al hydroxides by dehydroxylation) has been studied for many years[91, 92]. The WHO (World Health Organization) and US EPA (US Environmental Protection Agency) classified alumina adsorption as one of the best demonstrated available technology[93]. $Al(OH)_3$ and γ-Al_2O_3 were also widely used for this kind of applications[94]. Maximum uptake is obtained in the pH range 5-8, depending on the characteristics of the Al (hydr-) oxides. At lower pH, the preferential formation of complexes decreases the adsorptive capacity. It was shown that it is the less crystalline compound that is the most rapid and effective adsorbent for fluorine. Indeed the specific surface area or the pore size distributions are, with morphology, some of the parameters that condition reactivity, electrochemical and catalytic activities, and the adsorption properties of the materials. This means that, among the Al oxide phases, γ-Al_2O_3 is the most favored one[95]. The usefulness of this oxide can be traced to a favorable combination of its textural properties, such as the specific surface area, pore volume, and pore size distribution and to its acid/base characteristics. Porous materials possess nanopores or surface-active sites which could act as determinants in adsorption

processes. The impact of milling on the structural, morphological and compositional changes of γ-Al_2O_3 was already the aim of many studies in literature in the last years[45,96]. Indeed high energy ball milling induces a variety of transformations and reactions in oxides such as disordering and amorphisation, introducing defects and crystallographic shear planes[29]. The phases formed by grinding (as in the case of γ-Al_2O_3) may display several other attractive properties, such as improved catalytic properties, as grinding induces the formation of metastable phases and/or of superficial defects which may influence these properties.

But how does the fluorine adsorption occur? Theoretically the adsorption of fluoride onto solid particles proceeds in three steps[97]: 1) transport of F^- ions to the external surface of the particles from the bulk solution; 2) adsorption of F^- ions on the particle surfaces and 3) probable exchange of the adsorbed F^--ions with the structural anions inside adsorbent particles. Recent investigations on the formation of bifluoride species at the fluorinated aluminium hydroxide/water interface were reported by Shimizu et al.[98]. Indeed, ^{19}F MAS NMR studies showed that the observed fluoride species is comparable to the ^{19}F- signal of a sodium-bifluoride ($NaHF_2$) reference. So far, the chemical nature of F^- containing species at the surface of γ-Al_2O_3 was not described in the literature. Therefore the main focus of this chapter is to try to identify and assign adsorbed F^- species and formed structural units at the surface of unmilled and milled y-Al_2O_3. A detailed study of the MAS NMR spectra was done, combined with BET, ICP-OES, TPD and XRD in order to identify unambiguously the nature of the species formed at the surface. In particular ^{19}F MAS NMR measurements are expected to provide valuable information since fluorine is not originally present in the bulk of the solids.

6.2 XRD Characterization

The X-ray powder diffractograms of unmilled and milled γ-Al_2O_3 applying different milling times are compared in **Figure 6.2**, a). For milling treatments shorter than 30 min two features can be evidenced. First, the typical reflections of γ-Al_2O_3 (37.8°, 45.9°, 66.6°; PDF No. 29-63) are still present after milling. Second, the amplitudes of the reflections decrease and the width increases with milling time. For milling processes longer than 30 min not only the γ phase is present. A transition phase of alumina occurs

in addition. Indeed reflections corresponding to the δ phase (PDF No. 4-877) can be assigned after 1 h milling. After 4 h milling treatment narrower peaks belonging to the crystalline structure of corundum (α-Al_2O_3) are present in addition. Anyway the transition to α-Al_2O_3 is still not completed after 4h milling.

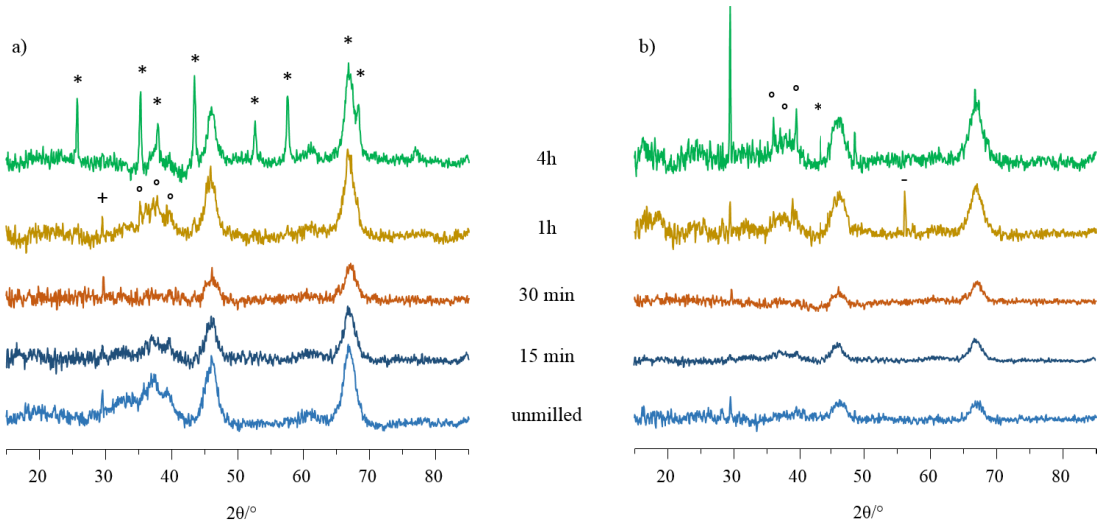

Figure 6.2: X-ray diffractograms of y-Al_2O_3 samples differently treated (in the milling time) a) before and b) after contact with NaF solution. Reflections of *) α-Al_2O_3 (PDF No. 10-173); °) δ-Al_2O_3 (PDF No. 4-877) ; -) NaF (PDF No. 88-2299); +) sample holder.

Figure 6.2, b shows the X-ray powder diffractograms of the same samples (unmilled and milled γ-Al_2O_3) after contact with NaF solution. For milling time shorter than 1h, just a broadening of the typical reflections of γ-Al_2O_3 can be observed. Only after 1h milling, a significant variation of the XRD pattern can be observed. The diffractogram of the 1h milled sample shows also a peak which can be assigned to NaF (PDF No. 88-2299). Reflections which evidence a transition phase of alumina can be detected just after 4h milling. The signal recorded at around 30° (visible in almost all diffractograms) is related to the sample holder. The reflections corresponding to different phases are clearly signed in the figure and assigned in the caption.

6.3 ^{27}Al and ^{19}F MAS NMR Characterization

The ^{27}Al NMR spectra of all γ-Al_2O_3 samples just after the milling process can be found in **Figure 6.3**. All spectra clearly show the typical ^{27}Al signals for (AlO_4)- and (AlO_6)-coordinations in γ-Al_2O_3. The most evident change with increasing the milling time is

the shift of the maximum of the main AlO_6- peak (highlighted by a dotted line) to the characteristic value of α-Al_2O_3 (at 12 ppm).

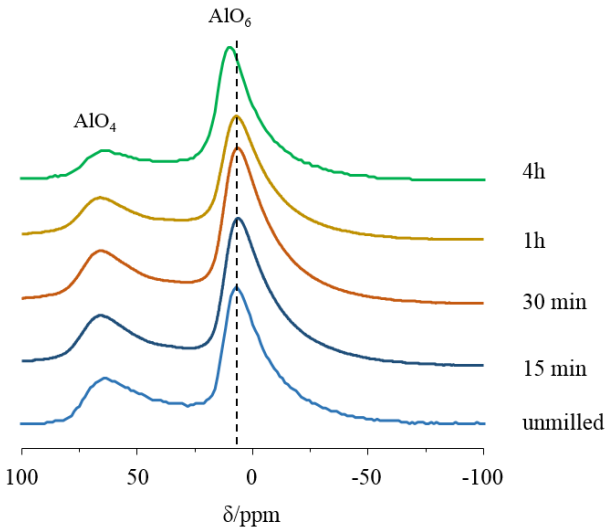

Figure 6.3: ^{27}Al MAS NMR (central lines, ν_{rot}= 20 kHz) spectra of γ-Al_2O_3 milled for different milling times. The dotted line as a guide for the maxima shift.

A comparison of the ^{27}Al MAS NMR spectra of the samples before (black line) and after (dotted line) contact with NaF solution is shown in **Figure 6.3**. All the signals are normalized to the intensity of the main peak at about 6 ppm. A change in the ratio of the signal assigned to the 6-fold coordinated Al sites (Al^{VI}, around 6 ppm) to the one assigned to the 4-fold coordinated Al sites (Al^{IV}, around 67 ppm) can be observed after contact with NaF solution. A decrease of the signal intensities at about 67 ppm and about 42 ppm (assigned to the 5-fold coordinated Al sites) signals occur at every milling time applied.

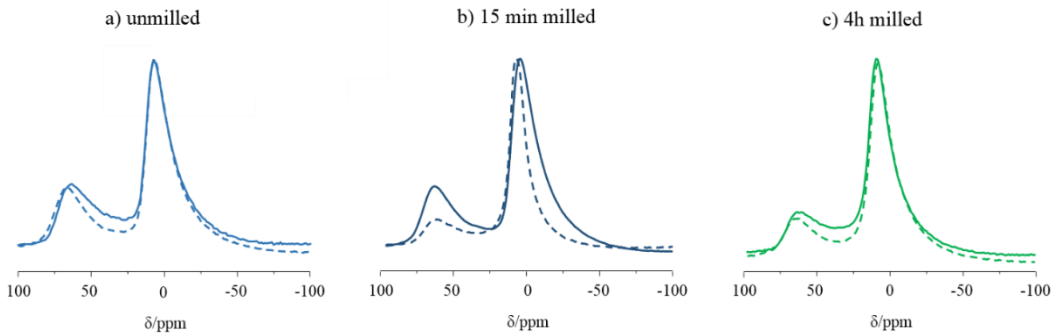

Figure 6.4: Comparison of ^{27}Al MAS NMR spectra of samples milled for different times before and after contact with NaF solution. Dotted line: NMR spectrum after contact of the sample with NaF solution.

Figure 6.5 shows the ^{19}F MAS NMR spectra of unmilled and milled γ-Al_2O_3 after contact with NaF solution. The NMR spectrum of the liquid NaF is added for comparison (**Figure 6.6**). Considering first the ^{27}Al MAS NMR spectra of the samples after contact with NaF solution, the main obvious change can be noticed in the spectrum of the 1 h milled sample. An additional shoulder occurs at about -0.5 ppm, finally shifting the upfield decay to the higher field.

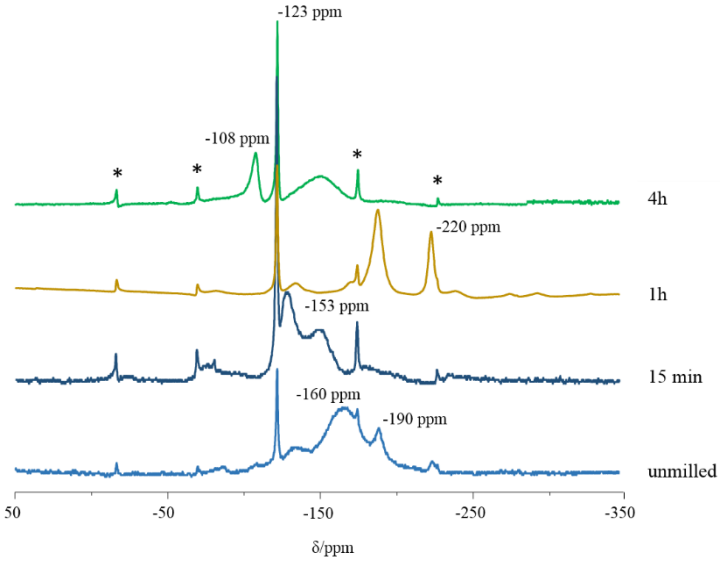

Figure 6.5: ^{19}F MAS NMR spectra (ν_{rot}= 20 kHz) of unmilled and milled γ-Al_2O_3 after contact with NaF .solution. *: spinning sidebands.

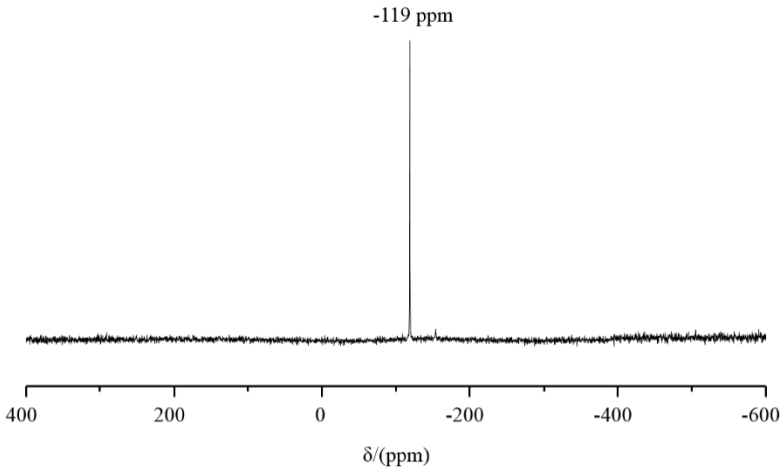

Figure 6.6: ^{19}F NMR spectrum of the NaF aqueous solution used for performing the experiments.

Milling time strongly influences the amplitude and the chemical shifts of these signals in the mentioned region, which represent fluorinated species on the surface of

aluminium oxide. In **Figure 6.7** a DMFIT simulation of the spectra of the unmilled and 4h milled γ-Al_2O_3 after contact with NaF solution can be observed.

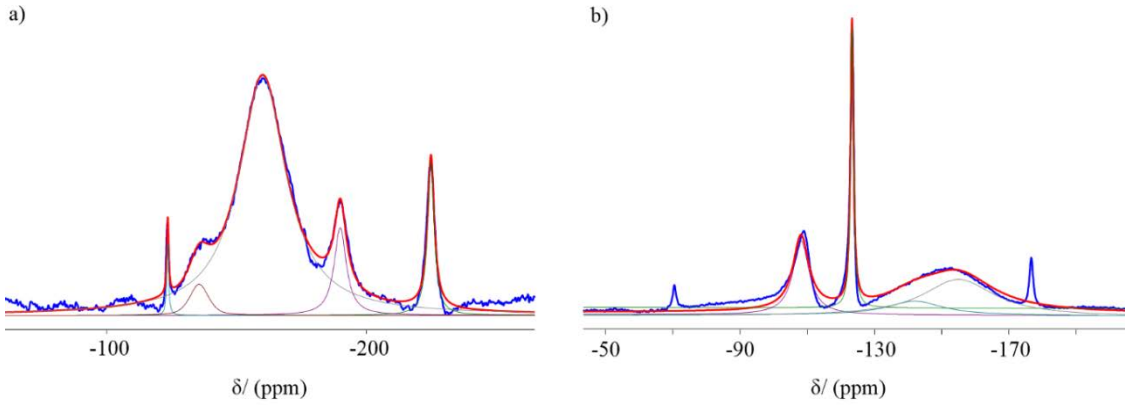

Figure 6.7: ^{19}F MAS NMR spectra of a) unmilled y-Al_2O_3 and b) 4h milled y-Al_2O_3 after contact with NaF solution (blue curves); simulated spectra (red curves) and individual components (colored) were obtained by using the DMFIT software[62].

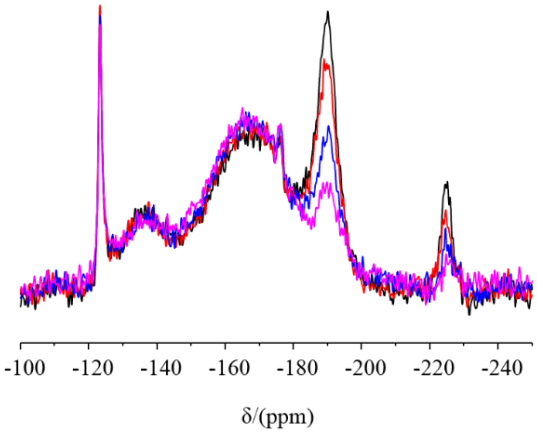

Figure 6.8:^{19}F MAS NMR spectra of the unmilled γ-Al_2O_3 after contact with NaF solution. Recycle delays of D1= 5 s (pink), 10 s (blue), 20 s (red), 30 s (black).

Concerning the ^{19}F MAS NMR, each spectrum obtained for different milling times of the γ-Al_2O_3 is characterized by distinct and partially different resonances. For the untreated γ-Al_2O_3 a small signal at -220 ppm is evident, which can be assigned to NaF species. The same signal does not occur for a milling time of 15 min but it shows its highest intensity increasing the milling time to 1 h, applying the same measurement conditions for all spectra. The ^{19}F NMR spectrum of the untreated γ-Al_2O_3 also shows a

signal at -190 ppm which can be assigned to Na_3AlF_6. As for the signal at -220 ppm, its highest intensity was recorded for the sample milled for 1 h. Independent of the milling time, two more signals lay within the typical region (between -170 ppm and -130 ppm) for species containing fluorine bonded directly to aluminium. The signal at around -160 ppm can be assigned to AlF_xO_{6-x}-species with high F^- content [64]. **Figure 6.8** shows how these signal intensities increase with increasing the time of the recycle delay. This means that well crystalline Na_3AlF_6 and NaF particles are present in the as-prepared powder. The latter could be a consequence of dissolution-precipitation processes.

Table 6.1: Chemical shifts of F- species observed in the ^{19}F MAS NMR spectra of all samples with possible assignments and referred literature. * F coordinated by 3-Al cations in the structure of α-Al_2O_3. **personal communication, to be published.

δ_{iso} ^{19}F (ppm)	Possible assignment	Reference
-108	$[FAl_3]$-sites *	J.Budau, B. Paulus **
-123	$(F^-_{(aq)})$ adsorbed	9, Figure 6.6
-139	$AlF_x(OH)_y$	64, 65
-150	AlF_3O_3	64, 65
-163	AlF_5O/AlF_6	64, 65
-192	Na_3AlF_6	65
-220	NaF	67

Another distinct and new fluoride ion site well resolved is evident in the ^{19}F NMR spectrum of the 4 h milled sample; the signal at -108 ppm can be assigned to fluoride ions in a typical corundum environment (whose formation was already discussed above). A very narrow signal which is constantly present in each ^{19}F MAS NMR spectrum is recorded at about -123 ppm, and it can be assigned to fluorine adsorbed on the oxide surface in a hydrated environment. A summary of all the F^- species observed in all the ^{19}F MAS NMR spectra and potential assignments can be found in **Table 6.1**.

6.4 ICP- EOS Characterization

Table 6.2 summaries the Al contents determined by ICP-OES after the dissolution of each powder in water. A trend can be observed except for the sample milled for a time of 15 min. The amount of Al in solution is decreasing with increasing milling time.

Table 6.2: Concentration of Al in aqueous solution determined by ICP measurements after dispersion in water.

Milling time	ppm Al (mg Al/l)
Unmilled	77,62 ± 2,22
15 min	79,67 ± 1,76
30 min	60,37 ± 0,82
1 h	59,39 ± 0,49
4 h	36,49 ± 0,64

6.5 BET Specific Surface Area Measurement

An analysis of the values reported in **Table 6.3** evidences how the specific surface area decreases with increasing milling time. Commercially available γ-Al_2O_3 shows the highest surface area (220 m^2/g). With increasing milling time, the specific surface area is decreasing. The lowest surface area was recorded for the 4 h milled γ-Al_2O_3, which is, as already mentioned, a mixture of α- and γ- alumina.

Table 6.3: Specific surface area values of the unmilled and milled γ-Al_2O_3 (before contact to NaF-solutions).

Milling time	S_{BET} (m^2/g)
Unmilled	220
15 min	157.3
30 min	137.9
1 h	106.6
4 h	26.2

6.6 NH_3-TPD Characterization

Figure 6.9 gives clear evidence of the change of the presence and the strength of acid sites for each unmilled and milled sample. The NH_3-TPD-graphs indicate that there is no doubt about the presence of both Brønsted and Lewis sites independent from the milling time. Changes can be observed by increasing the milling time. For the unmilled γ-Al_2O_3, two main peaks were recorded (at 170 °C and 270 °C), as also reported in literature[99]. The intensity of the second peak is decreasing after a milling treatment of 15 min. The sample milled for 1 h shows a different kinetic of NH_3 desorption. For a milling time of 30 min and 4 h, just one peak was recorded.

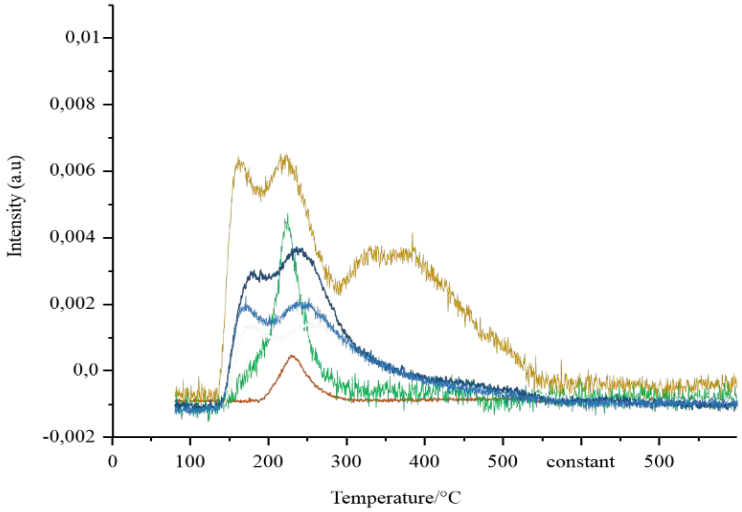

Figure 6.9: NH_3-TPD desorption profiles of unmilled (soft blue) γ-Al_2O_3, 15 min milled γ-Al_2O_3 (dark blue), 30 min milled γ-Al_2O_3 (orange), 1 h milled γ-Al_2O_3 (yellow) and 4 h milled γ-Al_2O_3 (green). The relative amount of desorbed NH_3 is on the y-axis.

6.7 Conclusions

A detailed characterization of different mechanically activated γ-Al_2O_3 samples was performed in the present study. The structural disorder was introduced by high energy ball milling. The X-ray patterns show the progressive amorphisation of γ-Al_2O_3 with the increase of the milling time. Indeed a broadening of the main reflections of γ-Al_2O_3 was observed (**Figure 6.2**, a). That can be due to a reduction of the particle size, which is a typical effect of the milling process. After 1h milling, the formation of a mixture of δ- and γ-phases is confirmed by XRD measurements. For a milling time of 4h, as already

explained, the ongoing transition to the α-Al_2O_3 phase occurs. After contact of the pretreated samples with a NaF solution, an additional degradation of the amplitudes and a broadening of all reflections was observed. Thus, the adsorption of fluoride at the surface (due to the contact with a NaF solution) of the unmilled and milled samples amplifies the degree of amorphisation for all milling times.

Although all the samples are on a first view mainly unchanged γ-Al_2O_3, they differ in properties such as surface area, solubility, amount of acid sites and adsorption of fluoride from solution. Mechanochemical treatments usually introduce an increase of the surface area of the samples, due to a decrease of the particle size. However, in our case the destruction of the already present porous structure in γ-Al_2O_3 seems to be the dominating effect; the longer the milling time is the lower is the surface area. The lowest surface area value obtained for the sample milled for 4h confirms the formation of a structure with a long-range order, here α-Al_2O_3, as the narrow reflections of the X-ray pattern of the same sample also do.

The activity of a catalyst can depend on the pore size. For our samples, the number of catalytically active surface sites seems to be strongly dependent on the pretreatment. The increase of these numbers after a short milling time may be due to the formation of a higher amount of defects created by the mechanical treatment. As shown in the TPD-desorption profiles, the sample characterized by the highest surface area has not necessarily the highest amount of acid sites. ICP measurements show also differences in the solubility of the samples depending on the pretreatment. The sample milled for 15 min showed the highest solubility and also a consistent and expected increase in the amount of acid sites. Therefore, a milling time of 15 min seems to be an optimum time for the pretreatment of γ-Al_2O_3 for catalytic applications.

As already observed for the BET surface areas of the milled samples, the solubility trend is inconsistent with the expected one (**Table 6.3**). This can only be understood in the context with the early formation of crystalline Al_2O_3 phases, which are finally less soluble.

As expected then, the capability of F^-adsorption for every sample is also different. And the actual adsorption of fluorine at the surface was proven by the measurement of the ^{19}F MAS NMR spectra of the unmilled and milled samples after contact with a NaF solution. It is important to note that all in all 7 different ^{19}F MAS NMR signals were

assigned to different F^- species at the surface of untreated and treated γ-Al_2O_3 (see **Figure 6.5**).

Adsorbed hydrated F^- ions from the NaF solution can be observed in each ^{19}F MAS NMR spectrum at about -123 ppm. For comparison, the ^{19}F spectrum of an aqueous NaF-solution is given in **Figure 6.6**. The ^{19}F chemical shift trend analysis for AlF_xO_{6-x} species proposed by König at al.[64] was used to assign the signals in the region between -130 ppm and -160 ppm. Milling time strongly influences the amplitude and the chemical shifts of these signals in the mentioned region, which represent fluorinated species on the surface of aluminium oxide. For unmilled γ-Al_2O_3, additional signals appear at about -190 ppm and -220 ppm, which can be assigned to Na_3AlF_6 (cryolite) and NaF, respectively. **Figure 6.8** shows how these signal intensities increase with increasing the time of the recycle delay. This means that well crystalline Na_3AlF_6 and NaF particles are present in the as-prepared powder. The latter could be a consequence of dissolution-precipitation processes.

The ^{19}F MAS NMR signal at -190 ppm was as well observed in the study published by Shimizu at al. and was assigned in that paper to $NaHF_2$ existing on the aluminium hydroxide/water interface. But neither the intensity distribution of the spinning side bands nor the expected anisotropy of the signal do actually match those of $NaHF_2$. Unfortunately, no ^1H MAS NMR spectrum was shown in, which should give a direct evidence of the formation of $[HF_2]^-$ with a strongly bridged proton, identified by a distinctly low-field shifted ^1H signal. In our case, no strongly bridged ^1H species can be observed by spin-echo NMR experiments. Following the given arguments we assume that both in the present and in the previous study the ^{19}F signal observed at -190 ppm belongs to Na_3AlF_6.

Distinct ^{19}F MAS NMR signals at -190 ppm and -220 ppm were observed also for the sample milled for 1h. The local formation of Na_3AlF_6 is also evident in the ^{27}Al MAS NMR spectrum which exhibits an additional shoulder at -0.5 ppm. As already mentioned, the X-ray pattern of this sample reveals already the coexistence of two different transition phases (δ- and γ-) of aluminium oxide, and obviously also cryolite, not visible in the powder diffractogram. This mixture of phases defines the highest number of acid sites by NH_3-TPD adsorption.

The 4h milled sample shows a new ^{19}F signal at -108 ppm. We checked carefully that this signal is not due to the presence of impurities. It was in fact also already

observed in the ^{19}F MAS NMR spectrum of Al-hydroxides annealed at 1400 °C, a temperature at which the transition to corundum is surely completed. In addition, this chemical shift was assigned to 3-fold coordinated F ions on the surface of corundum by DFT calculation from J. Budau and the Paulus group (FU, Berlin).

Mechanical treatment has a strong impact on the structure of γ-Al_2O_3. The high number of defects introduced by milling defines the formation of highly distorted Al-oxide phases. Their degree of amorphisation is strongly influenced by the milling time. It was observed that a time of milling higher than 1 h induces the transition to different Al-oxide phases. A detailed study of the surface properties (made by BET and NH_3-TPD measurements) of the unmilled and milled γ-Al_2O_3 points out how the impact of milling does not only affect just the bulk of the aluminium oxides. Once the unmilled and milled γ-Al_2O_3 are exposed to a NaF aqueous media, the degree of amorphisation seems actually to increase. Applying ^{19}F MAS NMR spectroscopy it was possible to discriminate between 7 different F-species either adsorbed at the surface or present as coexisting particles in the powder samples. A potential assignment of those species was proposed after an accurate analysis of the chemical shifts. The adsorption of fluorine from solution should guarantee moreover the presence of fluoride ions just at the surface of the unmilled and milled γ-Al_2O_3 since it is not originally present in the bulk of the solids. The unmilled and milled γ-Al_2O_3 surfaces fluorinated that way offer potential application as catalysis support material.

Chapter 7. Summary and Future Outlooks

The presented Ph.D. work sets out to demonstrate the capability of the mechanochemical technique as a tool for synthesizing highly distorted aluminium hydroxide fluorides. This solvent-free synthesis not only allows the introduction of a high number of defects in the structures of the starting materials but also changes their structures dependent on the starting material and water supply. The fluoride doping contributes to an increased degree of amorphisation. Simply by milling the long-range order of the Al hydroxides and oxides is lost because of the mechanical action. The result is an almost X-ray amorphous product. In the case of corundum (α-Al_2O_3), the intensity of the X-ray reflections decreases and peaks get broader. Except for the α-Al_2O_3 case and the visible partial formation of α-Al_2O_3 starting from γ-Al_2O_3, the high degree of amorphisation makes the interpretation of X-ray powder diffractograms of the obtained products impossible or at the least, difficult. The most relevant information about the structure of the products was gained with the use of solid state NMR spectroscopy. Although the ^{27}Al MAS NMR spectra do not exhibit significant changes after fluorine doping by milling, the ^{19}F MAS NMR spectra interestingly and selectively confirm the presence of different fluorine species in the resulting products.

Three essential parameters (fluorination degree, amount of water and milling time) have been considered in order to evaluate their distinct impact on the resulting product. Each parameter characterizes each of the chapters of this Ph.D. thesis.

As discussed in the 4th chapter, the mechanical impact strongly affects the phase transition of γ-$Al(OH)_3$ to corundum. As a consequence of the combined action of milling and fluoride doping the number of introduced defects is remarkably higher compared to a separate milling of the reactants. The introduction of fluorine in different Al: F molar ratios (higher than 1: 1) leads to the formation of strongly disordered products. A higher degree of fluorination results in a more crystalline product. In contrast to the crystalline aluminium hydroxide fluoride and to γ-$Al(OH)_3$, the amorphous products exhibit a higher amount of unsaturated Al sites. In particular, the signal corresponding to 5-fold coordinated Al species presents noticeable intensity. After removing the physisorbed water by heating at 120 °C, the amount of unsaturated Al sites increases. Further investigations about the dehydroxylation process of the amorphous products can be made.

In the 5th chapter, we systematically varied the water content of the reactants and tried to elucidate the role of water in the mechanochemical synthesis of low fluorine

doped aluminium (hydr-) oxides. First, it has to be considered that the water was introduced in the synthesis just as the structural water of the reactants. No other solvents were included in the synthesis. In this specific case, it is evident that water improves the fluorination of the Al (hydr-) oxides, which results in a more homogenous distribution of the fluorine species in the structure and at the surface of the aluminium (hydr-) oxides is obtained by mechanochemistry. The presence of water favours the implementation of fluorine and guarantees an almost homogeneous distribution of F-sites in the products.

As shown in the 6th chapter, the degree of amorphisation of the highly distorted Al-oxide phase is strongly influenced by the milling time. It was observed that a time of milling higher than 1 h induces the transition to different Al-oxide phases. A detailed study of the surface properties (made by BET and NH_3-TPD measurements) of the unmilled and milled γ-Al_2O_3 demonstrates how the impact of milling does not only affect just the bulk of the aluminium oxides. Once the unmilled and milled γ-Al_2O_3 are exposed to a NaF aqueous media, the degree of amorphisation appears actually to increase. Applying ^{19}F MAS NMR spectroscopy it was possible to discriminate between 7 different F-species either adsorbed at the surface or present as coexisting particles in the powder samples. A potential assignment of those species was proposed after an accurate analysis of the chemical shifts. The adsorption of fluorine from solution should guarantee moreover the presence of fluoride ions at the surface of the unmilled and milled γ-Al_2O_3 since it is not originally present in the bulk of the solids. Both so fluorinated unmilled and milled γ-Al_2O_3 surfaces offer potential application as catalysis support material.

Chapter 8. Materials and Methods

All studies and measurements were performed in the Institut für Chemie at the Humboldt-Universität zu Berlin unless otherwise specified.

8.1 Materials

Commercially available Al-(hydr-) oxides and Al-fluorides were used in this research work. Especially all the chemicals were delivered by the followed companies: Sigma-Aldrich, Fluka, Almatis. In particular, γ-$Al(OH)_3$ was provided by Fluka and presents a purity grade higher than 95 % (reaction grade); β-$AlF_3 \cdot 3H_2O$, α-AlF_3 and γ-Al_2O_3 by Sigma Aldrich (respectively with a purity of 97 %, 99.9 +% and 99.99 %); α-Al_2O_3 by Almatis and performs a purity of 99.8 %. No further purification was performed. In order to define a low F doping, each synthesis was in a molar ratio Al: F= 1: 0.25 and Al: F= 1: 0.05. Most of the reactions showed here were carried out with a molar ratio of Al: F= 1: 0.25.

8.2 Synthesis Route

Ball milling technique is well-known for the simplicity of the synthesis route. In this research project, in order to carry milling experiments, a commercial planetary mill "Pulverisette7- premium line (Fritsch, Germany) was used. Five ZrO_2 balls were used in each ZrO_2 vial (m_{balls} = 14.9 g; m_{sample} = 1 g) with a steel casing. The volume of each milling bowl is 45 ml. All the syntheses were performed on air. Each reaction was carried generally for a milling time of 4h at a rotational speed of 600 rpm, when not differently specified.

8.2.1 ^1H-^2H Exchange

The sample was exposed to a D_2O atmosphere by keeping it in a vacuum desiccator which contained D_2O in a separate beaker for four weeks. To maintain a good seal, vacuum grease was applied.

8.2.2 Classical Solid State Reaction

The classical solid state reactions were performed by inserting a platinum crucible (Q-crucible) containing the reactants into a Eurotherm furnace, Carbolite RHF 16/3. The top of the platinum crucible was not totally closed. The syntheses were carried out at a temperature of 500 °C for 2 h.

8.3 Bulk Characterization Methods

All the analytical techniques and the corresponding devices used in the present Ph.D. work are shortly described in the following paragraphs.

8.3.1 XRD

X-ray powder diffraction (XRD) is a powerful nondestructive analytical technique primarily used for phase identification of a crystalline material and can provide information on unit cell dimensions. X-ray diffraction peaks are produced by constructive interference of a monochromatic beam of X-rays diffracted at specific angles from each set of lattice planes in a sample. Diffraction occurs just when the Bragg´s law satisfies the condition for constructive interference. The peak intensities are determined by the distribution of atoms within the lattice. Consequently, the X-ray diffraction pattern is the fingerprint of the periodic atomic arrangements in a given materia**l.**

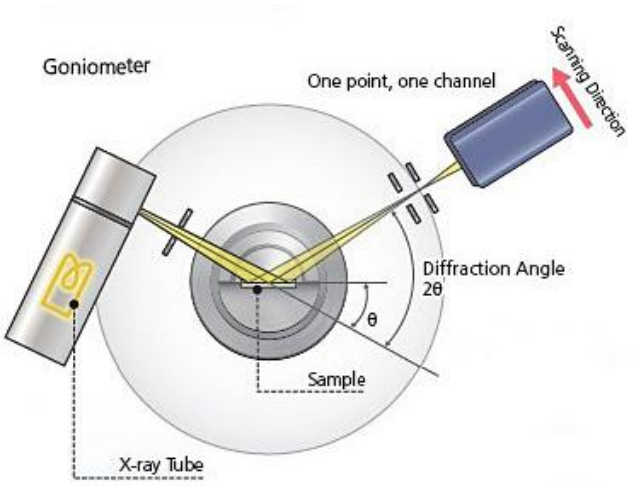

Figure 8.1: Scheme of the inner of a Bragg spectrometer.

In this study, XRD measurements were performed using the FPM 7 equipment (Rich, Seiffert & Co., Freiberg) with Cu Kα radiation (Cu $K\alpha_{1,2}$, λ = 1.542 Å, 2θ range: 5° < 2θ < 90°, step scan: 0.05°, step time: 5s). Phases were identified by comparison with JCSD powder database [100].

8.3.2 Solid State MAS NMR (^{19}F, ^{27}Al) Spectroscopy

Solid-state NMR spectroscopy can provide valuable information about molecular and supra-molecular local structures. In the solid state, anisotropic spin interactions such as the chemical shift anisotropy or dipolar couplings contain unique spatial and dynamic information. However, these interactions lead to broad and overlapping spectral lines, which obscure the familiar isotropic chemical information known from solution-state NMR spectroscopy. In order to obtain high-resolution, it is necessary to remove the broadening due to this anisotropic interactions. The most convenient way to achieve this goal is rapid sample rotation at the so-called "magic" angle (MAS) relative to the static magnetic field (**Figure 8.2**). Magic angle spinning (MAS) has the effect of averaging the chemical shifts for different molecular orientations within the sample and to average out dipolar interactions.

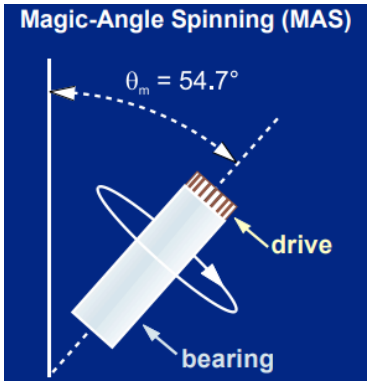

Figure 8.2: Magic-Angle Spinning (MAS) imposes a collective reorientation of all the molecules around a special axis.

^{19}F and ^{27}Al MAS NMR spectra were recorded on a Bruker AVANCE 400 spectrometer (Larmor frequencies: ν_{19F}=376.4 MHz, ν_{27Al}=104.6 MHz) using a 2.5 mm magic angle spinning (MAS) probe (Bruker Biospin) and applying a spinning speed of 20 kHz if not otherwise indicated. ^{19}F MAS NMR (I = 1/2) spectra were recorded with a $\pi/2$ pulse duration of 3.6 µs, a spectrum width of 400 kHz and a recycle delay of 5 s. Spectral

changes for longer recycle delays were checked. Isotropic chemical shifts of ^{19}F are given with respect to the $CFCl_3$ standard. Background signals of ^{19}F could be completely suppressed with the application of a phase-cycled depth pulse sequence according to Cory and Ritchey[101]. ^{27}Al MAS NMR (I = 5/2) spectra were recorded with an excitation pulse duration of 1 μs. A 1 M aqueous solution of $AlCl_3$ was used as a reference for the chemical shift of ^{27}Al.

In this Ph.D. work spin-echo and cross polarization experiments were performed.

The spin echo works by irradiating a sample with two RF pulses and observing an echo signal that has its adsorption peak at some time after the RF pulses. More specifically, start with a 90° excitation pulse, wait a short time period τ, then apply a 180° refocusing pulse, wait another equal time period τ for the peak of the spin echo signal to occur. Individual spins in MR have such low energy that they are not observed independently. Instead, we observe the combined signal of all the spins within the sample. Immediately after the 90° RF excitation pulse, all the spins are in phase and add coherently to form the maximum signal. In real-life situations, these spins start to dephase immediately as some precess faster, and some slower, than the average. As the spins move further out of phase with each other, they don't add together as effectively, and the sum of all the spins starts to decrease (or "decay").

The greatest value of CP is in enhancing the signals of low abundant nuclei (^{13}C or ^{15}N) that are dipolar coupled to proton spin bath. In addition, the modern development of CP has led to recent experiments that perform highly selective coupling among nuclei. For the ^{1}H-^{2}H CP MAS NMR (**Figure 4.14**), a pulse sequence employing direct excitation of ^{1}H (abundant nucleus) spin polarization is followed by a CP transfer to and a signal detection of ^{2}H (rare nucleus).

8.3.3 TG/DTA

Solid state chemistry uses thermal analysis for studying reactions in the solid state, thermal degradation reactions and phase transitions and phase diagrams. Thermal analysis includes a different kind of methods depending on the measured properties. The thermogravimetric analysis (TGA) evaluates then the mass and the differential thermal analysis (DTA) the temperature difference. In principle, this last one combines the ease of the measurement of the heating or the cooling curves with the quantitative

features of calorimetry[102]. Classical DTA measures the difference in temperature between the sample and reference (which undergoes no phase changes) as the furnace goes through a computer controlled temperature program. The temperatures of both the sample and reference material increase (or decrease) uniformly until the sample reaches a point that it undergoes a phase change, which is either endothermic or exothermic and the difference in temperature is recorded. The thermal behavior was studied by conventional thermal analysis (TA) in air. A NETZSCH thermoanalyzer STA 409 C Skimmer, is additionally equipped with a conventional high-temperature SiC oven, was used to record the thermoanalytical curves (DTA, TG, and DTG). 50-65 mg of sample was measured versus an empty crucible.

8.4 Surface Characterization Methods

8.4.1 NH_3-TPD

The Temperature-Programmed Desorption (TPD) of ammonia (NH_3-TPD) is one of the most widely used and flexible techniques for characterizing the acid sites on oxide surfaces. NH_3-TPD was employed to determine the presence and the strength of acid sites of unmilled, milled and fluorinated samples. Determining the quantity and strength of the acid sites on alumina, amorphous silica-alumina, and zeolites it is crucial to understanding and predicting the performance of a catalyst. For several significant commercial reactions (such as n-hexane cracking, xylene isomerization, propylene polymerization, methanol-to-olefins reaction, toluene disproportionation, and cumene cracking), all reaction rates increase linearly with Al content (acid sites) in H-ZSM-5. In the NH_3-TPD technique its small molecular size allows ammonia to penetrate into all pores of the solid where larger molecules commonly found in cracking and hydrocracking reactions only have access to large micropores and mesopores. The activity depends on many factors, but the Brønsted-acid site density is usually one of the most crucial parameters. The samples (around 50 mg) were first heated under Ar up to 150 °C and kept at 150 °C for 1h, cooling down to 120°C and exposing to NH_3. After cooling down to 80 °C and flushing physisorbed ammonia with Ar for about 30 min, the TPD program was started (10K/min up to 500 °C, keeping the temperature at 500 °C for

30 min). Desorbed ammonia was continuously monitored using IR spectroscopy (FT-IR system 2000, Perkin-Elmer).

8.4.2 BET

A brief description and discussion about the limits of all the techniques used for the determination of the specific surface area and especially of the called Brunauer- Emmet-Teller (BET) method was given by Leofanti et al. in 1998[68]. The BET model, developed in the 40s, still remains the most used tool for determining the monolayer volume of the adsorbate (usually nitrogen) and from it the value of the surface area of the solids. Nitrogen adsorption at boiling temperature (77 K) is the technique which applied the BET method and also the most widely one to characterize the pore texture of solids, which arises mostly during the preparation methods of these solids. Consequently, the shape of the isotherms obtained by this technique depends on the solid pore texture. According to IUPAC classification (1984), four different types of adsorption hysteresis loops can be distinguished[103].

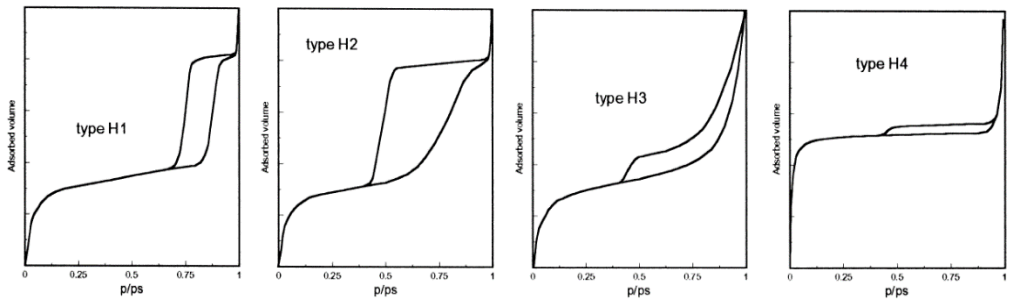

Figure 8.3: The four types of hysteresis loops identified by IUPAC in 1984.

In this research work the BET surface area was calculated by using a Physisorption Analyzer ASAP 2020 (Accelerated Surface Area and Porosimetry System) by Micrometrics. Each sample was first heated at 125 °C for 72 h in order to remove the physisorbed water. After heating, a 12 h-long degassing process (at $5 \cdot 10^{-5}$ mbar) of each sample at room temperature was done. Pore size distribution was determined by the Barret-Joyner-Halenda (BJH) method, applied to the desorption branch of the isotherm.

8.4.3 Zeta Potential

Because a layer of immobile ions and water molecules exists at the surface, it is not straightforward to directly measure the surface potential of particles. Instead, a closely related potential known as the z potential is usually measured. The zeta potential is measured through experiments where relative motion between the surface and the solution is required.

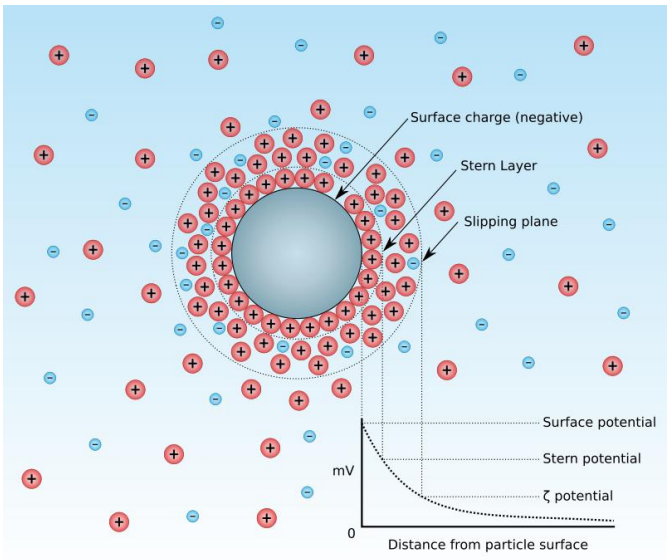

Figure 8.4: Ionic concentration and potential difference as a function of distance from the charged surface of a particle suspended in a dispersion medium. A schematic representation of the meaning of Zeta Potential (ξ).

It is considered as the potential at the plane of shear between the immobilized surface layer and the bulk solution (shipping plane, **Figure 8.4**). This plane is typically located only a few angstroms from the surface so the difference between the z potential and the surface potential is usually not much. The zeta potential corresponds even more closely with the diffuse layer potential, which is largely responsible for controlling the Electrical Double Layer (EDL) interaction force between surfaces. The pH where the z potential is zero is known as the IsoElectric Point (IEP). Dynamic light scattering (DLS) for characterization of zeta potential (ζ) was done using a Malvern Instruments Zeta-sizer Nano. The samples were diluted in water (0.01 wt %) and the mixture was ultrasonicated for 2 min prior to measurements. Titration was performed using a Malvern Instruments MPT-2 Autotitrator. The pH of the suspension was adjusted adding NaOH or HCl. The zeta potential was determined as a function of either pH in a range between 4 and 10. Each measurement was repeated three times.

8.4.4 ICP-OES

The ICP-OES is an analytical technique in which the composition of elements in (mostly water dissolved) samples can be determined using plasma and a spectrometer. The ICP-OES measurements were performed in an IRIS Intrepid Duo spectrometer (Thermo Elemental, USA) for the determination of the Al content. Samples were dispersed in H_2O by magnetic stirring at 400 rpm for 24 h. Microwave (ETHOS plus-MLS GmbH, Germany) digestion at 220 °C for 20 min was accomplished before each measurement. A special thanks to Dr. R. Bertram for performing the ICP-EOS measurements at the Leibniz-Institut für Kristallzüchtung in Adlershof, Berlin.

Chapter 9. References

1. Aoba, T. The effect of fluoride on apatite structure and growth. *Crit. Rev. Oral Biol. Med.* **8,** 136–153 (1997).

2. Kakei, M., Sakae, T., Yoshikawa, M. & Tamura, N. Effect of fluoride ions on apatite crystal formation in rat hard tissues. *Ann. Anat.* **189,** 175–181 (2007).

3. Kuznetsov, S. V, Osiko, V. V, Tkatchenko, E. A. & Fedorov, P. P. Inorganic nanofluorides and related nanocomposites. *Russ. Chem. Rev.* **75,** 1065–1082 (2006).

4. Ahrem, L., Scholz, G., Bertram, R. & Kemnitz, E. Thermal evolution of 4- and 5‑fold coordinated Al-sites in aluminium hydroxide fluorides with low fluorination degree. *J. Phys. Chem. C* **120**, 9236–9244 (2016).

5. Ritter, B., Haida, P., Krahl, T., Scholz, G. & Kemnitz, E. Core-shell metal fluoride nanoparticles via fluorolytic sol-gel synthesis – a fast and efficient construction kit. *J. Mater. Chem. C* **5,** 5444–5450 (2017).

6. Scholz, G. *et al.* Mechanochemical synthesis of MgF_2 - MF_2 composite systems (M Combining double low line Ca, Sr, Ba). *Solid State Sci.* **50,** 32–41 (2015).

7. Heise, M., Scholz, G., Düvel, A., Heitjans, P. & Kemnitz, E. Mechanochemical synthesis, structure, and properties of solid solutions of alkaline earth metal fluorides: $M^a_{1-x}M^b_xF_2$ (M: Ca, Sr, Ba). *Solid State Sci.* **60,** 65–74 (2016).

8. Al-Terkawi, A. A., Scholz, G., Emmerling, F. & Kemnitz, E. Mechanochemical synthesis, characterization, and structure determination of new alkaline earth metal-tetrafluoroterephthalate frameworks: Ca(pBDC-F_4)·$4H_2O$, Sr(pBDC-F4)·$4H_2O$, and Ba(pBDC-F_4). *Cryst. Growth Des.* **16,** 1923–1933 (2016).

9. Scholz, G., Brehme, S., Balski, M., König, R. & Kemnitz, E. Structure and properties of mechanochemically synthesised aluminium hydroxide fluoride phases $AlF_x(OH)_{3-x}$· nH_2O. *Solid State Sci.* **12,** 1500–1506 (2010).

10. Stosiek, C., Brehme, S., Scholz, G. & Kemnitz, E. Influence of milling, sonication and fluoride doping of pseudoboehmites on their phase transformation behaviour to corundum. *J. Eur. Ceram. Soc.* **29,** 2713–2720 (2009).

11. Takacs, L. The historical development of mechanochemistry. *Chem. Soc. Rev.*

42, 7649 (2013).

12. Ling, A. R. & Baker, J. L. Halogen derivatives of quinone. Part III. Derivatives of quinhydrone. *Chem. Soc*. **63**, 1314 (1893),

13. Ostwald, W. Lehrbuch der allgemeinen chemie. *Engelmann* 930, 2 (1887).

14. Peters, K. *Mechanochemische Reaktionen*. *Symp. Zerkleinern. Verlag Chemie, Weinheim,* VDI Verlag (1962).

15. J. Lin, S. N. Review of the phase transformation and synthesis of inorganic solids obtained by mechanochemical treatment (mechanochemical reactions). *Mater. Sci. Eng.* **39,** 193–209 (1979).

16. Fox, P. G. Mechanically initiated chemical reactions in solids. *J. Mater. Sci.* **10,** 340–360 (1975).

17. Boldyrev, V. V. Mechanochemistry of Inorganic Solids *Termochim. Acta* **110**, 303-317 (1987).

18. Roy, R. Accelerating the kinetics of low-temperature iInorganic syntheses. *J. Solid State Chem.* **111,** 11–17 (1994).

19. Juhász, Z. A. Colloid-chemical aspects of mechanical activation. *Part. Sci. Technol.* **16,** 145–161 (1998).

20. Boldyrev, V. V. & Tkáčová, K. Mechanochemistry of solids: Past, present, and prospects. *J. Mater. Synth. Process.* **8,** 121–132 (2000).

21. Takacs, L. & Carey Lea, M. The first mechanochemist. *J. Mater. Sci.* **39,** 4987–4993 (2004).

22. Gossweiler, G. R. *et al.* Mechanochemical activation of covalent bonds in polymers with full and repeatable macroscopic shape recovery. *ACS Macro Lett.* **3,** 216–219 (2014).

23. Boldyrev, V. V. Mechanochemistry and mechanical activation of solids. *Solid State Ionics* **63–65,** 537–543 (1993).

24. Braga, D. *et al.* Combining piracetam and lithium salts: ionic co-crystals and co-drugs? *Chem. Commun.* **48,** 8219 (2012).

25. Tan, D., Loots, L. & Friščić, T. Towards medicinal mechanochemistry: evolution of milling from pharmaceutical solid form screening to the synthesis of active pharmaceutical ingredients (APIs). *Chem. Commun.* **52,** 7760–7781 (2016).

26. Bruckmann, A., Krebs, A. & Bolm, C. Organocatalytic reactions: effects of ball milling, microwave and ultrasound irradiation. *Green Chem.* **10,** 1131 (2008).

27. Wu, H. & Li, Q. Application of mechanochemical synthesis of advanced materials. *J. Adv. Ceram.* **1,** 130–137 (2012).

28. Kosova, N. V., Uvarov, N. F., Devyatkina, E. T. & Avvakumov, E. G. Mechanochemical synthesis of $LiMn_2O_4$ cathode material for lithium batteries. *Solid State Ionics* **135,** 107–114 (2000).

29. Šepelák, V., Düvel, A., Wilkening, M., Becker, K.-D. & Heitjans, P. Mechanochemical reactions and syntheses of oxides. *Chem. Soc. Rev. Chem. Soc. Rev* **42,** 7507–7520 (2013).

30. James, S. L. *et al.* Mechanochemistry: opportunities for new and cleaner synthesis. *Chem. Soc. Rev.* **41,** 413–47 (2012).

31. Batzdorf, L., Fischer, F., Wilke, M., Wenzel, K.-J. & Emmerling, F. Direct in situ investigation of milling reactions using combined x-ray diffraction and Raman spectroscopy. *Angew. Chemie Int. Ed.* **54,** 1799–1802 (2015).

32. Bowmaker, G. a, Hanna, J. V, Skelton, B. W. & White, A. H. Solvent-assisted solid-state synthesis: separating the chemical from the mechanical in mechanochemical synthesis. *Chem. Commun.* **16**, 2168-2170 (2009).

33. Kwade, A. & Schwedes, J. Wet Grinding in Stirred Media Mills. *Hand. Powder Technol.* **12,** 251–382 (2007).

34. Burmeister, C. F. & Kwade, A. Process engineering with planetary ball mills. *Chem. Soc. Rev.* **42,** 7660 (2013).

35. Merupo, V.-I. *et al.* Structural and optical characterization of ball-milled copper-doped bismuth vanadium oxide ($BiVO_4$). *CrystEngComm* **17,** 3366–3375 (2015).

36. Rosenkranz, S., Breitung-Faes, S. & Kwade, A. Experimental investigations and modelling of the ball motion in planetary ball mills. *Powder Technol.* **212,** 224–

230 (2011).

37. Jiang, X., Trunov, M. A., Schoenitz, M., Dave, R. N. & Dreizin, E. L. Mechanical alloying and reactive milling in a high energy planetary mill. *J. Alloys Compd.* **478,** 246–251 (2009).

38. Matsuoka, M., Hirata, J. & Yoshizawa, S. Kinetics of solid-state polymorphic transition of glycine in mechano-chemical processing. *Chem. Eng. Res. Des.* **88,** 1169–1173 (2010).

39. Sinnott, M. D., Cleary, P. W. & Morrison, R. D. Combined DEM and SPH simulation of overflow ball mill discharge and trommel flow. *Miner. Eng.* **108,** 93–108 (2017).

40. Ward, T. S., Chen, W., Schoenitz, M., Dave, R. N. & Dreizin, E. L. A study of mechanical alloying processes using reactive milling and discrete element modeling. *Acta Mater.* **53,** 2909–2918 (2005).

41. Płóciennik, P., Guichaoua, D., Korcala, A. & Zawadzka, A. Studies of aluminium oxide thin films deposited by laser ablation technique. *Opt. Mater. (Amst).* **56,** 49–57 (2016).

42. Düvel, A. *et al.* Mechanically induced phase transformation of γ-Al_2O_3 into α-Al_2O_3. Access to structurally disordered γ-Al_2O_3 with a controllable amount of pentacoordinated al sites. *J. Phys. Chem. C* **115,** 22770–22780 (2011).

43. Kiss, S. J., Zec, S. & Boskovic, S. Transition of γ-Al_2O_3 into α-Al_2O_3 during vibro milling. *Powder Technol.* **107,** 48–53 (2000).

44. Mackenzie, K. J. D., Temuujin, J. & Okada, K. Thermal decomposition of mechanically activated gibbsite. **327,** 103–108 (1999).

45. Mackenzie, K. J. D., Temuujin, J., Smith, M. E., Angerer, P. & Kameshima, Y. Effect of mechanochemical activation on the thermal reactions of boehmite (γ-AlOOH) and g -Al 2 O 3. **359,** 87–94 (2000).

46. Kozawa, T. & Naito, M. Mechanically induced formation of metastable χ- And κ-Al_2O_3 from boehmite. *Adv. Powder Technol.* **27,** 935–939 (2016).

47. Levin, I. & Brandon, D. Metastable Alumina Polymorphs: Crystal Structures and

Transition Sequences. *J. Am. Ceram. Soc.* **81,** 1995–2012 (2005).

48. Franks, G. V. & Gan, Y. Charging behavior at the alumina-water interface and implications for ceramic processing. *J. Am. Ceram. Soc.* **90,** 3373–3388 (2007).

49. Slade, R. & M. Thompson, I. ^{27}Al nuclear magnetic resonance spectroscopy investigation of thermal transformation sequences of alumina hydrates. Part 1. - Gibbsite, γ-$Al(OH)_3$. *J. Mater. Chem.* **1**, 559-562 (1991).

50. Hiemstra, T., Yong, H. & Van Riemsdijk, W. H. Interfacial charging phenomena of aluminium (Hydr)oxides. *Langmuir* **15,** 5942–5955 (1999).

51. Leona, A. S., Secc, L., Luis, S. & Potosı, L. Fluoride adsorption onto α-Al_2O_3 and its effect on the zeta potential at the alumina – aqueous electrolyte interface. **37,** 1973–1987 (2002).

52. Kwak, J.H. *et al.* Coordinatively unsaturated Al^{3+} centers as binding sites for active catalyst phases of platinum on γ-Al_2O_3. *Science* **325,** 1670-1673 (2009).

53. Wang, Y., Shih, K. & Jiang, X. Phase transformation during the sintering of γ-alumina and the simulated Ni-laden waste sludge. *Ceram. Int.* **38,** 1879–1886 (2012).

54. Dambournet, D., Demourgues, A., Martineau, C., Durand, E., Majimel, J., Legein, C., Buzaré, J. Y., Fayon, F., Vimont, A., Leclerc, H. *et al*. Microwave synthesis of an aluminium fluoride hydrate with cationic vacancies: structure, thermal stability, and acidic properties. *Chem. Mater.* **20**, 7095−7106 (2008).

55. Pecharromán, C., Sobrados, I., Iglesias, J. E., González-Carreño, T. & Sanz, J. Thermal evolution of transitional aluminas followed by NMR and IR spectroscopies. *J. Phys. Chem. B* **103,** 6160–6170 (1999).

56. Eskandari, A., Aminzare, M., Razavi Hesabi, Z., Aboutalebi, S. H. & Sadrnezhaad, S. K. Effect of high energy ball milling on compressibility and sintering behavior of alumina nanoparticles. *Ceram. Int.* **38,** 2627–2632 (2012).

57. Singh, B. P., Menchavez, R., Takai, C., Fuji, M. & Takahashi, M. Stability of dispersions of colloidal alumina particles in aqueous suspensions. *J. Colloid Interface Sci.* **291,** 181–6 (2005).

58. Moreno, R. Colloidal processing of ceramics and composites. *Adv. Appl. Ceram.* **111,** 246–253 (2012).

59. Mikolajczyk, A. *et al.* Zeta Potential for metal oxide nanoparticles: a predictive model developed by a nano-quantitative structure–property relationship approach. *Chem. Mater.* **27,** 2400–2407 (2015).

60. Patterson, A. L. The Scherrer formula for X-ray particle size determination. *Phys. Rev.* **56,** 978–982 (1939).

61. Skibsted, J., Henderson, E. & Jakobsen, H. J. Characterization of Calcium Aluminate Phases in Cements by ^{27}Al MAS NMR Spectroscopy. *Inorg. Chem.* **32,** 1013–1027 (1993).

62. Massiot, D. *et al.* Modelling one- and two-dimensional solid-state NMR spectra. *Magn. Reson. Chem.* **40,** 70–76 (2002).

63. Ahrem, L. *et al.* Direct observation of coordinatively unsaturated sites on the surface of a fluoride-doped alumina catalyst. *J. Phys. Chem. C* **121,** 12206-12213 (2017).

64. König, R., Scholz, G., Bertram, R. & Kemnitz, E. Crystalline aluminium hydroxy fluorides—Suitable reference compounds for ^{19}F chemical shift trend analysis of related amorphous solids. *J. Fluor. Chem.* **129,** 598–606 (2008).

65. König, R. *et al.* Spectroscopic characterization of crystalline AlF_3 phases. *J. Fluor. Chem.* **131,** 91–97 (2010).

66. Isobe, T., Watanabe, T., d'Espinose de la Caillerie, J. B., Legrand, a P. & Massiot, D. Solid-state ^{1}H and ^{27}Al NMR studies of amorphous aluminium hydroxides. *J. Colloid Interface Sci.* **261,** 320–4 (2003).

67. Stosiek, C., Scholz, G., Eltanany, G., Bertram, R. & Kemnitz, E. Novel synthesis and thermal behavior of aluminium hydroxy fluorides $AlF_x(OH)_{3-x}$ *Chem. Mat.* **20**, 5687–5697 (2008).

68. Leofanti, G., Padovan, M., Tozzola, G. & Venturelli, B. Surface area and pore texture of catalysts. *Catal. Today* **41,** 207–219 (1998).

69. Greenwood, R. Review of the measurement of zeta potentials in concentrated

aqueous suspensions using electroacoustics. *Adv. Colloid Interface Sci.* **106,** 55–81 (2003).

70. Negoi, A. *et al.* Bifunctional nanoscopic catalysts for the one-pot synthesis of (±)-menthol from citral. *Top. Catal.* **55,** 680–687 (2012).

71. Agirrezabal-Telleria, I., Hemmann, F., Jäger, C., Arias, P. L. & Kemnitz, E. Functionalized partially hydroxylated MgF_2 as catalysts for the dehydration of d-xylose to furfural. *J. Catal.* **305,** 81–91 (2013).

72. Agirrezabal-Telleria, I., Guo, Y., Hemmann, F., Arias, P. L. & Kemnitz, E. Dehydration of xylose and glucose to furan derivatives using bifunctional partially hydroxylated MgF_2 catalysts and N_2-stripping. *Catal. Sci. Technol.* **4,** 1357–1368 (2014).

73. Hemmann, F., Jaeger, C. & Kemnitz, E. Comparison of acidic site quantification methods for a series of nanoscopic aluminium hydroxide fluorides. *RSC Adv.* **4,** 56900–56909 (2014).

74. Scalise, V., Scholz, G. & Kemnitz, E. Mechanochemical synthesis of low-fluorine doped aluminium hydroxide fluorides. *J. Solid State Chem.* **243,** 154–161 (2016).

75. Scholz, G., Pawlik, A., Ja, C., Rossum, B. Van & Kemnitz, E. Identification of $AlF_x(OR)_y$ species in strongly disordered aluminium isopropoxide fluoride solids : a field-dependent mas nmr study *J. Phys. Chem. C* **113**, 15576–15585 (2009).

76. Scholz, G., Feist, M. & Kemnitz, E. On the influence of humidity on the mechanochemical reaction between NaF and AlF_3. *Solid State Sci.* **10,** 1640–1650 (2008).

77. Budau, J. H., Paulus, B. & Steenbergen, K. G. Theoretical investigation of the crystal structure of AlOF. *Chem. Phys.* **491,** 112–117 (2017).

78. Kitamura, M. & Senna, M. Effects of preheating on mechanochemical amorphisation and enhanced reactivity of aluminium hydroxide. *Adv. Powder Technol.* **12,** 215–226 (2001).

79. Baranyai, Z. V., Kristály, F. & Szűcs, I. Influence of the short time grinding on the thermal decomposition processes of gibbsite produced by the bayer process. *Mater. Sci. Eng.* **38,** 15–27 (2013).

80. Li, J., Wu, Y., Pan, Y., Liu, W. & Guo, J. Influence of fluorides on phase transition of α-Al_2O_3 formation. *Ceram. Int.* **33,** 919–923 (2007).

81. Wenshan Bünger., V. Mechanochemische synthese von fluor-dotiertem γ-aluminiumoxid (2015).

82. Peckham, S. & Awofeso, N. Water fluoridation: A critical review of the physiological effects of ingested fluoride as a public health intervention. *Sci. World J.* (2014).

83. Fawell, J., Bailey, K., Chilton, J. World Health Organization. Fluoride in drinking-water. (2006).

84. Mohapatra, M., Anand, S., Mishra, B. K., Giles, D. E. & Singh, P. Review of fluoride removal from drinking water. *J. Environ. Manage.* **91,** 67–77 (2009).

85. Jiang, K., Zhou, K., Yang, Y. & Du, H. A pilot-scale study of cryolite precipitation from high fluoride-containing wastewater in a reaction-separation integrated reactor. *J. Environ. Sci. (China)* **25,** 1331–1337 (2013).

86. Emamjomeh, M. M. & Sivakumar, M. Fluoride removal by a continuous flow electrocoagulation reactor. *J. Environ. Manage.* **90,** 1204–1212 (2009).

87. Adak, M. K., Chakraborty, S., Sen, S. & Dhak, D. Synthesis and optimization of low-cost and high efficient zirconium-aluminium modified iron oxide nano adsorbent for fluoride removal from drinking water *Advanc. Mater. Proc*. **2**, 716-724 (2017).

88. Sailaja, K. *et al*. J. Removal of fluoride from drinking water by adsorption onto activated alumina and activated carbon. *Int. J. Eng. Res. Appl.* **5,** 19–24 (2015).

89. Amor, Z. *et al.* Fluoride removal from brackish water by electrodialysis. *Desalination* **133,** 215–223 (2001).

90. Bhatnagar, A., Kumar, E. & Sillanpää, M. Fluoride removal from water by adsorption-A review. *Chem. Eng. J.* **171,** 811–840 (2011).

91. Chauhan, V. S., Dwivedi, P. K. & Iyengar, L. Investigations on activated alumina based domestic defluoridation units. *J. Hazard. Mater.* **139,** 103–107 (2007).

92. Wirth, J., Schacht, J., Saalfrank, P. & Paulus, B. Fluorination of the hydroxylated α-Al_2O_3(0001) and Its Implications for water adsorption: a theoretical study. *J. Phys. Chem. C* **120**, 9713-9718 (2016).

93. Farrah, H., Pickering, W. Fluoride interactions with hydrous aluminum oxides and alumina *Austr. J. Soil. Res.* **24,** 55-69 (1999).

94. Tomar, V. & Kumar, D. A critical study on efficiency of different materials for fluoride removal from aqueous media. *Chem. Cent. J.* **7,** 51 (2013).

95. Chunduri, L. A. *et al.* Single step preparation of nano size gamma alumina exhibiting enhanced fluoride adsorption. *Mater. Express* **4,** 235–241 (2014).

96. Chauruka, S. R. *et al.* Effect of mill type on the size reduction and phase transformation of gamma alumina. *Chem. Eng. Sci.* **134,** 774–783 (2015).

97. Fan, X., Parker, D. J. & Smith, M. D. Adsorption kinetics of fluoride on low cost materials. *Water Res.* **37,** 4929–4937 (2003).

98. Shimizu, K. *et al.* Bifluoride ($[HF_2]^-$) formation at the fluoridated aluminium hydroxide/water interface. *Dalt. Trans.* **45,** 9045–9050 (2016).

99. Zielinski, P .A. *et al.* Structural transformation of alumina by high-energy ball milling. *Mater. Res.* **8,** 2985–2992 (1993).

100. JCPDS-ICDD, International Center for Diffraction Data: PDF-2 Database (sets 1-51 plus 70-89), PA 19073-3272 U.S.A., Release 2001- PCPDFWIN Version 2.2.

101. Cory, D. G. & Ritchey, W. M. Suppression of signals from the probe in bloch decay spectra. *J. Magn. Reson.* **80,** 128–132 (1988).

102. Dollimore, D. Thermal Analysis. *Anal. Chem.* **62,** 394–402 (1990).

103. Sing, K. S. & Williams, R. T. Physisorption Hysteresis Loops and the Characterization of Nanoporous Materials. *Adsorpt. Sci. Technol.* **22,** 773–782 (2004).

Appendix

A1. List of abbreviations

Techniques

BET	Brunauer- Emmett- Teller
CP	Cross Polarization
DFT	Density Functional Theory
FT-IR	Fourier Transform- Infra Red
ICP- OES	Inductively Coupled Plasma- Optical Emission Spectroscopy
MAS	Magic Angle Spinning
NMR	Nuclear Magnetic Resonance
TG-DTA	ThermoGravimetric- Differential Thermal Analisys
TPD	Temperature Programmed Desorption
XRD	X-Ray Diffraction
ZP	Zeta Potential

Formula

$Al(OH)_3$	Aluminium trihydroxide
Al_2O_3	Aluminium oxide
AlF_3	Aluminium fluoride
$AlF_3 \cdot 3H_2O$	Aluminium fluoride trihydrate
$CFCl_3$	Trichlorofluoromethane
D_2O	Deuterium oxide
HCl	HydroChloric acid
NaF	Sodium fluoride
NaOH	Sodium hydroxide
NH_4F	Ammonium fluoride

Symbols

°C	Degrees Centigrade
cm	Centimeters
DMFIT	Software for simulation solid state NMR spectra developed by Dominique Massiot
Exo	Exothermal reaction
h	Hours
Hz	Hertz
I	Nuclear spin
IEP	Isoelectric Point
M	Molar
min	Minutes
mV	milliVolt
Na	number of accumulations
PDF	Standard X-ray Diffraction Powder Patterns
ppm	parts per million
r. t.	room temperature
rpm	rounds per minute
T	Tesla
δ	Chemical Shift (ppm)
θ	Scattering Angle
μs	Microseconds
ν	Frequency

A2. Declaration

Selbstständigkeiterklärung

Hiermit versichere ich, Valentina Scalise, dass ich die vorliegende Arbeit selbstständig und nur unter Einsatz der angegeben Hilfsmittel und Quellen am Institut für Chemie der Humboldt-Universität zu Berlin angefertigt habe.

Valentina Scalise Berlin, den